ABSTRACT

Title of dissertation: FEEDBACK EXPERIMENTS
USING ENTANGLED PHOTONS
FOR POLARIZATION CONTROL
IN FUTURE QUANTUM NETWORKS
Evan Dowling, Doctor of Philosophy, 2023

Dissertation directed by: Professor Thomas E. Murphy
Department of Physics

Control of the measurement frames that project on polarization entangled photons is an important experimental task for near term fiber-based quantum networks. Because of the changing birefringence in optical fiber arising from temperature fluctuations or external vibrations, the polarization projection direction at the end of a fiber channel is unpredictable and varies with time. This polarization drift can cause errors in quantum information protocols, like quantum key distribution, that rely on the alignment of measurement bases between users sharing a quantum state. Polarization control within fiber is typically accomplished using feedback measurements from classical power alignment signals, multiplexed in time or wavelength with the quantum signal that coexist in the same fiber. This thesis explores ways to use only measurements on the entangled photons for polarization control and perform entanglement measures without multiplexing alignment signals. This approach is experimentally less complex and can reduce the noise within the quantum channel arising from the alignment signals. In the first part of this dissertation, we study how to use distributed measurements on polarization entangled photons for polarization drift correction in a 7.1 km deployed fiber between the University of Maryland and the Laboratory of Telecommunication Sciences for two individuals sharing a near maximally entangled Bell state, $\hat{\rho}=|\Psi^-\rangle\langle\Psi^-|$. In the second part of the dissertation, we examine how to use feedback measurements to maximize the

violation of a Bell's inequality used as an entanglement measure. Both polarization drift correction and the maximization of a Bell's inequality violation use iterative optimization algorithms to actuate upstream polarization controllers. In the Bell's inequality investigation, three numerical methods: Bayesian optimization, Nelder-Mead simplex optimization, and stochastic gradient descent are implemented and compared against each other. For complete polarization control and Bell's inequality violation experiments, we developed a polarization and time multiplexed detection system that reduced the number of photon detectors needed and mitigated the demand on the coincidence counting electronics for real-time feedback and control.

Feedback Experiments using Polarization Entangled Photons for Polarization Control on Future Quantum Networks

by

Evan Dowling

Dissertation submitted to the Faculty of the Graduate School of the
University of Maryland, College Park in partial fulfillment
of the requirements for the degree of
Doctor of Philosophy
2024

Advisory Committee:
Professor Thomas E. Murphy, Chair/Advisor
Professor Rajarshi Roy, Co-Advisor
Professor Julius Goldhar
Professor Yanne Chembo
Professor Wendell T. Hill

Acknowledgements

Graduating with a PhD from the University of Maryland after coming out of high school in rural Wisconsin and without a particular direction in life, would have never been possible without many things going right in my life. To begin to thank all the people involved would be a chapter in itself, but let me try.

To start with, I want to thank my family and friends back home. To my parents, brothers, and extended family members whose endless support, love, encouragement, and unwavering belief in my abilities were a constant source of strength throughout my graduate school journey, this accomplishment would not have been possible without you.

I am thankful for my undergraduate university, the University of Wisconsin-La Crosse, that fostered a growing interest in physics and punched way above its weight in its educational quality. I want to give a special shout out to my undergraduate research advisor, Professor Eric Barnes, who first believed in my abilities to conduct research and guide in the transition to graduate school.

I am indebted to my University of Maryland advisors, Professors Thomas Murphy and Rajarshi Roy, for their kindness, invaluable guidance, and expertise. I have often been told that it is not what you work on, but who you work with that matters most, and I could not have asked for better advisors. Their mentorship has been instrumental in shaping my research and academic pursuits, but the way they foster a positive and supportive environment to work in has been nothing short of inspirational.

I am grateful to the members of my dissertation committee for their impact not just on this dissertation, but on my general education in physics and quantum optics. Their expertise throughout my entire graduate school experience has significantly enriched the quality of this work.

A special thanks is needed to the team at the Laboratory for Telecommunication Sciences (LTS), where most of this research took place. Their funding and access to equipment has enabled me to pursue interesting academic questions and make small contributions to the body of physics. Mark Morris, your expertise in the lab never ceases to amaze me and your ability to drop everything to help a novice experimentalist manage an experiment on his own is the reason why my confidence in the lab grew. Gerry Baumgartner, your guidance over my research direction and persistent nudging to graduate is half the reason this dissertation came together. To all my other LTS friends, our talks about physics and life outside physics have made my time at LTS all the more valuable.

Any marathon-like endeavor is bound to have difficult moments, but being able to turn to my friends within my physics cohort and the cohort below me (who adopted me as their own) for support, distraction, and guidance has been crucial. Outside of hanging out, our disc golf outings, friends-givings, climbing, pick-up basketball games, triathlon races, and back-to-back intramural flag football championships are some of the highlights of my graduate school experience and I am happy to have shared them with you all.

To Josiland Chambers and the staff in the Institute for Research in Electronics and Applied Physics (IREAP), your support and ability to work last minute after I missed an important deadline or submission have saved me more times than I would like to admit.

Lastly, this dissertation would not have been possible without the love, understanding, and support of my better half, Lindsay Smith. No one knows the hills and valleys of graduate school better than a graduate student, and to undertake the final part of our graduate school adventure together is something I will always treasure. Out of everything that I have done with my time at Maryland, finding you is my greatest achievement.

This dissertation is the culmination of the collective efforts of many individuals, and I am profoundly grateful for each and every contribution that has helped me reach this milestone.

Thank you.

Table of Contents

List of Tables

List of Figures

Contributed Works and Dissertation Outline

The motivation of this dissertation was to find a solution for polarization drift and polarization control of quantum signals being sent through a quantum network using only the quantum signals. When a photon's or entangled photons' information is encoded in polarization, the polarization state may change due to the birefringence of the single-mode fiber they travel through. This change in the quantum state can affect downstream measurements on the photons, leading to errors in quantum information protocols that use them. We wanted to investigate if measurements on entangled photons could be enough to correct the relative polarization drift between two users sharing an entangled state in deployed fiber. The scope of this work was to investigate methods that could be applied to the developing quantum network in the Washington DC metro area, DC-Qnet, which is discussed more in section 1.7. The work leading up to this dissertation has been published in articles:

- Non-local polarization alignment and control in fiber using feedback from correlated measurements of entangled photons [1]
- Automated Bell Inequality Violation Searches for Estimating Entanglement Quality in Future Quantum Networks (in prepublication)

and presented at conferences:

- CLEO 2023: Automated Bell Inequality Violation using Uncalibrated Fiber Squeezing Polarization Controllers[2]
- APS March Meeting 2022: Polarization Drift Compensation in Fiber using Feedback from Correlated Measurements of Entangled Photons [3]
- APS March Meeting 2021: Self-guided method to search for EPR state correlations using uncalibrated polarization controllers in a plug-and-play optical system.[4]

The outline of this dissertation is as follows. In chapter 1, the basic physics concepts are introduced. In chapter 2, the experimental details for the creation, manipulation, and detection of polarization entangled light is discussed. In chapters 3 and 4, the results from the papers mentioned above, where polarization drift is corrected and entanglement measures are attained from automated algorithms using feedback from measurements on entangled particles. Lastly, in chapter 5, the main findings of this dissertation are summarized and future work is presented.

Chapter 1

Introduction, Motivation, and Essential Physics

> We are currently in the midst of a second quantum revolution. The first quantum revolution gave us the rules that govern physical reality. The second will take these rules and use them to develop new technologies.
>
> Jonathan P. Dowling

To understand the contributions of this dissertation one must know what polarization and quantum entanglement are. Within this introduction, I will attempt to explain polarization and quantum entanglement in a brief but hopefully complete way. While doing so I will motivate the interesting problem of controlling for polarization drift in fiber networks. I will discuss the pros and cons of existing polarization control techniques and how our method of using feedback from measurements on entangled photons attempts to address some of those problems for quantum networks. I will then briefly examine how this fits into the infrastructure of future quantum networks.

1.1 Polarization and Polarization Control - Classical Electrodynamics

Quantum mechanics as we will soon see, often forces us to accept that the world works in nonintuitive ways. Instead of beginning there, let us start with something more tangible: real and imaginary, three-dimensional waves oscillating trillions of times a second in time and space.

In first-year physics courses, one learns that the propagation equations of electric and magnetic fields determined by Maxwell equations within empty space are plane waves

$$\begin{aligned} \boldsymbol{E}(\boldsymbol{r},t) &= \Re(\boldsymbol{E}_0 e^{-i(\omega t - \boldsymbol{k}\cdot\boldsymbol{r})}) \\ \boldsymbol{H}(\boldsymbol{r},t) &= \sqrt{\frac{\varepsilon_0}{\mu_0}} \frac{\boldsymbol{k}}{|\boldsymbol{k}|} \times \boldsymbol{E}(\boldsymbol{r},t) \end{aligned} \tag{1.1}$$

where ω is the frequency, $\boldsymbol{k}$ is the wave vector, $\Re$ is the real part, and ε_0 and μ_0 are the permittivity and permeability of empty space [5, 6]. Each solution has a specific phase velocity and wavelength. These transverse waves oscillate in the direction perpendicular to the direction of propagation specified by wave vector $\boldsymbol{k}=2\pi/\lambda\hat{k}$. Polarization is historically defined as the direction of the electric field. As equation (1.1) shows, $\boldsymbol{E}(\boldsymbol{r},t)$ gives the full description of both the electric and magnetic fields.

For nearly all wavelengths of light, the electric field oscillates too rapidly to determine its orientation, or its potentially time-dependent orientation, for experimentalists to measure. As an example, the slowest oscillating light in the visible spectrum (red light at 750nm), still oscillates 400 trillion (4×10^{14}) times each second. Instead of directly measuring the orientation of the electric field, the polarization is mapped to intensity measures along specific electric field projection directions. For electric fields of constant polarization orientations, the intensity measures are time-independent and can be easily measured experimentally. This mapping is summarized in the equivalent descriptions of polarization: Jones vectors (electric field) and Stokes vectors (intensity measures).

1.1.1 Polarization Ellipse and Two Equivalent Polarization Formalisms

To study the polarization of light, let us first make our expression of $\boldsymbol{E}$ simpler by choosing $\boldsymbol{r}=0$. We set the direction of propagation to equal $\hat{\boldsymbol{z}}$ so that $\boldsymbol{k}=\frac{2\pi}{\lambda}\hat{\boldsymbol{z}}$. Breaking the complex $\boldsymbol{E}(\boldsymbol{0},t)$

into two orthogonal components $\hat{x}$,$\hat{y}$ we see

$$\boldsymbol{E}(\mathbf{0},t)=\boldsymbol{E}_0 e^{-i\omega t}=\begin{pmatrix} E_{0x}e^{i\phi_x} \\ E_{0y}e^{i\phi_y} \end{pmatrix} e^{-i\omega t} \tag{1.2}$$

where E_{0x}, E_{0y}, ϕ_x, and ϕ_y are real numbers. The real-valued counterpart can be written as

$$\boldsymbol{E}(\mathbf{0},t)=E_{0x}\cos(\omega t+\phi_x)\hat{x}+E_{0y}\cos(\omega t+\phi_y)\hat{y} \quad . \tag{1.3}$$

Defining the time-dependent amplitudes as

$$X(t)=E_{0x}\cos(\omega t+\phi_x)$$

$$Y(t)=E_{0y}\cos(\omega t+\phi_y)$$

one can observe that $X(t)$ and $Y(t)$ trace out an ellipse with respect to time. The derivation is shown in the appendix A.1. The polarization ellipse can be written as

$$\frac{X^2}{E_{0x}^2}+\frac{Y^2}{E_{0y}^2}-2\frac{XY}{E_{0x}E_{0y}}\cos(\phi_y-\phi_x)=\sin^2(\phi_y-\phi_x) \quad . \tag{1.4}$$

This equation shows that at any instant of time, the locus of points described by the trajectory of $X(t)$ and $Y(t)$ will trace out an elliptical curve.

For $\phi=\phi_y-\phi_x=0$ we get linear polarization states where the orientation is determined by the angle χ where $\tan\chi=E_{0y}/E_{0x}$. For $\phi=\pm\pi/2$ and $\chi=\pi/4$ we get the right and left circular polarization states for plus and minus $\pi/4$ respectively. For all other states of ϕ and χ the polarization can be described as elliptical. The electric field vector can be rewritten in terms

of these ellipse parameters

$$\boldsymbol{E}=E_0\begin{pmatrix}\cos\chi\\ \sin\chi e^{i\phi}\end{pmatrix} \quad . \tag{1.5}$$

where $E_0=\sqrt{E_{0x}^2+E_{0y}^2}$. When normalized to unity this complex 2-row column vector is called the Jones polarization vector [7–9]

$$|j\rangle=\boldsymbol{E}/E_0=\begin{pmatrix}\cos\chi\\ \sin\chi e^{i\phi}\end{pmatrix} \quad . \tag{1.6}$$

The state of polarization is completely described by the quantities χ, and ϕ. If you were looking towards a propagating wave ($-z$ direction) an example of the polarization ellipse is seen in figure 1.

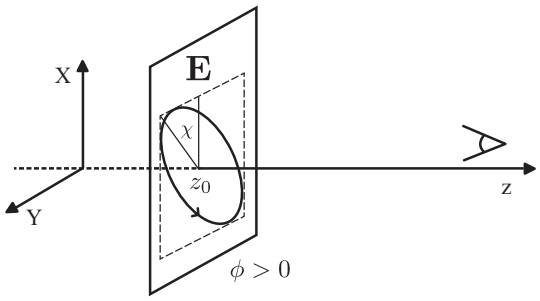

Figure 1: Polarization ellipse for an electromagnetic wave, $\boldsymbol{E}$, traveling in the positive z direction with ellipse parameters χ and ϕ. At the screen's location z_0, $\boldsymbol{E}$ will rotate in time at frequency ω around the ellipse in the counterclockwise direction for positive, nonzero ϕ.

Since the electric field oscillates with angular frequency ω, any measurement of the electric field must have a time resolution better than $1/\omega$. For all optical waves, this is impossible. Instead, the polarization quantities (χ and ϕ) can be estimated through a series of 6 intensity measurements (I_H,I_V,I_D,I_A,I_R,I_L) in different measurement bases. Rotating the measurement basis from horizontal $\hat{x}$ and vertical $\hat{y}$ can be described as a unitary transform, where $\hat{\boldsymbol{U}}\hat{\boldsymbol{U}}^\dagger=1$. In

general, this description can be written in Cayley-Klein form using complex entries a and b

$$\hat{\boldsymbol{U}}(a,b)=\begin{pmatrix} a & b \\ -b^* & a^* \end{pmatrix} \tag{1.7}$$

where the Hermitian conjugate $\boldsymbol{U}^\dagger(a,b)=\boldsymbol{U}(a^*,-b)$ and $|a|^2+|b|^2=1$. Polarization transformations will be described more in the following section. Measurements themselves can be described by a projection matrix. A projection direction along a specific linear polarization direction where θ describes the rotation from horizontal is

$$\hat{\boldsymbol{M}}(\theta)=\begin{pmatrix} \cos^2\theta & \sin\theta\cos\theta \\ \sin\theta\cos\theta & \sin^2\theta \end{pmatrix} \quad . \tag{1.8}$$

Intensity measurements (I_H,I_V,I_D,I_A,I_R,I_L) are then described by

$$\begin{aligned} I_k&=\left\langle \hat{\boldsymbol{M}}(\boldsymbol{\theta}) \right\rangle=\boldsymbol{E}_{rot}^\dagger \hat{\boldsymbol{M}}(\boldsymbol{\theta})\boldsymbol{E}_{rot} \\ &=\boldsymbol{E}^\dagger \hat{\boldsymbol{U}}^\dagger \hat{\boldsymbol{M}}(\boldsymbol{\theta})\boldsymbol{E} \quad . \end{aligned} \tag{1.9}$$

For horizontal, vertical, diagonal, and anti-diagonal intensities, the unitary transform before the measurement is the identity matrix, and the measurement angles are θ=0,$\pi/2$,$\pi/4$,$-\pi/4$ respectively. For right and left circular intensities, the unitary transform is done by a $\pi/4$ rotated quarter-waveplate to convert R and L circular polarized light into linear horizontal and vertical light, respectively (θ=0,$\pi/2$).

$$\hat{\boldsymbol{U}}_{\text{QWP}}\left(\frac{\pi}{4}\right)=\frac{1}{\sqrt{2}}\begin{pmatrix} 1 & i \\ -i & 1 \end{pmatrix}$$

The intensities can be written for the electric field (1.5) by using the appropriate unitary and

projection matrices in (1.9)

$$
\begin{aligned}
I_H &= E_0^2 \cos^2\chi/2 \\
I_V &= E_0^2 \sin^2\chi/2 \\
I_D &= \left(E_0^2\cos^2\chi + E_0^2\sin^2\chi\right)/4 + \left(E_0^2\cos\chi\sin\chi/2\right)\cos\phi \\
I_A &= \left(E_0^2\cos^2\chi + E_0^2\sin^2\chi\right)/4 - \left(E_0^2\cos\chi\sin\chi/2\right)\cos\phi \\
I_R &= \left(E_0^2\cos^2\chi + E_0^2\sin^2\chi\right)/4 + \left(E_0^2\cos\chi\sin\chi/2\right)\sin\phi \\
I_L &= \left(E_0^2\cos^2\chi + E_0^2\sin^2\chi\right)/4 - \left(E_0^2\cos\chi\sin\chi/2\right)\sin\phi \quad .
\end{aligned}
\tag{1.10}
$$

Combinations of these intensities can be combined into four terms called the Stokes parameters, which are defined by the equations

$$
\begin{aligned}
S_0 &= I_H + I_V = \frac{1}{2}E_0^2 \\
S_1 &= I_H - I_V = \frac{1}{2}E_0^2\cos 2\chi \\
S_2 &= I_D - I_A = \frac{1}{2}E_0^2\sin 2\chi\cos\phi \\
S_3 &= I_R - I_L = \frac{1}{2}E_0^2\sin 2\chi\sin\phi \quad .
\end{aligned}
\tag{1.11}
$$

For pure polarized light and normalizing the electric field magnitude to unity, $S_0=1$, the real-valued Stokes vector $\boldsymbol{S}=(S_1,S_2,S_3)$ uniquely describes the polarization just like the Jones vector (1.5). One can think about the quantity S_1 as the amount of polarization in the horizontal versus vertical direction. Similar arguments can be made for S_2 and S_3 with diagonal/anti-diagonal and right/left circular directions. When looking at the equations (1.11) one notices the parameters S_1,S_2,S_3 look like the equations for a point on the surface of the sphere with radius $\frac{1}{2}E_0^2$ and with angles 2χ being the angle from the positive S_1 axis and ϕ being the angle from the

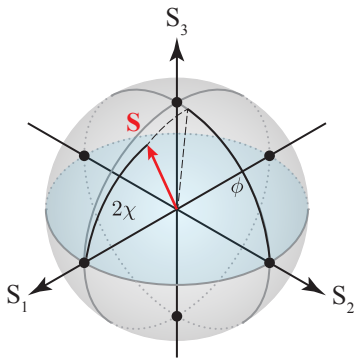

Figure 2: Poincaré sphere representation of the state of polarization for Stokes polarization vector $\boldsymbol{S}$. $\pm S_1$ represents horizontal/vertical polarization, $\pm S_2$ represents diagonal/anti-diagonal polarization, and $\pm S_3$ represents left/right circular polarization.

positive S_2 direction in the S_2/S_3 plane projection. This sphere is dubbed the Poincaré sphere and can be seen in figure 2. This transformation gives additional insights into the nature of unitary polarization transformation as the equivalent Stokes vector transformation is a three-dimensional rotation about a Stokes vector $\boldsymbol{r}$ with precession angle φ. The Jones vector can be reconstructed from the Stokes vector (up to a complex constant) as

$$\boldsymbol{E}(S_1,S_2,S_3)=\begin{pmatrix} \sqrt{\frac{1}{2}(1+S_1)} \\ \sqrt{\frac{1}{2}(1-S_1)}e^{i\arctan_2(S_3,S_2)} \end{pmatrix} \tag{1.12}$$

where $\arctan_2$ is the two-argument arctangent valid for a positive and negative S_2. The Stokes vector can be reconstructed from the Jones vector as

$$\boldsymbol{S}(\chi,\phi)=\begin{pmatrix} S_1 \\ S_2 \\ S_3 \end{pmatrix}=\begin{pmatrix} \cos 2\chi \\ \sin 2\chi\cos\phi \\ \sin 2\chi\sin\phi \end{pmatrix} \quad . \tag{1.13}$$

The Jones vector for the 6 nodes of the Poincaré sphere can be written in terms of the horizontal,

$\hat{x}$, and vertical, $\hat{y}$, measurement bases

$$\boldsymbol{E}_{S_1}=\boldsymbol{E}(1,0,0)=\begin{pmatrix}1\\0\end{pmatrix}=\hat{x} \qquad \boldsymbol{E}_{-S_1}=\boldsymbol{E}(-1,0,0)=\begin{pmatrix}0\\1\end{pmatrix}=\hat{y}$$

$$\boldsymbol{E}_{S_2}=\boldsymbol{E}(0,1,0)=\frac{1}{\sqrt{2}}\begin{pmatrix}1\\1\end{pmatrix}=\frac{1}{\sqrt{2}}(\hat{x}+\hat{y}) \qquad \boldsymbol{E}_{-S_2}=\boldsymbol{E}(0,-1,0)=\frac{1}{\sqrt{2}}\begin{pmatrix}1\\-1\end{pmatrix}=\frac{1}{\sqrt{2}}(\hat{x}-\hat{y})$$

$$\boldsymbol{E}_{S_3}=\boldsymbol{E}(0,0,1)=\frac{1}{\sqrt{2}}\begin{pmatrix}1\\i\end{pmatrix}=\frac{1}{\sqrt{2}}(\hat{x}+i\hat{y}) \qquad \boldsymbol{E}_{-S_3}=\boldsymbol{E}(0,0,-1)=\frac{1}{\sqrt{2}}\begin{pmatrix}1\\-i\end{pmatrix}=\frac{1}{\sqrt{2}}(\hat{x}-i\hat{y}) \tag{1.14}$$

The normalized Stokes vector, $|\boldsymbol{S}|=1$, can be written in a nice compact form using the normalized Jones vector $|j\rangle=\boldsymbol{E}/|\boldsymbol{E}|$

$$\boldsymbol{S}=\begin{pmatrix}S_1\\S_2\\S_3\end{pmatrix}=\begin{pmatrix}\langle j|\hat{\sigma}_1|j\rangle\\\langle j|\hat{\sigma}_2|j\rangle\\\langle j|\hat{\sigma}_3|j\rangle\end{pmatrix}=\langle j|\hat{\boldsymbol{\sigma}}|j\rangle \tag{1.15}$$

where the Pauli matrices and Pauli matrix vector are defined as

$$\hat{\boldsymbol{\sigma}}=\hat{\sigma}_1\hat{\boldsymbol{s}}_1+\hat{\sigma}_2\hat{\boldsymbol{s}}_2+\hat{\sigma}_3\hat{\boldsymbol{s}}_3 \tag{1.16}$$

$$\sigma_1=\begin{pmatrix}1&0\\0&-1\end{pmatrix} \qquad \sigma_2=\begin{pmatrix}0&1\\1&0\end{pmatrix} \qquad \sigma_3=\begin{pmatrix}0&-i\\i&0\end{pmatrix} \tag{1.17}$$

and $\hat{\boldsymbol{s}}_i$ are unit vectors on the Poincaré sphere (Stokes space) in the i^{th} direction. For normalized vectors, $\langle j|j\rangle=1$, we can construct the projector in terms of the Stokes vector

$$|j\rangle\langle j|=\frac{1}{2}\Big(I+\boldsymbol{S}\cdot\hat{\boldsymbol{\sigma}}\Big) \quad . \tag{1.18}$$

By multiplying equation (1.18) on the right by $|j\rangle$ we can see the compact way to map Stokes vectors to Jones vectors. One needs to calculate the eigenvector associated with the $+1$ eigenvalue of matrix $\boldsymbol{S}\cdot\hat{\boldsymbol{\sigma}}$:

$$\boldsymbol{S}\cdot\hat{\boldsymbol{\sigma}}|j\rangle=|j\rangle \quad . \tag{1.19}$$

1.1.2 Polarization Transformation and Control

Polarization transformation is the act of changing the polarization from one state to another. Specifically, each transformation is a unitary transformation on the polarization Jones vector or, equivalently, a rotation operation on the polarization Stokes vector. Any two-level unitary transform can be decomposed into the form

$$\hat{\boldsymbol{U}}(\boldsymbol{r},\delta)=\cos(\delta/2)\hat{\boldsymbol{I}}_2-i\,\sin(\delta/2)\boldsymbol{r}\cdot\hat{\boldsymbol{\sigma}} \tag{1.20}$$

where $\boldsymbol{r}$ is the Stokes eigenvector of $\hat{\boldsymbol{U}}$ and δ is the rotation angle about the eigenvector on the Poincaré sphere. From the arbitrary Cayley-Klein form of equation (1.7), $a=\cos(\delta/2)-ir_1\sin(\delta/2)$ and $b=-i(r_2-ir_3)\sin(\delta/2)$ with $\boldsymbol{r}=(r_1,r_2,r_3)$ and $||\boldsymbol{r}||=1$.

A given polarization Jones vector, $|j_0\rangle$, is transformed into a new Jones vector by matrix multiplication

$$|j_f\rangle=\hat{\boldsymbol{U}}|j_0\rangle \quad . \tag{1.21}$$

Each unitary has an eigenvector and eigenvalue

$$\hat{\boldsymbol{U}}|j_\pm\rangle=e^{\pm i\varphi}|j_\pm\rangle \tag{1.22}$$

where φ is some phase and the eigenvector $|j_\pm\rangle$ is the determined through the Stokes vector $\boldsymbol{r}$ and

equation (1.12).

This transform is equally described by the polarization Stokes vector $\boldsymbol{S}_0$ and 3x3 real entry rotation matrix $\boldsymbol{R}$ and the matrix multiplication

$$\boldsymbol{S}_f = \boldsymbol{R}\boldsymbol{S}_0 \tag{1.23}$$

where in vector form

$$\boldsymbol{R}(\boldsymbol{r},\delta) = (\boldsymbol{r}\boldsymbol{r}\cdot) + \sin\delta(\boldsymbol{r}\times) - \cos\delta(\boldsymbol{r}\times)(\boldsymbol{r}\times) \tag{1.24}$$

and the equivalence between $\hat{\boldsymbol{U}}$ and $\boldsymbol{R}$ is given explicitly by

$$R_{j,k} = \frac{1}{2}\mathrm{Tr}\left\{\hat{\boldsymbol{U}}\sigma_k\hat{\boldsymbol{U}}^{\dagger}\sigma_j\right\} \quad . \tag{1.25}$$

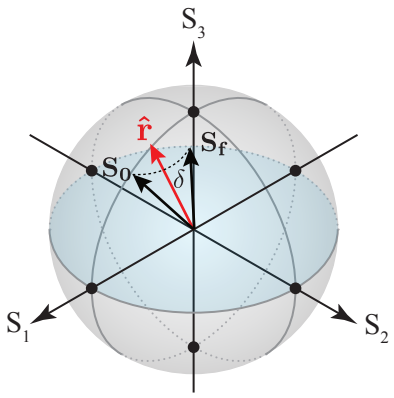

Figure 3: Rotation of polarization state $\mathbf{S_0}$ to $\mathbf{S_f}$ by rotation axis $\hat{\boldsymbol{r}}$ and rotation angle δ.

For complete polarization control from a sender of a polarization state to the receiver of that polarization state the Poincaré spheres within the sender's frame and the receiver's frame must be aligned. When this is done, any polarization state $\boldsymbol{S}$ sent from the source will be measured as $\boldsymbol{S}$ and not some other rotated state $\boldsymbol{S}'$. This can be accomplished by sending two orthogonal Stokes vectors, typically aligned in the $\hat{\boldsymbol{s}}_1$ and $\hat{\boldsymbol{s}}_2$ directions, and having the receiver rotate the polarization

states until the signal referring to $\hat{\boldsymbol{s}}_{1,2}$ points along the direction of $\hat{\boldsymbol{s}}_{1,2}$ within their measurement frame. Once this is done, the two measurement frames will be aligned and any arbitrary state $\boldsymbol{S}$ will be measured as $\boldsymbol{S}$. This can be extended to two individuals measuring a shared quantum state where one is not the sender, but both are receivers. Through joint measurements on the quantum state and feedback to upstream polarization controllers, if they can align their $\hat{\boldsymbol{s}}_{1,2}$ measurement projection directions their measurement frames will be aligned.

1.2 Polarization Drift in Fiber

In a fiber communication network, information is carried not by plane waves, but by guided optical modes down fiber. The most widely used optical fiber is single-mode fiber, which has a cylindrical core of a higher refractive index that is surrounded by a lower-index cladding layer. When the core dimension is sufficiently small, the optical fiber supports only one transverse propagating mode, hence the term ”single-mode fiber“. Because of the cylindrical symmetry of the fiber, shown in figure 40 of the appendix, there are actually two degenerate eigenmodes corresponding to the two orthogonal transverse polarization states. More details are provided in the appendix A.2. However, in the real world, fibers aren't perfectly symmetric due to manufactured defects, applied stresses, and bending from deployment. Additionally, environmental impacts such as vibrations from cars, trains, and wind, as well as temperature changes, can change the index of refraction along different polarization directions. If propagation due to the index of refraction is different along the different polarization directions the fiber is said to be birefringent. When the fiber exhibits any birefringence the polarization of light injected into a fiber can be different than the light exiting it.

To see this, let us examine a birefringent fiber of length L. Assume the index of refraction along the H direction, n_H, is greater than the index of refraction along the V direction, n_V, and

the difference of indexes can be defined as $\Delta n{=}n_H{-}n_V$. The total relative phase lag between the two perpendicular eigenmodes in the H and V direction can be expressed as:

$$\begin{aligned}\Delta\delta &= \frac{2\pi}{\lambda}\Delta nL \\ &= \frac{\omega}{c}\Delta nL\end{aligned} \tag{1.26}$$

From (1.20) and (1.24) the polarization transformation $\hat{\boldsymbol{U}}(\boldsymbol{r},\Delta\delta)$ and $\boldsymbol{R}(\boldsymbol{r},\Delta\delta)$ rotates the initial polarization state according to equations (1.21) and (1.23). Where $\boldsymbol{r}$ is the eigenvector of the fiber's unitary transform (1.21).

In general, the birefringence can be along any direction and one can define a birefringence vector in Stokes space

$$\begin{aligned}\boldsymbol{\beta} &= \frac{\Delta\delta}{l}\boldsymbol{r}_+ \\ &= \frac{\omega}{c}\Delta n\boldsymbol{r}_+\end{aligned} \tag{1.27}$$

where the magnitude $\Delta\delta/l$ represents the birefringent phase per unit length between the polarizations eigenvectors $\boldsymbol{r}_\pm$. The rate of polarization change from this birefringence while light propagates down the fiber in the z-direction is

$$\frac{\partial \boldsymbol{S}}{\partial z} = \boldsymbol{\beta}\times\boldsymbol{S} \quad . \tag{1.28}$$

The new polarization after propagating a length $z{=}L$, using equation (1.24), is just $\boldsymbol{S}_f{=}\boldsymbol{R}(\boldsymbol{r}_+,|\boldsymbol{\beta}|L)\boldsymbol{S}_0$. Equally, the rate of change of the polarization with different input frequencies through the birefringent media gives an identical differential equation

$$\frac{\partial \boldsymbol{S}}{\partial \omega} = \boldsymbol{\beta}\times\boldsymbol{S} \quad . \tag{1.29}$$

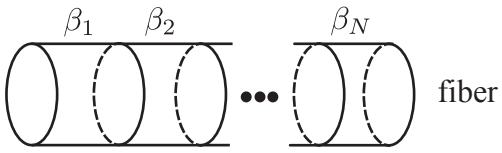

Figure 4: Schematic of long fiber with N birefringent elements with birefringence vector $\boldsymbol{\beta}_i$.

Typical birefringence values of early 1990s fiber are $\Delta n/n \sim 10^{-7}$ which corresponds to a beat length, a commonly reported length scale of the birefringence, $L_B = \lambda_0/\Delta n \approx 20$ m at a wavelength of 1550 nm.

The birefringence of a specific fiber section, equation (1.27), means that the two principal polarization directions, $\boldsymbol{r}_\pm$, travel at different speeds down the fiber. This time delay is called the differential group delay (DGD), $\Delta\tau$, and the DGD per unit length can be obtained from differentiating the magnitude of (1.27) with respect to the frequency

$$\begin{aligned} \frac{\Delta\tau}{L} &= \frac{d}{d\omega}|\boldsymbol{\beta}| \\ &= \frac{\Delta n}{c} + \frac{\omega}{c}\frac{d\Delta n}{d\omega} \quad . \end{aligned} \tag{1.30}$$

When fibers become long enough, the birefringence can no longer be described by a single, homogeneous birefringence vector, $\boldsymbol{\beta}$, acting over the entire length [6, 10–12]. Instead, the fiber can be broken into N sections with their own birefringence vector, $\boldsymbol{\beta}_i$, as shown in the schematic of figure 4. In general, each section's birefrigence vector $\boldsymbol{\beta}_i$ is randomly oriented on the Poincarè sphere with differing magnitudes. Since each section has a different fast and slow polarization propagation mode, that might add or subtract from the prior sections, the DGD is no longer linear with respect to the propagation length, L. A statistical treatment is needed for the analysis of birefringence over the whole of the fiber length to get the collective behavior. When more than one concatenated birefringent sections are put together we begin to enter the study of polarization mode dispersion (PMD). For long fibers, with many randomly oriented birefringent sections, the

DGD grows as the square root of the L

$$\Delta\tau_{RMS}=\sqrt{\langle\Delta\tau^2\rangle}=D_p\sqrt{L} \tag{1.31}$$

where D_p is often termed the PMD parameter, where the expectation value is an ensemble average over all possible random configurations of $\boldsymbol{\beta}_i$. It is common to find single-mode fibers with D_p values in the range $0.1-0.3$ ps/km$^{1/2}$ and with the best fibers having D_p values less than 0.1 ps/km$^{1/2}$ for light in the telecom wavelength range of 1550 nm [13].

1.2.1 Time Varying Drift

After N sections of birefringent elements, shown in figure 4, an overall birefringence can be attributed to the fiber. Ignoring the frequency behavior of PMD the total polarization transformation on the state can be considered unitary. This implies that the inner angle between polarizations at different frequencies remains the same. This assumes the bandwidth of the signals propagating is relatively narrow and the fiber propagation distances are not sufficiently large where the cumulative PMD effects are significant. If the overall birefringence is caused by the environment, it is natural to assume the direction and magnitude will change over time due to the changing temperature and mechanical vibrations the fiber is exposed to. A randomly changing birefringence can be modeled by sequences of random matrices [14]. For a given snapshot in time, t_j, the unitary transform given by equation (1.20) is

$$\hat{\boldsymbol{U}}_F(\boldsymbol{\beta}(t_j))=\hat{\boldsymbol{I}}_2\cos|\boldsymbol{\beta}|-i(\boldsymbol{b}\cdot\boldsymbol{\sigma})\sin|\boldsymbol{\beta}| \tag{1.32}$$

where $\boldsymbol{\beta}(t_j)=|\boldsymbol{\beta}|\boldsymbol{b}$ is the current birefringence vector at that time, t_j, and $\boldsymbol{b}=(b_1,b_2,b_3)$ is a unit vector in Stokes space that points along the direction of $\boldsymbol{\beta}(t_j)$. Each of the three elements

within $\boldsymbol{\beta}=(\beta_1,\beta_2,\beta_3)$ are random variables from a zero-mean Gaussian distribution with standard deviation $\sigma_p^2=2\pi\Delta_p T$ where T is the measurement integration time and Δ_p is the polarization line width or the speed at which the polarization drifts per integration period. At time t_k the total polarization unitary transform from all previous time steps, $t_0,t_1,...,t_{k-1}$, is given by the recursive equation

$$\hat{\boldsymbol{U}}_{F,t_k}=\hat{\boldsymbol{U}}_F(\boldsymbol{\beta}(t_k))\hat{\boldsymbol{U}}_{F,t_{k-1}} \quad . \tag{1.33}$$

This produces a random walk on the Poincaré sphere shown in figure 5.

Experimentally, one can measure the polarization drift speed to reach some error rate [15]. This is defined as the

$$P_{ds}=\cos^{-1}(\boldsymbol{S}(t_k+\tau)\cdot\boldsymbol{S}(t_k))/\tau \tag{1.34}$$

with units rad/s, where τ is the drift time due to a given variation angle $\cos^{-1}(\boldsymbol{S}(t_k+\tau)\cdot\boldsymbol{S}(t_k))$. The error between two polarization signals that are meant to be coaligned is

$$\text{Error}=1-|\langle j_1|j_2\rangle|=\frac{1-\boldsymbol{S}_1\cdot\boldsymbol{S}_2}{2}=\frac{1-\cos\theta_{12}}{2} \tag{1.35}$$

where θ_{12} is the angle between Stokes vectors $\boldsymbol{S}_1$ and $\boldsymbol{S}_2$ with corresponding Jones vectors $|j_1\rangle$, $|j_2\rangle$. If the goal is to keep the polarization drift below a certain error threshold, e_{th}, then the critical polarization drift speed to hit the error threshold is

$$P_{ds}=\cos^{-1}(1-2e_{th})/\tau_{e_{th}} \tag{1.36}$$

where $\tau_{e_{th}}$ is the time it took to go from zero error to e_{th}. In order to reduce any accumulated error due to polarization drift a polarization controller and measurement system must be able to correct on time scales shorter than P_{ds}^{-1}. Ding *et al* proposed that any polarization control technique

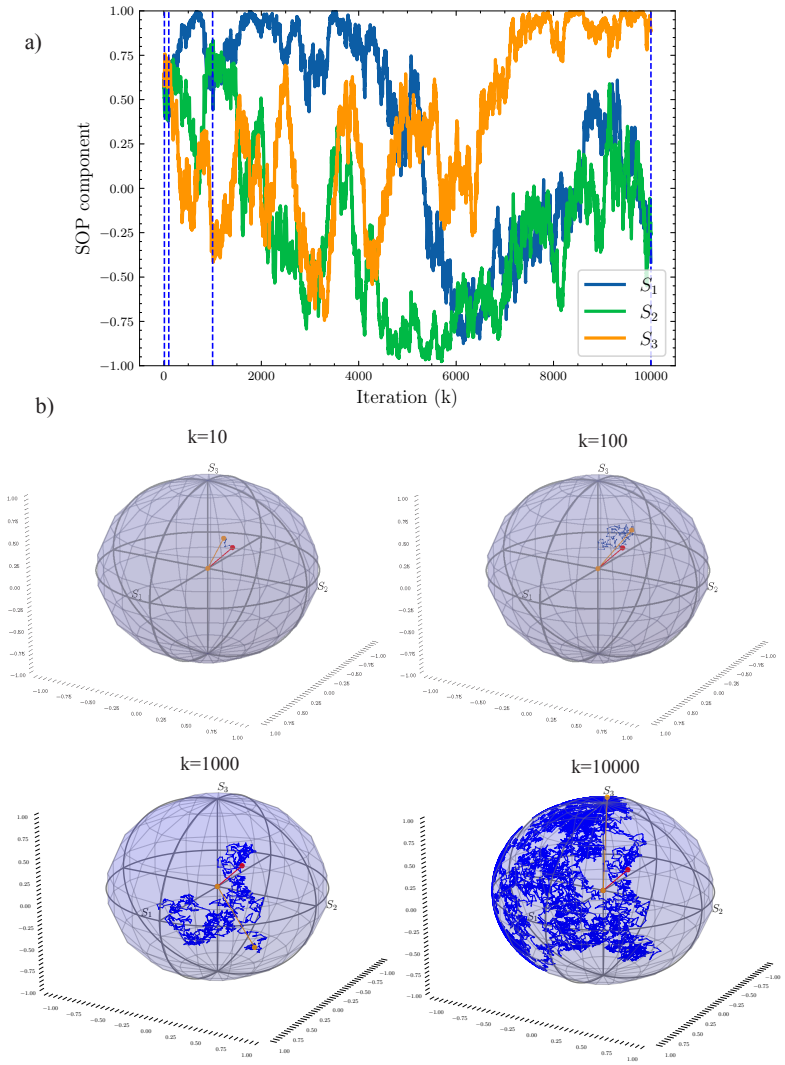

Figure 5: Polarization random walk on the Poincaré sphere produced from random unitaries (1.32). In the simulation, we set the initial polarization to $\boldsymbol{S}_0{=}1/\sqrt{3}(1,1,1)$ with $T{=}1$ and $\Delta_p{=}10^{-4}$. a) The state of polarization (SOP) Stokes vector components as a function of time, $\boldsymbol{S}(t_k){=}(S_1,S_2,S_3){=}\hat{\boldsymbol{U}}_{F,t_k}\boldsymbol{S}_0$. The dotted lines represent time step $t_j{=}\{t_{10},t_{100},t_{1000},t_{10000}\}$. b) Snapshots of the evolution of $\boldsymbol{S}_0$ at time steps $t_j{=}\{t_{10},t_{100},t_{1000},t_{10000}\}$. The red vector is the initial point, $\boldsymbol{S}_0$, the orange vector is $\boldsymbol{S}(t_k)$, and the blue trace is the k random kicks/steps the polarization took to get from the initial to final orientation.

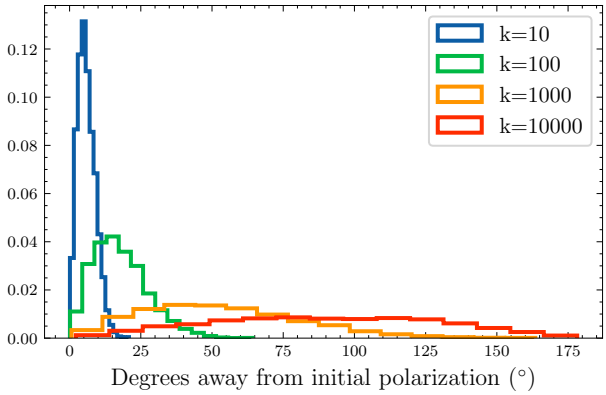

Figure 6: Histogram of the inner angle between the initial polarization $\boldsymbol{S}_0=\frac{1}{\sqrt{3}}(1,1,1)$ and the final polarization $\hat{\boldsymbol{U}}(t_k)\boldsymbol{S}_0$ for 5000 different polarization drifts. As time progresses, $k\gg1$, then the polarization state statistically covers the surface of the Poincaré sphere evenly.

should meet the requirement that

$$v\geq\langle P_{ds}\rangle+3\sigma \tag{1.37}$$

where v is the required real-time tracking speed of a polarization controller, $\langle P_{ds}\rangle$ and σ are the mean and standard deviation of the polarization variation speed, respectively [15]. Using the simulated data from the prior figure 5 with e_{th}=5%, T=1, and $\Delta_p=10^{-4}$ the average P_{ds} over the course of the k=10000 iterations was $\langle P_{ds}\rangle=3.69\times10^{-7}$ with $\sigma=2.79\times10^{-7}$. The histogram of this drift speed over the course of the k=10000 iterations is shown in figure 7. Even when the polarization linewidth is $\Delta_p=1e{-}4$ the drifting speed our controllers must be able to track is $v\geq1.20\times10^{-6}$ if we can tolerate up to 5% error.

The statistical modeling of polarization drift has shown that the correlation between two polarizations with the same frequency, but at different times t_1 and t_2, can be related to the PMD coefficient of equation (1.31). The correlation is

$$\langle\boldsymbol{S}(t_1,\omega)\cdot\boldsymbol{S}(t_2,\omega)\rangle=\exp\left\{-\frac{|t_2-t_1|}{2t_0/(2\omega^2D_p^2L)}\right\} \tag{1.38}$$

where t_0 is the drift time due to the index of refraction difference of the fast and slow fiber

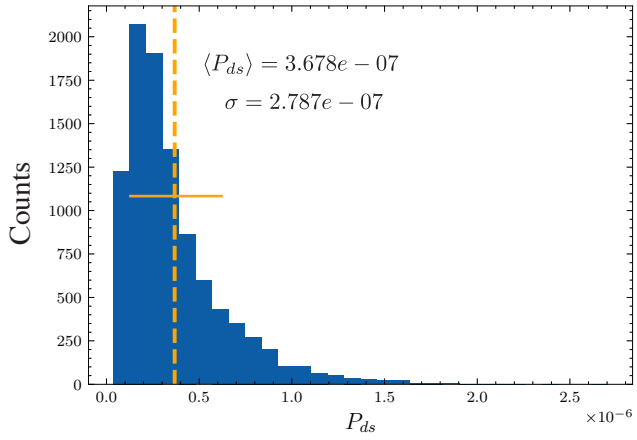

Figure 7: Statistical analysis of the polarization drift speed of figure 5a for a e_{th}=5%. The averaged drift speed over the k=10000 data set was $\langle P_{ds} \rangle$=3.678e−7 with a standard deviation of σ=2.787e−7.

axis, unique to any fiber span of length L, and needs to be experimentally measured [16]. The decorrelation time, or drift time t_d can be defined as t_d=$2t_0/(2\omega^2 D_p^2 L)$ where $\langle \boldsymbol{S}(t,\omega)\cdot\boldsymbol{S}(t+t_d,\omega)\rangle$= $1/e$.

Additionally, the correlation between two polarizations with different frequencies at time t depends on the frequency spread

$$\langle \boldsymbol{S}(t,\omega_1)\cdot\boldsymbol{S}(t,\omega_2)\rangle = \exp\left\{-\frac{\Delta\tau_{RMS}^2(\omega_2-\omega_1)^2}{3}\right\} \quad . \tag{1.39}$$

This last equation is important within the discussion of how correlated an aligning pilot tone signal at ω_1 is to your quantum signal at ω_2 over long fiber spans.

Table 1 reports the polarization drifting rates of various deployed fibers reported in the literature using the drift time $\langle \tau \rangle_{e_{th}}$ of (1.36) or the drift time t_d of equation (1.38).

1.3 Methods for Drift Compensation with Quantum Signals

Drifting polarization in fiber is not a new problem and was first documented in the 70s and 80s by Imai, Harmon, Poole, and Wagner in several research papers [10, 11, 22, 23]. They noted

Polarization Drifts			
Author	Environment	Length (km)	Drift Times
Ding et al.[17] Ding et al. [17] Ding et al.[17] Ding et al.[17]	Underground Underground Underground Aerial	23.3 69.7 85.1 1.78	$\langle\tau\rangle_{e_{th}=5\%}$=402.3 s $\langle\tau\rangle_{e_{th}=5\%}$=6.12 s $\langle\tau\rangle_{e_{th}=5\%}$=1.07 s $\langle\tau\rangle_{e_{th}=5\%}$=15 s
Waddy et al. [18]	Aerial	6.5	t_d=10 ms
Karlsson et al. [16]	Underground	127	t_d=3 days
Imai et al. [10] Imai et al. [10]	Underground Submarine	21.8 10	t_d=10 hours t_d=1 hour
Poole et al. [11]	Lab	31.6	t_d=30 minutes
De Angelis et al. [19]	Aerial	48	t_d=5 minutes
Zhang et al. [20]	Submarine	240	t_d=5 minutes
Li et al. [21]	Aerial	48	t_d= 10 ms

Table 1: Reported polarization drifts within the literature.

that the polarization of fiber, even in still laboratory conditions drifted over the course of hours to days. In the 80s and 90s new electronically controlled polarization controllers were developed to correct for the drifting polarization of classical signals [24–29].

In our application, we seek to control or compensate for fiber polarization drift when quantum light is transmitted over fiber. Because the streams of photons are too weak for conventional polarimetry measurements, often alignment signals that are strong enough to be recorded by polarimeters are multiplexed along the same fiber in either wavelength or time with the quantum signal. Examples of these are shown in figure 8a-b. For reference, our entanglement source generates 10^6 photon pairs per second, but due to photon losses through the filters, controllers, splices/connectors, and the fiber path itself, common count rates are in the 10^3-10^4 per second at the detectors. Although these photons are statistically unpolarized their signal would not register on our polarimeter (Agilent N7788B) because it has a lower-end sensitivity of -50 dBm or 10^{11} photons per second at 1550 nm.

In figure 8a the alignment signals, $\lambda_{1,2}$, are usually separated by a constant wavelength above and below the wavelength of the quantum signal, λ_q

$$\lambda_{1,2}=\lambda_q\pm\Delta\lambda \quad .$$

The alignment signals are sent down the same fiber path as the quantum signals through a wavelength multiplexer. The alignment signals are then demultiplexed where the H/V and D/A polarizations of $\lambda_{1,2}$ are recorded on a polarimeter and if they have drifted from $\hat{\boldsymbol{s}}_{1,2}$ then upstream polarization controllers correct for the drift. However, for longer fiber spans, PMD can cause the polarization of the quantum and alignment signals to become uncorrelated. Using (1.39) into (1.35) the angular separation and probability of error between two coaligned signals, separated by $\Delta\omega$ after propagating down a fiber of length L is [30]

$$\begin{aligned}\theta_{RMS}&=\arccos\left(-\Delta\tau_{RMS}^2\Delta\omega^2/3\right)\\ P_{err}&=\frac{1-\exp\left\{-\Delta\tau_{RMS}^2\Delta\omega^2/3\right\}}{2}=\frac{1-\exp\left\{-D_p^2L\Delta\omega^2/3\right\}}{2}\end{aligned} \quad . \tag{1.40}$$

As an example for D_p=0.1 ps/km$^{1/2}$, $\Delta\lambda$=5 nm $\rightarrow\Delta\omega$=3.9$\times10^{12}$rad/sec for λ=1550nm, and for fiber propagation length, L=10 km, the expected error rate due to lost polarization correlation is P_{err}=20%. In addition, the wavelength multiplexer and demultiplexer must have high filtering and extinction so that the classical power signals do not leak into the quantum channel and cause measurement errors or blind the detectors. The limitation of transmission distance for differing wavelength pilot tones and high isolation requirements between WDM channels is a hurdle for this mode of polarization drift correction. To combat these issues, smaller $\Delta\lambda$ values with high-quality WDM and fiber with lower D_p can be used.

Figure 8b and 8c show two different types of time division multiplexed polarization drift

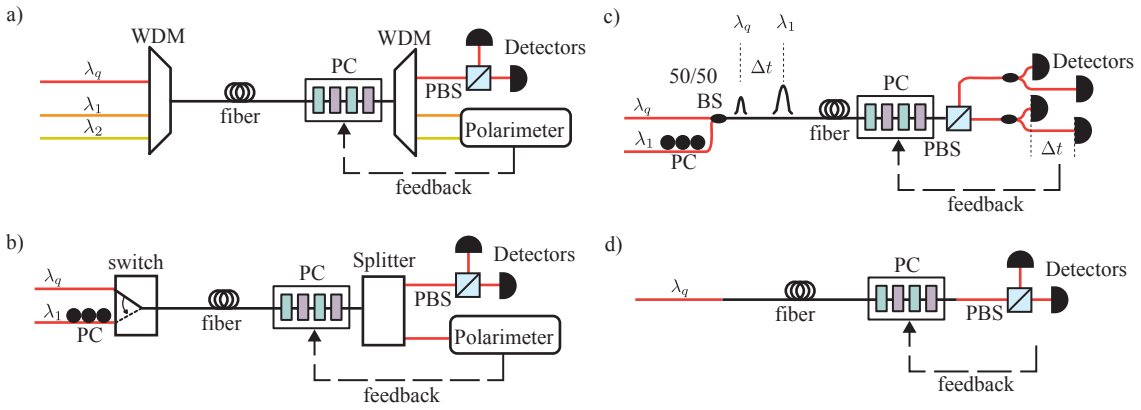

Figure 8: Representative experimental figures for how quantum polarization drift is corrected for using measurement feedback. a) Wavelength division multiplexed strategy. b) Interruption based time division multiplexed strategy. c) Continuous time division multiplexed strategy. d) Quantum signal based strategy. WDM = wavelength division multiplexer, PC = polarization controller, PBS = polarization beam splitter, BS = beam splitter. The color of the fiber is used to indicate the wavelength of light being sent down it.

strategies. In 8b, either at regular intervals or when an error marker is hit at the receiver side, the quantum signal is switched off, and the aligning pilot tone is turned on. The alignment signal, λ_1, at the same wavelength as the quantum signal, switches between polarizations H/V and D/A for the upstream PC to adjust according to the polarimeter measurements. Once alignment has been restored the quantum signal is turned back on. This interruption based polarization drift compensation fundamentally reduces the rate at which photons can be sent from the send to the receiver due to the downtime from the classical signal alignment. In this configuration, additional measures need to be taken to protect the quantum detectors from blinding due to the classical power of the alignment signals and the detectors used.

In 8c, the alignment signals are much weaker, but still strong relative to the quantum signals with which they are copropagating. The alignment signal's power can be configured so that n numbers of photons per pulse, on average, arrive within an alignment signal pulse. As the alignment pulse no longer blinds the detectors, the same detectors can be used to measure both the quantum and alignment signals. The alignment signals are pulsed with a temporal separation

of Δt from the quantum signal. After polarization projection by a PBS, a 50/50 beamsplitter directs the photons to two temporally separated detectors. Assuming the alignment signal is well polarized and an order of magnitude, or more, larger than the quantum signal, the single photon count rates, to first order, determine the alignment signal polarization orientation. Whereas the coincidence detection from events at the interarrival time of t_{int}=0 or t_{int}=2Δt corresponds to the detection of photons from the alignment and quantum signals. Knowledge of the polarization state of the alignment signal can be used in feedback with the upstream polarization controller. Gating of detectors can improve the signal-to-noise ratio of the quantum signal detection. In addition, a pulsed alignment signal can be used for clock recovery, another problem for quantum fiber networks for synchronizing events at distant locations [31]. The drawbacks of this method are alignment signal leakage and laser repetition rate limitations [30]. Additionally, common photon detectors used in this time-gated setup are avalanche photodiodes (APD), which can place constraints due to their deadtime and aterpulse effects [32, 33].

A different strategy, shown in figure 8d, has been explored in the past several years to reduce the complexity of multiplexing alignment signals in time or wavelength by using only measurements on the quantum signal for feedback for the correction of polarization drift. This alignment strategy has the advantage of reduced experimental complexity, as it requires fewer optical elements. One problem with this method is the lower count rate of the quantum signals and the larger integration time required for a given measurement. The number of photons in a fiber of length L decreases as $10^{-\alpha L/10}$ where α is the attenuation due to propagation expressed in dB per km. Low loss single mode fibers for wavelengths near 1550 nm have common transmission losses of α=0.1$-$0.3 dB/km. As an example, for fibers with α=0.2 dB/km only 1% of the photons survive to the receiver after traveling 100 km. Often these transmission losses are only a part of the total losses due to experimental component losses, lossy fiber connections and splices, and

free space couplings. Longer integration times mean that the speeds of drifts these strategies can correct for using feedback strategies are inherently slower. The methods we developed, shown in chapter 3, work using the feedback from entangled photons and work to correct the relative drift between two user's measurement bases [1].

Once a polarization alignment measurement or objective function has been identified, there are many different alignment algorithms used on the polarization controllers from the feedback signals. If the polarization transformations of the polarization controllers are known from prior calibration then analytic solutions to undo the polarization misalignment may be performed [34–39]. If the polarization controllers are not calibrated, or if the polarization controllers themselves are subject to slow drift in their actuation, iterative techniques can be used where the polarization controller settings are varied by an algorithm until the polarization drift is corrected in a convergent fashion [31, 40–43]. The mechanisms for how our polarization controllers work and the algorithms we used for measurement base alignment are provided in the following chapters. Table 2 reports some of the quantum experiments correcting for polarization drift within their fiber paths. The feedback methods, with some variations, all roughly fit into the four methods shown above with abbreviations: WDM=wavelength division multiplexed, ITDM=interruption time division multiplexed, TDM=time division multiplexed, and QM=quantum signal based. While all compensation speeds depend on the feedback mechanism, the polarization control algorithm, the repetition rate of the alignment signals, the length of the fiber/losses, the speeds of the polarization controller, etc. the table 2 gives a reference for the compensation speeds people have reported in the literature.

Polarization Drifts Compensation with Quantum Signals				
Author	Environment	Fiber Length (km)	Method	Compensation Speed
Xavier et al. [34]	Lab	8.6	WDM	10 ms
Xavier et al. [35]	Lab	16	WDM	5 ms
Chen et al. [44]	Lab	50	TDM	1-2 min
Treiber et al. [40]	Lab	25	ITDM	1-2 minutes
Li et al. [21]	Aerial	45	WDM	1-5 ms
Wengerowsky et al. [45]	Submarine	96	ITDM	1-2 minutes
Ding et al. [41]	Lab	50	QM	1 minutes
Agnesi et al. [31]	Lab	26	QM	10 s
Peranić et al. [42] Peranić et al. [42] Peranić et al. [42]	Lab Lab Lab	1.6 1.6 1.6	TDM ITDM QM	8 minutes 6 minutes 2 minutes
Shi et al. [43]	Underground	10	QM	20 minutes
Dowling et al. [1]	Underground	7.1	QM	10 minutes

Table 2: Polarization drift compensation strategies within the literature.

1.4 Polarization of Photons

> I can't define a photon, but I know one when I see one.
>
> Roy J. Glauber

Several novel experiments done in the 1970s tell us that the classical description of electromagnetic waves isn't complete and instead reveal that the electromagnetic field is transmitted by discrete bundles of energy termed photons [46, 47]. In classical electrodynamics, polarization is defined as the orientation of the electric field of an electromagnetic wave, seen in equation (1.2), but for single photons, polarization is an inherent property due to the fact they are spin-1 bosons. This intrinsic spin angular momentum measured along the direction of motion is found to be $\hbar$, Plank's constant, corresponding to the right and left circular polarization we discussed earlier. As we have

seen right- and left-circularly polarized light can be expressed in terms of the linear horizontal and vertical polarization bases. The most general polarization state of a single photon $|\psi\rangle$, a realization of a qubit, can be expressed as a linear combination of perpendicular polarization bases existing in superposition.

1.4.1 Notation for Quantum Objects

Before stating the mathematical description of a photon we must have a brief overview of the mathematical notation used to describe and measure a quantum state. The physical state of a quantum object's polarization (or any other degree of freedom) is determined by its complex state vector $|\psi\rangle$ in a Hilbert space. This vector is called a ket, following the notation invented by Dirac, and is postulated to contain the complete information about the physical state. The exact Hilbert space is dependent on the system being studied, but in general is defined as the total phase space for all normalizable complex state vectors, i.e. any vector that satisfies

$$\langle\alpha|\alpha\rangle=1$$

is within a Hilbert space. Here, $\langle\alpha|$, is the bra vector dual to the ket $|\alpha\rangle$. Computationally, the dual bra is the complex conjugate transpose of the ket vector.

An observable, $\hat{A}$, such as the electric field direction of a photon, is represented as a Hermitian operator that transform one ket to a new ket

$$\hat{A}|\psi\rangle=|\phi\rangle \quad . \tag{1.41}$$

Normalized eigenkets of an observable form a complete orthonormal set, $\{\alpha_i\}$, and any ket can

be spanned by a linear combination of these special kets

$$|\psi\rangle=\sum_{\alpha_i} k_{\alpha_i}|\alpha_i\rangle=\begin{pmatrix}\langle\alpha_1|\psi\rangle\\ \langle\alpha_2|\psi\rangle\\ \vdots\\ \langle\alpha_N|\psi\rangle\end{pmatrix}=\begin{pmatrix}k_{\alpha_1}\\ k_{\alpha_2}\\ \vdots\\ k_{\alpha_N}\end{pmatrix} \tag{1.42}$$

where k_{α_i} are complex constants, and for simplicity, we assumed a finite dimension Hilbert space of length N.

Operationally, each ket (and bra) vector has an inner and outer product operation that has been used above, but now is rigorously defined as

$$\begin{aligned}\langle\alpha|\beta\rangle&=\begin{pmatrix}\alpha_1^* & \alpha_2^* & \cdots & \alpha_N^*\end{pmatrix}\begin{pmatrix}\beta_1\\ \beta_2\\ \vdots\\ \beta_N\end{pmatrix}=\alpha_1^*\beta_1+\alpha_2^*\beta_2+\cdots+\alpha_N^*\beta_N\\ |\beta\rangle\langle\alpha|&=\begin{pmatrix}\beta_1\\ \beta_2\\ \vdots\\ \beta_N\end{pmatrix}\begin{pmatrix}\alpha_1^* & \alpha_2^* & \cdots & \alpha_N^*\end{pmatrix}=\begin{pmatrix}\beta_1\alpha_1^* & \beta_1\alpha_2^* & \cdots & \beta_1\alpha_N^*\\ \beta_2\alpha_1^* & \beta_2\alpha_2^* & \cdots & \beta_2\alpha_N^*\\ \vdots & \ddots & & \vdots\\ \beta_N\alpha_1^* & \beta_N\alpha_2^* & \cdots & \beta_N\alpha_N^*\end{pmatrix}.\end{aligned} \tag{1.43}$$

Here, we see that the inner product is a complex number, and the outer product is a $N\times N$ matrix that functions equivalently as an operator.

When measurements are performed we can calculate the probability of detecting a specific

eigenstate $|\alpha_j\rangle$ from Born's rule

$$\begin{aligned} \mathrm{P}(|\alpha_j\rangle) &= |\langle\alpha_j|\psi\rangle|^2 = \Big(\langle\psi|\alpha_j\rangle\Big)\Big(\langle\alpha_j|\psi\rangle\Big) = \langle\psi|\Big(|\alpha_j\rangle\langle\alpha_j|\Big)|\psi\rangle \\ &= \langle\ |\alpha_j\rangle\langle\alpha_j|\ \rangle = |k_{\alpha_j}|^2 \quad . \end{aligned} \tag{1.44}$$

Above we used the notation $\left\langle \hat{A} \right\rangle = \langle\psi|\hat{A}|\psi\rangle$ that is often labeled as the expectation value of a measurement operator, $|\alpha_j\rangle\langle\alpha_j|$. For all the coefficients k_{α_i} within (1.43) to make sense, given Born's rule, the total probabilities must add to unity

$$\sum_i^N |k_{\alpha_i}|^2 = 1 \quad . \tag{1.45}$$

The collapse of the wavefunction due to measurement and determining that the state was in $|\alpha\rangle$ can be mathematically written as

$$|\psi\rangle \xrightarrow[\text{measurement}]{\text{projective}} |\alpha\rangle = \frac{(|\alpha\rangle\langle\alpha|)|\psi\rangle}{(\langle\psi|(|\alpha\rangle\langle\alpha|)|\psi\rangle)^{1/2}} \quad . \tag{1.46}$$

This update rule is useful for the description of the polarization of your photons after a polarizer oriented to, in this case, the α polarization direction.

1.4.2 Polarization Qubits

While there are three special bases for polarization: horizontal(H)/vertical(V), diagonal(D)/anti-diagonal(A), and right(R)/left(L) circular, in any basis polarization is described as a two-dimensional superposition

$$|\psi\rangle = a|\alpha\rangle + b|\alpha_\perp\rangle \quad . \tag{1.47}$$

Because of this, the polarization of a single photon is often the prototypical example of a physical qubit, the quantum analog of a classical bit. A classical bit is represented by a binary system, 0 or 1, where the prototypical classical bit is the conducting or nonconducting state of a transistor. The photon's polarization exists in a superposition of being in state $\boldsymbol{\alpha}$ with probability $|a|^2$ and $\boldsymbol{\alpha}_\perp$ with probability $|b|^2{=}1{-}|a|^2$. If we defined the state $|\alpha\rangle$ as "on" and $|\alpha_\perp\rangle$ as "off," the ability for a quantum bit to be in a superposition of "on" AND "off" is dramatically different than a classical bit, described by classical physics, where it must be either "on" OR "off," and never can be some combination of the two at the same time. Superposition combined with the inherent role of probability within measurement is often one's first departure from classical physics lines of thought.

Through the second quantization of the electromagnetic field, a single photon can be described by the action of a creation operator acting on the (zero-photon) vacuum state $|0\rangle$. The polarization qubit in the three special bases mentioned above can be written

$$\begin{aligned} |\psi\rangle &= \left(k_H \hat{a}_H^\dagger + k_V \hat{a}_V^\dagger\right)|0\rangle \\ &= \left(k_D \hat{a}_D^\dagger + k_A \hat{a}_A^\dagger\right)|0\rangle \\ &= \left(k_R \hat{a}_R^\dagger + k_L \hat{a}_L^\dagger\right)|0\rangle \end{aligned} \tag{1.48}$$

where $k_{H,V,D,A,R,L}$ are constants with $|k_H|^2{+}|k_V|^2{=}|k_D|^2{+}|k_A|^2{=}|k_R|^2{+}|k_L|^2{=}1$ and $\hat{a}_j^\dagger$ are creation operators that create a photon in polarization mode j. Creation and annihilation operators satisfy the commutation relation

$$[\hat{a}_i, \hat{a}_j^\dagger] = \delta_{ij} \tag{1.49}$$

where δ_{ij} is the Kronecker delta function that is zero when $i{\neq}j$ and one when $i{=}j$ for i,j in the basis H/V, D/A, R/L, or general $\boldsymbol{\alpha}/\boldsymbol{\alpha}_\perp$. The polarization qubit $|\psi\rangle$ can be written as a one-by-two

column vector like (1.6)

$$|\psi\rangle = \begin{pmatrix} \langle 0|\hat{a}_H|\psi\rangle \\ \\ \langle 0|\hat{a}_V|\psi\rangle \end{pmatrix} = \begin{pmatrix} k_H \\ \\ k_V \end{pmatrix} \tag{1.50}$$

The creation operators are related through the same relations that we saw for the electric field (Jones vector) and horizontal and vertical measurement bases (1.14):

$$\begin{aligned} \hat{a}_D^\dagger &= \frac{1}{\sqrt{2}}\left(\hat{a}_H^\dagger + \hat{a}_V^\dagger\right) & \hat{a}_R^\dagger &= \frac{1}{\sqrt{2}}\left(\hat{a}_H^\dagger + i\hat{a}_V^\dagger\right) \\ \hat{a}_A^\dagger &= \frac{1}{\sqrt{2}}\left(\hat{a}_H^\dagger - \hat{a}_V^\dagger\right) & \hat{a}_L^\dagger &= \frac{1}{\sqrt{2}}\left(\hat{a}_H^\dagger - i\hat{a}_V^\dagger\right) \quad . \end{aligned} \tag{1.51}$$

This relationship from creation to electric fields isn't by chance as the electric field operator is directly proportional to the creation operator

$$\begin{aligned} \hat{\boldsymbol{E}}(\boldsymbol{r},t) &= \sum_{\boldsymbol{k},\lambda} \boldsymbol{e}_{\boldsymbol{k}\lambda} \sqrt{\hbar\omega_k / 2\varepsilon_0 V}\left(\hat{a}_{\boldsymbol{k}\lambda}\exp[-i\chi_{\boldsymbol{k}}(\boldsymbol{r},t)] + \hat{a}_{\boldsymbol{k}\lambda}^\dagger \exp[i\chi_{\boldsymbol{k}}(\boldsymbol{r},t)]\right) \\ \chi_{\boldsymbol{k}}(\boldsymbol{r},t) &= \omega_k t - \boldsymbol{k}\cdot\boldsymbol{r} \end{aligned} \tag{1.52}$$

where $\boldsymbol{e}_{\boldsymbol{k}\lambda}$ is a unit vector, V is the volume of the cavity the field is in, and λ is one of the two orthogonal polarization modes. This can be derived explicitly through the comparison of the energy density of the electromagnetic field in a cavity to the quantum harmonic oscillator [47, 48].

So far we have only discussed pure polarization states like (1.48). Quantum mechanics also permits more classical mixtures of quantum states. Like a coin flip might produce heads or tails 50% of the time, a quantum source might produce one pure state or another with some probability. When we work to include both the superposition allowed within quantum pure states and their classical mixtures we get the most general form of a quantum state, a mixed state, $\hat{\rho}$. Consider a source that emits pure states $|\psi_1\rangle, |\psi_2\rangle, ..., |\psi_N\rangle$ with probability $p_1, p_2, ..., p_N$ then the mixed state

that describes this source is the density matrix

$$\hat{\rho}=\sum_{i=1}^{N} p_i|\psi_i\rangle\langle\psi_i| \quad . \tag{1.53}$$

The probability of a measurement yielding the outcome $|\alpha\rangle$ is given from trace of the measurement operator $|\alpha\rangle\langle\alpha|$ and $\hat{\rho}$

$$\mathrm{P}(\alpha)=\mathrm{Tr}\{\hat{\rho}|\alpha\rangle\langle\alpha|\} \tag{1.54}$$

and the state afterwards is updated to

$$\hat{\rho}_{\text{after}}=\frac{|\alpha\rangle\hat{\rho}\langle\alpha|}{\mathrm{Tr}\{\hat{\rho}|\alpha\rangle\langle\alpha|\}} \quad . \tag{1.55}$$

For mixed states that describe only one qubit, it is always possible to write the density matrix in the form

$$\hat{\rho}=\frac{1}{2}\left(\hat{I}_2+\boldsymbol{r}\cdot\hat{\boldsymbol{\sigma}}\right) \tag{1.56}$$

where $\hat{I}_2$ is the 2x2 identity matrix. If $|\boldsymbol{r}|=1$ we have a pure state and if $|\boldsymbol{r}|<1$ the state is mixed. A polarization transformation caused by rotation about rotation vector $\boldsymbol{a}$ and angle θ can be described by defining the component of $\boldsymbol{r}$ parallel to $\boldsymbol{a}$, $\boldsymbol{r}_{\|}=(\boldsymbol{r}\cdot\boldsymbol{a})\boldsymbol{a}$, and perpendicular to $\boldsymbol{a}$, $\boldsymbol{r}_{\perp}=\boldsymbol{r}-\boldsymbol{r}_{\|}$. Using those vectors and equation (1.20) the mixed state is transformed to

$$\hat{\rho}_{\text{rotated}}=\hat{U}\hat{\rho}\hat{U}^{\dagger}=\frac{1}{2}\left(I+(\boldsymbol{r}_{\|}+\cos\theta\boldsymbol{r}_{\perp}-\sin\theta(\boldsymbol{a}\times\boldsymbol{r}_{\perp}))\cdot\hat{\boldsymbol{\sigma}}\right) \quad . \tag{1.57}$$

Moving to two qubits sent to two observers Alice and Bob, the most general density matrix

description of that system is with Stokes vectors $\boldsymbol{a}$ and $\boldsymbol{b}$ for each respective qubit

$$\hat{\rho}=\frac{1}{4}\Big(\hat{I}_2\otimes\hat{I}_2+\boldsymbol{a}\cdot\boldsymbol{\sigma}\otimes\hat{I}_2+\hat{I}_2\otimes\boldsymbol{b}\cdot\boldsymbol{\sigma}+\sum_{j=1}^{3}\sum_{k=1}^{3}T_{jk}\hat{\sigma}_j\otimes\hat{\sigma}_k\Big) \tag{1.58}$$

where $|\boldsymbol{a}|\leq 1$ and $|\boldsymbol{b}|\leq 1$, $\otimes$ is the tensor product linking the Hilbert space of qubit $\boldsymbol{a}$ and Hilbert space of qubit $\boldsymbol{b}$, and T_{jk} are the coupling coefficients between the two qubits that contain the special quantum correlations, termed quantum entanglement.

1.5 Quantum Entanglement

> "... I would not call that 'one' but rather 'the' characteristic trait of quantum mechanics, the one that enforces its entire departure from classical lines of thought. By the interaction, the two representatives have become entangled."
>
> Erwin Schrödinger

As we have seen from the prior section, quantum mechanics forces us to acknowledge the fundamental role superposition, probability, and measurement have in how the world operates at the quantum level. Nevertheless, as we begin to comprehend the peculiar nature of single-qubit quantum mechanics, nature unveils yet another counterintuitive attribute for two or more particles: quantum entanglement. Loosely described, quantum entanglement is the phenomenon that occurs when groups of particles cannot be described independently but rather must be described as a collection of the group's shared properties.

As we will see, when two photon's polarizations are perfectly entangled, there is no information

when looking at the polarization of any one photon, yet the measurement of both reveals perfect correlation 100% of the time (when measured correctly), even when the photons might be measured independently across vast distances. These quantum collective correlations allow for special and "stronger" correlations than can exist classically and, to some physicists, are the primary departure of quantum mechanics from classical physics.

Entanglement and correlated behavior between qubits can be stated more succinctly for pure two-qubit states. The most general pure two-particle polarization ket can be expressed as

$$|\psi\rangle = k_{HH}|H_1\rangle|H_2\rangle + k_{HV}|H_1\rangle|V_2\rangle + k_{VH}|V_1\rangle|H_2\rangle + k_{VV}|V_1\rangle|V_2\rangle \tag{1.59}$$

where $\sum|k_i|^2=1$ and for simplicity we use the notation $|j\rangle = \hat{a}_j^\dagger|0\rangle$ and $|j\rangle_1|k\rangle_2 = |j\rangle_1 \otimes |k\rangle_2$ and $\otimes$ is the tensor product. The ket $|\psi_1\rangle|\psi_2\rangle$ can be represented as a 4x1 state vector

$$|\psi_1\rangle|\psi_2\rangle = \begin{pmatrix} a \\ b \end{pmatrix} \otimes \begin{pmatrix} c \\ d \end{pmatrix} = \begin{pmatrix} ac \\ ad \\ bc \\ bd \end{pmatrix} \quad . \tag{1.60}$$

The general two-qubit state, equation (1.59), is entangled if it cannot be rewritten in the factorized form

$$|\psi\rangle = (\alpha_H|H_1\rangle + \alpha_V|V_1\rangle) \otimes (\beta_H|H_2\rangle + \beta_V|V_2\rangle) \quad . \tag{1.61}$$

Equation (1.61) describes a perfectly separable state where the first qubit has no coupling to the state of the second qubit, and, therefore, no special quantum correlations are present. This is only

possible if the coefficients within (1.59) are related to one another by

$$k_{HH}=\alpha_H\beta_H \quad k_{HV}=\alpha_H\beta_V \quad k_{VH}=\alpha_V\beta_H \quad k_{VV}=\alpha_V\beta_V \quad . \tag{1.62}$$

However, it doesn't take much playing around with (1.59) to see this is impossible for some chosen k_i values. For instance, suppose we let $k_{HH}=k_{VV}=0$ and $k_{HV}=-k_{VH}=1/\sqrt{2}$. This is a perfectly valid, normalized, two-qubit state, but if k_{HH} and k_{VV} are zero, then either α_H or β_H are zero and likewise either α_V or β_V are also zero. However, this means that for whichever pair you pick k_{HV} and k_{VH} will be zero from (1.62) when we have required them to be $k_{HV}=-k_{VH}=1/\sqrt{2}$. Therefore, it is impossible to write such a state in an unentangled/factorized form. This entangled state, written in its ket form is

$$|\psi\rangle=\frac{1}{\sqrt{2}}\Big(|H_1\rangle|V_2\rangle-|V_1\rangle|H_2\rangle\Big) \quad . \tag{1.63}$$

If a measurement were to be done on just the first photon the probability of finding it in the horizontal or vertical polarization state is

$$\begin{aligned} P_1(|H\rangle)&=\sum_{j\in\{|H_2\rangle,|V_2\rangle\}}|\langle H_1|\langle j|\psi\rangle|^2=\frac{1}{2} \\ P_1(|V\rangle)&=\sum_{j\in\{|H_2\rangle,|V_2\rangle\}}|\langle V_1|\langle j|\psi\rangle|^2=\frac{1}{2} \end{aligned} \tag{1.64}$$

meaning its equality likely to be horizontally or vertically polarized. But the probability of observing anti-correlated polarization states (one being horizontally polarized and the other being vertically polarized) is

$$P_{\text{anti}}=P(|H_1\rangle|V_2\rangle)+P(|V_1\rangle|H_2\rangle)=|\langle H_1|\langle V_2|\psi\rangle|^2+|\langle V_1|\langle H_2|\psi\rangle|^2=1 \quad . \tag{1.65}$$

Therefore, while there is no information when looking at the single photon count rates there is still correlated information when comparing which polarization was observed for both photons.

While an infinite number of entangled states exist, the special coefficients I chose creates one of the four maximally entangled states (and the one we ideally generate in the lab), named the Bell states

$$\begin{aligned} \left|\Psi^-\right\rangle &= \frac{1}{\sqrt{2}}\left(|H\rangle_a|V\rangle_b - |V\rangle_a|H\rangle_b\right) \qquad \left|\Psi^+\right\rangle = \frac{1}{\sqrt{2}}\left(|H\rangle_a|V\rangle_b + |V\rangle_a|H\rangle_b\right) \\ \left|\Phi^-\right\rangle &= \frac{1}{\sqrt{2}}\left(|H\rangle_a|H\rangle_b - |V\rangle_a|V\rangle_b\right) \qquad \left|\Phi^+\right\rangle = \frac{1}{\sqrt{2}}\left(|H\rangle_a|H\rangle_b + |V\rangle_a|V\rangle_b\right) \quad . \end{aligned} \tag{1.66}$$

1.5.1 Entanglement Measures

To quantify the amount of entanglement present in a quantum state, one can define an entanglement monotone or a nonnegative function that increases in the presence of more entanglement but does not increase under local operations and classical communication [49]. There are several entanglement functions people have developed to quantify quantum entanglement, such as entanglement entropy, entanglement of formation, concurrence, tangle, and negativity, to name a few. While two qubit entanglement quantifiers are well understood, in general, for high dimensional quantum systems with large numbers of interacting particles, describing quantum entanglement is still an active area of research.

For two interacting qubits, their shared entanglement is well defined. Following Wootters derivation for entanglement of formation and concurrence [50], we start by looking at the 'polarization flip' transformation for a single particle. For an arbitrary one-qubit mixed state, $\hat{\rho}$, the polarization-flipped mixed state is

$$\hat{\rho} \rightarrow \hat{\tilde{\rho}} = \hat{\sigma}_3 \hat{\rho}^* \hat{\sigma}_3 \quad , \tag{1.67}$$

where $\hat{\tilde{\rho}}$ is the polarization flipped state and $\hat{\rho}^*$ is the complex conjugate of $\hat{\rho}$. The action of $\hat{\sigma}_3$

on both sides of (1.67) acts to flip the sign of equation (1.56), i.e. $\hat{\tilde{\rho}}=\frac{1}{2}(\hat{I}_2-\boldsymbol{r}\cdot\boldsymbol{\sigma})$ [48]. This is extended to two qubits with the transform

$$\hat{\tilde{\rho}}=\left(\hat{\sigma}_3\otimes\hat{\sigma}_3\right)\hat{\rho}^*\left(\hat{\sigma}_3\otimes\hat{\sigma}_3\right) \tag{1.68}$$

The Hermitian matrix $\hat{R}$ ($\hat{R}=\hat{R}^\dagger$) of the two qubit density matrix is defined as

$$\hat{R}=\sqrt{\sqrt{\hat{\rho}}\hat{\tilde{\rho}}\sqrt{\hat{\rho}}} \quad . \tag{1.69}$$

The positive eigenvalues of $\hat{R}$ can be arranged in decreasing size: $\lambda_1,\lambda_2,\lambda_3,\lambda_4$. The concurrence, an entanglement measure, is then defined as

$$\mathcal{C}(\hat{\rho})=\max\left(0,\lambda_1-\lambda_2-\lambda_3-\lambda_4\right) \quad . \tag{1.70}$$

If $\mathcal{C}>0$ then there is entanglement in $\hat{\rho}$. For pure states $|\psi\rangle$ the concurrence equation (1.70) can be reduced to $\mathcal{C}(|\psi\rangle)=|\langle\psi|\bar{\psi}\rangle|$,where the polarization flipped state $|\bar{\psi}\rangle=\hat{\sigma}_3\otimes\hat{\sigma}_3|\psi\rangle$. For the maximally entangled Bell state, $|\Psi^-\rangle$, the polarization flip transform leaves the state unchanged (except for an overall minus sign), and the concurrence returns the maximal value $\mathcal{C}(|\Psi^-\rangle)=1$. Any value of $\mathcal{C}$ between 0 and 1 quantifies the degree of entanglement $\hat{\rho}$ has between its qubits.

The entanglement of formation monotone quantifies how much entanglement is needed to create the state $\hat{\rho}$, can be defined in terms of the concurrence

$$E_F(\hat{\rho})=-\left(\frac{1+\sqrt{1-\mathcal{C}^2}}{2}\right)\log_2\left(\frac{1+\sqrt{1-\mathcal{C}^2}}{2}\right)-\left(\frac{1-\sqrt{1-\mathcal{C}^2}}{2}\right)\log_2\left(\frac{1-\sqrt{1-\mathcal{C}^2}}{2}\right) \quad . \tag{1.71}$$

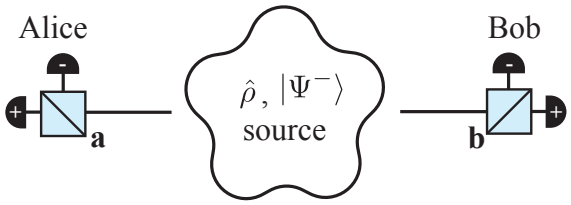

Figure 9: Nonlocal measurements on quantum state $\hat{\rho}$ by measurement projectors $\hat{A}=\boldsymbol{a}\cdot\hat{\boldsymbol{\sigma}}$ and $\hat{B}=\boldsymbol{b}\cdot\hat{\boldsymbol{\sigma}}$.

1.6 Bell Nonlocality

> ... the statistical predictions of quantum mechanics are incompatible with separable predetermination.
>
> John Bell

The 2022 Nobel Prize in Physics was awarded to John Clauser, Alain Aspect, and Anton Zeilinger for their experiments using entangled photons for, among other things, violating inequalities put forth by John Bell. The violation of these inequalities proved that quantum mechanics cannot be described by a local real theory. Instead, nonlocality appears fundamental to quantum mechanics, adding another tally to the departures from classical lines of thought.

To describe a quantum source from a local, real description let us examine a typical Bell experiment that can be performed when two photons from a source, $\hat{\rho}$, are distributed to two spatially separated observers, Alice and Bob, shown in figure 9. Alice and Bob are then able to perform a joint measurement using equation (1.54)

$$P(\boldsymbol{a},\boldsymbol{b})=\mathrm{Tr}\left\{\hat{\rho}\hat{A}\otimes\hat{B}\right\} \quad . \tag{1.72}$$

where $\hat{A}=\boldsymbol{a}\cdot\hat{\boldsymbol{\sigma}}$ and $\hat{B}=\boldsymbol{b}\cdot\hat{\boldsymbol{\sigma}}$ and $\boldsymbol{a}$ and $\boldsymbol{b}$ are the Stokes' measurement projection directions for their

polarization projecting PBS. The measurement outcomes are either to the positive detector, labeled with the $+$, or to the negative detector, $-$. To describe the anticorrelations discussed in section 1.5, i.e. when $\hat{\rho}=|\Psi^-\rangle\langle\Psi^-|$ and $\boldsymbol{a}=\boldsymbol{b}$ the detectors always fired as $+-$ or $-+$, a hidden variable, λ, unknown to Alice and Bob used within the source may structure the photons to emerge with opposite polarizations. This hidden variable is determined the moment the photons are created and/or interacted and creates a local, real description for the anticorrelations experimentalists observe. Labeling the outcomes of Alice's and Bob's PBS as x and y (corresponding to $\pm$ detection events or ± 1) the local, realistic theory of quantum mechanics says the correlations of Alice and Bob are dictated by the conditional probability

$$P(\boldsymbol{a},\boldsymbol{b}|x,y)=P(\boldsymbol{a}|x,\lambda)P(\boldsymbol{b}|y,\lambda) \tag{1.73}$$

where for example $P(\boldsymbol{a}|x,\lambda)$ is the conditional probability of Alice observing event x with hidden variable λ given her PBS is oriented along $\boldsymbol{a}$. The locality is imposed by not allowing x of Alice's measurement base outcome to depend on $\boldsymbol{b}$ or $\boldsymbol{y}$ and shown within the separability of equation (1.73).

Any correlations between the measurements carried out by Alice and Bob will be revealed in the joint probabilities for their measurement outcomes. The probability that they measure the same polarizations ($++$ or $--$) minus the probability they measure different polarizations ($+-$ or $-+$) is expressed in the correlation coefficient C

$$C(\boldsymbol{a},\boldsymbol{b})=\int d\lambda\rho(\lambda)X(\boldsymbol{a},\lambda)Y(\boldsymbol{b},\lambda) \tag{1.74}$$

where $\rho(\lambda)$ is a classical probability distribution describing the set of hidden variables, and X and Y are the functions determining the measurement outcomes, ± 1, for Alice and Bob, that depend

on the measurement orientation and hidden variable λ.

Letting there be two other measurement directions $\boldsymbol{a}'$ and $\boldsymbol{b}'$ it can be shown that the quantity

$$S=C(\boldsymbol{a},\boldsymbol{b})+C(\boldsymbol{a},\boldsymbol{b}')+C(\boldsymbol{a}',\boldsymbol{b})-C(\boldsymbol{a}',\boldsymbol{b}') \tag{1.75}$$

$$=\int d\lambda\rho(\lambda)\Big(X(\boldsymbol{a},\lambda)Y(\boldsymbol{b},\lambda)+X(\boldsymbol{a},\lambda)Y(\boldsymbol{b}',\lambda)+X(\boldsymbol{a}',\lambda)Y(\boldsymbol{b},\lambda)-X(\boldsymbol{a}',\lambda)Y(\boldsymbol{b}',\lambda)\Big) \tag{1.76}$$

$$=\int d\lambda\rho(\lambda)X(\boldsymbol{a},\lambda)\Big(Y(\boldsymbol{b},\lambda)+Y(\boldsymbol{b}',\lambda)\Big)+X(\boldsymbol{a}',\lambda)\Big(Y(\boldsymbol{b},\lambda)-Y(\boldsymbol{b}',\lambda)\Big) \tag{1.77}$$

is bounded. To find the bound for this quantity, remember since X or Y must be $+1$ or -1 for a given value of λ and projection direction $\boldsymbol{a}$,$\boldsymbol{a}'$,$\boldsymbol{b}$ or $\boldsymbol{b}'$. With this the "Y" terms inside the ( ) of (1.77) can be either -2, 2, or 0. When one is ± 2 the other ( ) term must be 0. Since $\int d\lambda\rho=1$ and $|X|=1$, S must be bounded by the inequality

$$|S|\leq 2 \quad . \tag{1.78}$$

This is the CHSH inequality and S is termed the CHSH parameter after the inventors Clauser, Horne, Shimony, and Holt [51].

However, for quantum state $\hat{\rho}=|\Psi^-\rangle\langle\Psi^-|$ a given correlation term is

$$C(\boldsymbol{a},\boldsymbol{b})=\big\langle\Psi^-\big|\boldsymbol{a}\cdot\hat{\boldsymbol{\sigma}}\otimes\boldsymbol{b}\cdot\hat{\boldsymbol{\sigma}}\big|\Psi^-\big\rangle=-\boldsymbol{a}\cdot\boldsymbol{b} \tag{1.79}$$

and for $\boldsymbol{a}=(1,0,0)$, $\boldsymbol{a}'=(0,1,0)$, $\boldsymbol{b}=1/\sqrt{2}(1,1,0)$, $\boldsymbol{b}'=1/\sqrt{2}(1,-1,0)$ we get a CHSH parameter of

$$|S|=\left|-\frac{1}{\sqrt{2}}-\frac{1}{\sqrt{2}}-\frac{1}{\sqrt{2}}-\frac{1}{\sqrt{2}}\right|=2\sqrt{2} \quad .$$

This breaks the inequality of (1.78) showing that quantum mechanics allows special nonlocal

correlations that local real descriptions (which govern classical physics) cannot allow. Horedeki *et al* has shown that all violations of $|S|>2$ require quantum entanglement and therefore showing a violation of equation (1.78) is a tool in the quantum information toolbox to test for quantum entanglement [49, 52].

1.7 Quantum Fiber Networks

The goal of near-term quantum networks is to utilize the infrastructure of the current city-scale fiber optic networks of the communication grid. These quantum networks are going to consist of quantum sources, quantum channels, quantum memories, and quantum measurement systems [53–55]. An example of a star network, or nodes sharing a common quantum source is shown in figure 10. The channels transmit the quantum state to each user, and the quantum channels for city-scale networks are likely to be fiber optic channels. Because of transmission losses, the quantum channels can only be hundreds of kilometers before most of the quantum signals are lost to absorption. When $\hat{\rho}$ encodes the quantum information in the polarization degree of freedom, the polarization drift from the fiber may cause errors within the measurements between the users and source or relative measurements between the users themselves.

The work of this thesis examines the use of distributed measurements on polarization entangled photons for automated feedback to correct for polarization drift and estimate the amount of shared entanglement. Polarization drift is a problem for certain applications of quantum information protocols where the measurement base must be aligned with the source or the relative alignment of two or more measurement bases with each other. As we have seen, when the guiding medium, fiber, is exposed to time-dependent experimental conditions, whether it be mechanical vibrations, shifting stresses, or changing temperatures, it will cause local polarization transformations for the light propagating through it. When the quantum source is being transmitted to two or more

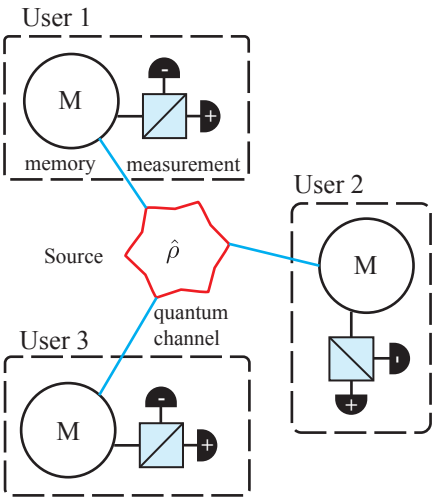

Figure 10: Schematic of a three-node star quantum network. Users share a quantum source producing state $\hat{\rho}$. The quantum channel carries either the whole state for single qubit sources or part of the state for entangled sources to each user or node. Each user can then store the quantum state in memory (M) and measure the state via projection measurements, shown as a PBS and photon detectors.

individuals the issue is compounded as the channels will drift independently with respect to one another.

It should be noted that polarization drift in fiber is only one of a few problems to overcome with distributed measurement bases sharing an entangled source. Another key problem is clock synchronization, or the syncing of when events coming from one quantum source happen at spatially separated nodes in the presence of local clock time drifts [31, 56–59]. No two clocks tick at the same rate so when separated clocks at each node in the quantum network drift apart from one another, errors will occur in photon arrival time measurements, which presents a challenge for reliably detecting coincidences. Methods can use Global Positioning System (GPS), White Rabbit protocols, or post-processing on the data stream. If methods require classical signal powers to propagate down the same quantum channel, interference, and detector blinding can occur.

This work is motivated by the application to solve problems relevant to the goal of creating a quantum network in the DC metropolitan area (DC-QNet), shown in figure 11. DC-QNet is

a consortium of U.S. government research laboratories in the Washington, D.C. area, including the U.S. Army Combat Capabilities Development Command Army Research Laboratory (ARL), the U.S. Naval Research Laboratory (NRL), the U.S. Naval Observatory (USNO), the National Institute of Standards and Technologies (NIST), the Laboratory for Telecommunication Sciences (LTS), and NASA. The aim of the consortium is to build a quantum network testbed at a regional level. While more work needs to be done before implementation within this larger scale network, the application of the ideas within this dissertation have been implemented within the local network between LTS and the University of Maryland College Park, shown in figure 11a. We found the ability to not only correct for the polarization drift within this 7.1 km of deployed fiber, but we were able to track faster, artificially created drifts. When this thesis project began, no other experiment had been performed examining the use of distributed measurements on entangled particles as a means for feedback to correct for polarization drift or to maximize violations to Bell's inequalities in deployed fiber. While conducting this research, two groups did manage to publish before our group, but in the case of polarization drift, did not systemically examine the ability to track polarization drift and in the Bell inequality violation study, did so using free space optics [43, 60].

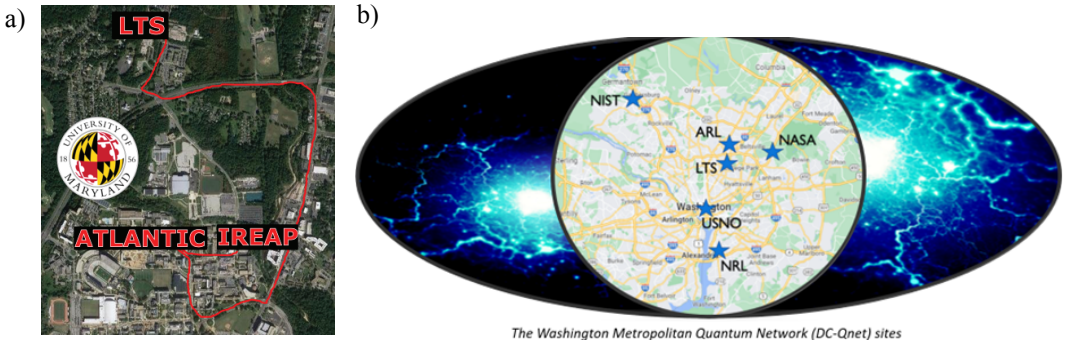

Figure 11: a) Fiber network between the University of Maryland's campus and the Laboratory for Telecommunication Sciences. b) Planned fiber quantum network within the DC Metropolitan area. Image credit to NIST's employees Abdella Battou and Thomas Gerrits https://www.nist.gov/news-events/news/2023/09/nists-quantum-experts-present-ways-improve-washington-dc-quantum-network.

Before concluding this introduction section, it is worth investigating one of the first applications of quantum networks and how polarization drift affects it. Quantum key distribution (QKD) is the distribution of shared private random keys between users using the rules of quantum mechanics to provide security. While QKD was not implemented in the experiments of this thesis, it is worth giving a high-level overview of two QKD protocols that use entangled photons to demonstrate the utility of QKD, quantum networks, and how QKD breaks down under the presence of polarization drift in single mode fibers. Additionally, the entanglement source and measurement setups of the experiments within this thesis are also required to conduct entanglement-based QKD.

QKD allows users to share private keys and detect the presence or absence of an eavesdropper because the eavesdropper must measure the quantum state, and this fundamentally changes the quantum state, seen in equations (1.46) and (1.55). The state they emit towards the intended user, based on their measurement results, will not share the same properties as the state they intercepted. When the two users compare their measured results, the two users will know if their private random key is secure or if an eavesdropper was observing. Once two individuals share a private random key, encrypted messages can be exchanged between them by using the random key as a one-time-pad over classical communication channels. Provided that the private random key is as long as the sent message, one-time-pad encryption is perfectly secure [61, 62].

1.7.1 Quantum Key Distribution using Entangled Photons

One-time-pad encryption relies on the users sharing an identical, private, random key or strings of 0s and 1s. The purpose of QKD, in general, is to provide a reliable method for transmitting a shared random key to each party, Alice and Bob. QKD began with the BB84 protocol proposed by Bennett and Brassard in 1984 [63] with Alice emitting single photons for Bob to measure. When two users share an entangled source, like figure 9, an extension of BB84

was developed by Bennett, Brassard, and Mermin in 1992, often called the BBM92 protocol [64]. It works in a similar fashion to BB84, only extended to two users sharing a two-particle quantum source. A year earlier Ekert developed a slightly different approach, E91 protocol [65], using the CHSH inequality of equation (1.78), to check for eavesdroppers. An overview of the most common QKD protocols is well described in the review by Gisin et al. [66].

The BBM92 protocol goes as follows: Alice and Bob share the maximally entangled singlet state, $\hat{\rho}=|\Psi^-\rangle\langle\Psi^-|$, and both measure either in the horizontal/vertical basis or diagonal/anti-diagonal basis. These are nonorthogonal, complementary bases where a perfectly polarized state in one basis gives a 50% detection to both detectors in the other basis. Regardless of the chosen measurement basis, if they measure a click on the positive detector, they record it as a "1," and if they measure a click on the negative detector, they record it as a "0". Because the $|\Psi^-\rangle$ is globally invariant to rotations, i.e

$$\hat{U}_a\otimes\hat{U}_b\big|\Psi^-\big\rangle=\hat{U}\otimes\hat{U}\big|\Psi^-\big\rangle=\big|\Psi^-\big\rangle \tag{1.80}$$

if they both chose to measure in the H/V basis or D/A basis their detectors will be anti-correlated ($+-$ or $-+$). Expressed differently, the state $|\Psi^-\rangle$ is the same in all measurement bases

$$\big|\Psi^-\big\rangle=\frac{1}{\sqrt{2}}\Big(|H\rangle_a|V\rangle_b-|V\rangle_a|H\rangle_b\Big)=\frac{1}{\sqrt{2}}\Big(|D\rangle_a|A\rangle_b-|A\rangle_a|D\rangle_b\Big) \quad . \tag{1.81}$$

They ignore times when one's detector clicks and the other does not (due to loss of photon in one channel) and when they choose opposite measurement bases (which happens 50% of the time). Because of the anti-correlations, Bob inverts his bit string so that $0\rightarrow1$ and $1\rightarrow0$ giving identical bit strings between Alice and Bob. A simplistic example of five pairs of entangled photons undergoing the BBM92 protocol is shown in table 3. If Alice and Bob chose to share a portion of their measured results, they can rule out the presence of an eavesdropper if the error

BBM92 Protocol										
	Alice	Bob	Alice	Bob	Alice	Bob	Alice	Bob	Alice	Bob
Basis	H/V	D/A	H/V	H/V	D/A	D/A	D/A	D/A	H/V	D/A
Outcome Bit	+ 1	+ 1	- 0	+ 1	+ 1	- 0	- 0	+ 1	+ 1	+ 1
Same Basis?	No		Yes		Yes		Yes		No	
Inversion			0	0	1	1	0	0		
Shared Key			0		1		0			

Table 3: Outline of BBM92 protocol.

rate is below 25%. This is because an eavesdropper can at most guess the correct orientation of the other's choice of measurement base 50% of the time and send a photon with the $+/-$ polarization state in that measurement base where again a 50% measurement error will occur with actual intended recipient, leaving a lower bound error rate of 25%. The security of this is based on the use of non-orthogonal measurement bases, a single entangled pair, and the no-cloning theorem [48, 67].

The E91 protocol begins with Alice and Bob randomly choosing to measure in one of three nonorthogonal bases:

$$\begin{aligned} \boldsymbol{a}_1&=(1,0,0) & \boldsymbol{b}_1&=\frac{1}{\sqrt{2}}(1,1,0) \\ \boldsymbol{a}_2&=\frac{1}{\sqrt{2}}(1,1,0) & \boldsymbol{b}_2&=(0,1,0) \\ \boldsymbol{a}_3&=(0,1,0) & \boldsymbol{b}_3&=\frac{1}{\sqrt{2}}(1,-1,0) \quad . \end{aligned} \tag{1.82}$$

After doing so they report which measurement base they measured in. In bases ($\boldsymbol{a}_3$, $\boldsymbol{b}_2$) and ($\boldsymbol{a}_2$, $\boldsymbol{b}_1$), the measurements are anti-correlated, and Bob's bits would be inverted. These three pairs of bases are chosen 2/9 of the time and will create random bit strings. However, the other

combinations ($\boldsymbol{a}_1$, $\boldsymbol{b}_1$), ($\boldsymbol{a}_1$, $\boldsymbol{b}_3$), ($\boldsymbol{a}_3$, $\boldsymbol{b}_1$), ($\boldsymbol{a}_3$, $\boldsymbol{b}_3$) can be used to calculate the CHSH parameter

$$\begin{aligned} S&=C(\boldsymbol{a}_1,\boldsymbol{b}_1)+C(\boldsymbol{a}_1,\boldsymbol{b}_3)+C(\boldsymbol{a}_3,\boldsymbol{b}_1)-C(\boldsymbol{a}_3,\boldsymbol{b}_3) \\ C(\boldsymbol{a},\boldsymbol{b})&=\frac{N_{++}(\boldsymbol{a},\boldsymbol{b})+N_{--}(\boldsymbol{a},\boldsymbol{b})-N_{+-}(\boldsymbol{a},\boldsymbol{b})-N_{-+}(\boldsymbol{a},\boldsymbol{b})}{N_{++}(\boldsymbol{a},\boldsymbol{b})+N_{--}(\boldsymbol{a},\boldsymbol{b})+N_{+-}(\boldsymbol{a},\boldsymbol{b})+N_{-+}(\boldsymbol{a},\boldsymbol{b})} \end{aligned} \tag{1.83}$$

where N_{+-} is the coincidence count rate from Alice's $+$ detector firing with Bob's $-$ detector firing. If $|S|>2$, then an eavesdropper could not have been present as their influence is identical to a classical hidden variable, which violates the CHSH inequality, and having a classical hidden variable is impossible, as shown in section 1.6 [66].

The provided QKD description is just a high-level overview of these methods as this thesis does not implement QKD. While the entangled photon source studied could be applied to conduct QKD, instead, this thesis seeked to tackle one of the hurdles QKD and other distributed polarization-resolved measurements have, the coordinated alignment of measurement frames in time-varying single mode fiber. This can be easily imagined when Alice and Bob measure in the same basis, but an uncontrolled polarization transformation has rotated Alice's measurement frame with respect to Bob's. This would cause Alice, for instance, to record a $+$ detection event when it should have been a $-$, or vice-versa, resulting in an error in Alice's and Bob's shared bit string. This error due to misaligned measurement frames is captured in equation (1.35). The bit error attributed to incorrect measurements on quantum systems is called the quantum bit error rate (QBER). QBER is defined as the ratio of the number of times the wrong detectors click together versus the number of total coincidence counts. If the two users, Alice and Bob, share an entangled source $\hat{\rho}=|\Psi^-\rangle\langle\Psi^-|$

and have two measurement bases that are supposed to be coaligned the total QBER is

$$\begin{aligned} \text{QBER} = \text{QBER}_{H/V} + \text{QBER}_{D/A} &= \left.\frac{N_{wrong}}{N_{tot}}\right|_{H/V} + \left.\frac{N_{wrong}}{N_{tot}}\right|_{D/A} \\ &= \sum_i \frac{1 - \boldsymbol{a}_i \cdot \boldsymbol{b}_i}{2} \end{aligned} \tag{1.84}$$

for $i = \{1,2\}$ corresponding to the H/V and D/A basis. The last term is the sum of the error probability of Alice's and Bob's two measurement base orientations. If the measurement bases drift with respect to each other the QBER will increase.

Chapter 2

Experimental Entanglement Generation and Control of the Measurement Frame Orientation

> "Basic research is like shooting an arrow in the air and, where it lands, painting a target."
>
> Homer Burton Adkins

This chapter aims to introduce the subtleties of how we perform polarization control, generate polarization entanglement, and measure polarization within the lab. In section 2.1 we preview the piezoelectric actuator based polarization controllers and present their pros and cons. In section 2.2 we discuss how we generate polarization entangled photons from the arrival of two cross polarized photons at a 50/50 beamsplitter. Finally, in section 2.3 I briefly outline how we measure a photon's polarization with polarization beamsplitters and superconducting nanowire single photon counting detectors (SNSPDs) and their pros and cons.

2.1 Fiber Squeezers as Polarization Controllers

> "Controller? I hardly know 'er."
>
> Adam Ehrenberg

In our lab, we primarily used voltage-controlled piezoelectric actuators as polarization controllers. These controllers clamp onto the fiber and apply a compressive force due to the expansion of the piezoelectric crystals when voltage is applied. The applied strain induced by the compressive force creates a fast and slow axis parallel and perpendicular to the applied force respectively. These controllers exhibit nearly 0 dB loss as the light stays within the guiding

medium. The speed at which voltage values can vary depends on the high-voltage drivers, but they often have millisecond response times. The drawback to using these controllers is that they often display hysteresis, where the strain induced by the controllers, and hence the effect on the polarization transform, is dependent on the prior path rather than purely the voltage applied [68]. As we will see this is one of the main limitations to using these controllers within calibrated alignment algorithms.

An experimental schematic of these controllers is seen in figure 12a. The phase retardance of the eigenmodes of each piezoelectric actuator is then a function of the applied voltage $\delta_i(V_i)$. Experimental data for the rotational axis of the second piezoelectric actuator can be seen in figure 12b for various different input polarizations dictated by different voltages across the first piezoelectric actuator. The rotation of a polarization state by a variable birefringent element is specified by equation (1.23), where a voltage causes a rotation about the actuator's birefringence vector.

For four piezoelectric actuators whose orientation around the circumference of the fiber's parameter, ϕ_{piezo} seen in Fig. 12a, are $0°$, $45°$, $0°$, and $45°$ the rotation axes ideally would be placed $90°$ apart from each other on the Poincaré sphere. Provided the birefringent axes are oriented as shown in Fig. 12a, only three actuators are needed in order to allow for an arbitrary, programmable mapping of any input polarization state to any desired output polarization state, see chapter 5.2.1.

However, when manufacturers package piezoelectric actuators, they are assembled under compression, to ensure that the actuators remain in contact with the fiber under all applied voltages [68, 69]. Therefore the zero voltage doesn't correspond to zero birefringence, as one might expect. This non-null birefringence, $\delta_i(V{=}0){=}\bar{\delta}_i$, changes the orientation of the rotation vectors mentioned above to some nonstandard orientation that needs to be calibrated for. Additionally,

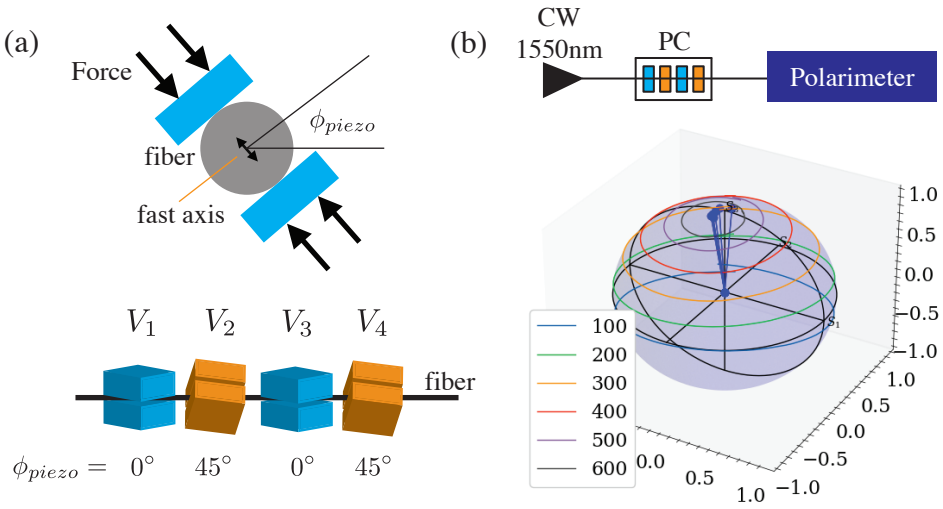

Figure 12: Polarization controller based upon voltage-controlled piezoelectric actuators at different orientations. a) Schematic of the polarization controller based on four piezoelectric actuators clamped on a fiber at relative orientations 0°,45°,0°,45° respectively. The amount of birefringence each actuator gives to the fiber is proportional to the force exerted by each piezoelectric actuator, which in turn is proportional to the voltage, V_i, across them. b) Experimental data of a continuous wave 1550nm laser coupled into fiber propagating through our polarization controller (PC) and the polarization state measured by a polarimeter. The rotational vector for the second piezoelectric actuator, $\hat{\boldsymbol{r}}_2$ seen as blue vectors, is found to be nearly $\hat{s}_3$. The 6 rotations around $\hat{\boldsymbol{r}}_2$ occur for different V_1 values changing the initial polarization state prior to the rotation about $\hat{\boldsymbol{r}}_2$.

when there is hysteresis, the orientation of each rotational vector with respect to each other varies over time. This is the main obstacle in using these types of controllers in simple calibrated polarization control strategies. Instead, we, as others often do, actuate these controllers using iterative algorithms that are agnostic to the physical mechanisms of actuation.

2.1.1 Rotation Vector Locations and Hysteresis

To explain the impact of non-zero stress at $V=0$ for each piezoelectric actuator, its impact on rotation vector locations, and how hysteresis further complicates the ability to provide accurate calibration, let us model our polarization controller as some rotational transform, **PC**, that changes the polarization state $\boldsymbol{S}_0$ to $\boldsymbol{S}_f$

$$\boldsymbol{S}_f = \mathbf{PC}(\delta_1,\delta_2,\delta_3,\delta_4)\boldsymbol{S}_0 \quad . \tag{2.1}$$

Initially, the true rotation vectors $\hat{\boldsymbol{n}}_i$, the birefringence's functional dependence $\delta_i(V)$, and the non-null birefringence $\bar{\delta}_i$ is unknown. The total polarization transformation from four piezoelectric actuators in series are

$$\mathbf{PC}(\delta_1,\delta_2,\delta_3,\delta_4) = \boldsymbol{R}_4(\hat{\boldsymbol{r}}_4,\delta_4+\bar{\delta}_4)\boldsymbol{R}_3(\hat{\boldsymbol{r}}_3,\delta_3+\bar{\delta}_3)\boldsymbol{R}_2(\hat{\boldsymbol{r}}_2,\delta_2+\bar{\delta}_2)\boldsymbol{R}_1(\hat{\boldsymbol{r}}_1,\delta_1+\bar{\delta}_1) \tag{2.2}$$

where $\boldsymbol{R}_i$ is described by (1.24). We can start decomposing (2.2) by noting $\boldsymbol{R}_i(\hat{\boldsymbol{r}},\delta_i+\bar{\delta}_i) = \boldsymbol{R}_i(\hat{\boldsymbol{r}},\delta_i)\boldsymbol{R}_i(\hat{\boldsymbol{r}},\bar{\delta}_i)$. Using this identity we can express (2.2) as

$$\begin{aligned}\mathbf{PC}(\delta_1,\delta_2,\delta_3,\delta_4) = {} & \boldsymbol{R}_4(\hat{\boldsymbol{r}}_4,\delta_4)\boldsymbol{R}_4(\hat{\boldsymbol{r}}_4,\bar{\delta}_4)\boldsymbol{R}_3(\hat{\boldsymbol{r}}_3,\delta_3)\boldsymbol{R}_3(\hat{\boldsymbol{r}}_3,\bar{\delta}_3) \\ & \boldsymbol{R}_2(\hat{\boldsymbol{r}}_2,\delta_2)\boldsymbol{R}_2(\hat{\boldsymbol{r}}_2,\bar{\delta}_2)\boldsymbol{R}_1(\hat{\boldsymbol{r}}_1,\delta_1)\boldsymbol{R}_1(\hat{\boldsymbol{r}}_1,\bar{\delta}_1) \quad .\end{aligned} \tag{2.3}$$

It will be shown that all $\bar{\delta}_i$ influence the preceding $\hat{\boldsymbol{n}}_j$ for $i>j$. To show this let us just look at the rotational transform $\boldsymbol{R}(\delta_1,\delta_2)=\boldsymbol{R}_2(\hat{\boldsymbol{r}}_2,\delta_2)\boldsymbol{R}_2(\hat{\boldsymbol{r}}_2,\bar{\delta}_2)\boldsymbol{R}_1(\hat{\boldsymbol{r}}_1,\delta_1)\boldsymbol{R}_1(\hat{\boldsymbol{r}}_1,\bar{\delta}_1)$. Using the relation $\boldsymbol{R}^{-1}\boldsymbol{R}=\boldsymbol{I}$ gives us the following expression

$$\boldsymbol{R}(\delta_1,\delta_2)=\boldsymbol{R}_2(\hat{\boldsymbol{r}}_2,\delta_2)\boldsymbol{R}_2(\hat{\boldsymbol{r}}_2,\bar{\delta}_2)\boldsymbol{R}_1(\hat{\boldsymbol{r}}_1,\delta_1)\boldsymbol{R}_1(\hat{\boldsymbol{r}}_1,\bar{\delta}_1) \tag{2.4}$$

$$=\boldsymbol{R}_2(\hat{\boldsymbol{r}}_2,\delta_2)\boldsymbol{R}_2(\hat{\boldsymbol{r}}_2,\bar{\delta}_2)\boldsymbol{R}_1(\hat{\boldsymbol{r}}_1,\delta_1)\Big(\boldsymbol{R}_2^{-1}(\hat{\boldsymbol{r}}_2,\bar{\delta}_2)\boldsymbol{R}_2(\hat{\boldsymbol{r}}_2,\bar{\delta}_2)\Big)\boldsymbol{R}_1(\hat{\boldsymbol{r}}_1,\bar{\delta}_1) \tag{2.5}$$

$$=\Big(\boldsymbol{R}_2(\hat{\boldsymbol{r}}_2,\delta_2)\Big)\Big(\boldsymbol{R}_2(\hat{\boldsymbol{r}}_2,\bar{\delta}_2)\boldsymbol{R}_1(\hat{\boldsymbol{r}}_1,\delta_1)\boldsymbol{R}_2^{-1}(\hat{\boldsymbol{r}}_2,\bar{\delta}_2)\Big)\boldsymbol{R}_2(\hat{\boldsymbol{r}}_2,\bar{\delta}_2)\boldsymbol{R}_1(\hat{\boldsymbol{r}}_1,\bar{\delta}_1) \tag{2.6}$$

$$=\boldsymbol{R}_2(\hat{\boldsymbol{n}}_2,\delta_2)\boldsymbol{R}_1(\hat{\boldsymbol{n}}_1,\delta_1)\boldsymbol{R}_2(\hat{\boldsymbol{r}}_2,\bar{\delta}_2)\boldsymbol{R}_1(\hat{\boldsymbol{r}}_1,\bar{\delta}_1) \quad . \tag{2.7}$$

The term in the brackets within the equation (2.6) is the true rotation caused by voltage changes in the first piezoelectric actuator with the impact of the null phase $\bar{\delta}_2$ of the second piezoelectric actuator, i.e.

$$\boldsymbol{R}_1(\hat{\boldsymbol{n}}_1,\delta_1)=\boldsymbol{R}_2(\hat{\boldsymbol{r}}_2,\bar{\delta}_2)\boldsymbol{R}_1(\hat{\boldsymbol{r}}_1,\delta_1)\boldsymbol{R}_2^{-1}(\hat{\boldsymbol{r}}_2,\bar{\delta}_2) \quad . \tag{2.8}$$

The first rotation in (2.6), $\boldsymbol{R}_2^{-1}(\hat{\boldsymbol{r}}_2,\bar{\delta}_2)$, only rotates the incoming polarization state, but changes to the polarization state after $\boldsymbol{R}_1(\hat{\boldsymbol{r}}_1,\delta_1)$ can be thought of as rotations to the rotational direction of the first piezoelectric actuator. This means the true rotational vector for the first piezoelectric actuator is affected by the non-zero birefringence of the second actuator

$$\hat{\boldsymbol{n}}_1=\boldsymbol{R}_2(\hat{\boldsymbol{r}}_2,\bar{\delta}_2)\hat{\boldsymbol{r}}_1 \quad . \tag{2.9}$$

This analysis can be applied to all actuators and the full polarization transformation can then be expressed as

$$\mathbf{PC}(\delta_1,\delta_2,\delta_3,\delta_4)=\boldsymbol{R}_4(\hat{\boldsymbol{n}}_4,\delta_4)\boldsymbol{R}_3(\hat{\boldsymbol{n}}_3,\delta_3)\boldsymbol{R}_2(\hat{\boldsymbol{n}}_2,\delta_2)\boldsymbol{R}_1(\hat{\boldsymbol{n}}_1,\delta_1)\boldsymbol{M} \tag{2.10}$$

where

$$\boldsymbol{R}_4(\hat{\boldsymbol{n}}_4,\delta_4)=\boldsymbol{R}_4(\hat{\boldsymbol{r}}_4,\delta_4)$$

$$\hat{\boldsymbol{n}}_4=\boldsymbol{r}_4$$

$$\boldsymbol{R}_3(\hat{\boldsymbol{n}}_3,\delta_3)=\boldsymbol{R}_4(\hat{\boldsymbol{r}}_4,\bar{\delta}_4)\boldsymbol{R}_3(\hat{\boldsymbol{r}}_3,\delta_3)\boldsymbol{R}_4^{-1}(\hat{\boldsymbol{r}}_4,\bar{\delta}_4)$$

$$\hat{\boldsymbol{n}}_3=\boldsymbol{R}_4(\hat{\boldsymbol{r}}_4,\bar{\delta}_4)\hat{\boldsymbol{r}}_3$$

$$\boldsymbol{R}_2(\hat{\boldsymbol{n}}_2,\delta_2)=\boldsymbol{R}_4(\hat{\boldsymbol{r}}_4,\bar{\delta}_4)\boldsymbol{R}_3(\hat{\boldsymbol{r}}_3,\bar{\delta}_3)\boldsymbol{R}_2(\hat{\boldsymbol{r}}_2,\delta_2)\boldsymbol{R}_3^{-1}(\hat{\boldsymbol{r}}_3,\bar{\delta}_3)\boldsymbol{R}_4^{-1}(\hat{\boldsymbol{r}}_4,\bar{\delta}_4)$$

$$\hat{\boldsymbol{n}}_2=\boldsymbol{R}_4(\hat{\boldsymbol{r}}_4,\bar{\delta}_4)\boldsymbol{R}_3(\hat{\boldsymbol{r}}_3,\bar{\delta}_3)\hat{\boldsymbol{r}}_2$$

$$\boldsymbol{R}_1(\hat{\boldsymbol{n}}_1,\delta_1)=\boldsymbol{R}_4(\hat{\boldsymbol{r}}_4,\bar{\delta}_4)\boldsymbol{R}_3(\hat{\boldsymbol{r}}_3,\bar{\delta}_3)\boldsymbol{R}_2(\hat{\boldsymbol{r}}_2,\bar{\delta}_2)\boldsymbol{R}_1(\hat{\boldsymbol{r}}_1,\delta_1)\boldsymbol{R}_2^{-1}(\hat{\boldsymbol{r}}_2,\bar{\delta}_2)\boldsymbol{R}_3^{-1}(\hat{\boldsymbol{r}}_3,\bar{\delta}_3)\boldsymbol{R}_4^{-1}(\hat{\boldsymbol{r}}_4,\bar{\delta}_4)$$

$$\hat{\boldsymbol{n}}_1=\boldsymbol{R}_4(\hat{\boldsymbol{r}}_4,\bar{\delta}_4)\boldsymbol{R}_3(\hat{\boldsymbol{r}}_3,\bar{\delta}_3)\boldsymbol{R}_2(\hat{\boldsymbol{r}}_2,\bar{\delta}_2)\hat{\boldsymbol{r}}_1$$

$$\boldsymbol{M}=\boldsymbol{R}_3(\hat{\boldsymbol{r}}_3,\bar{\delta}_3)\boldsymbol{R}_2(\hat{\boldsymbol{r}}_2,\bar{\delta}_2)\boldsymbol{R}_1(\hat{\boldsymbol{r}}_1,\bar{\delta}_1) \quad .$$

$\boldsymbol{M}$ works to change the initial polarization much like the birefringent section of fiber preceding the polarization controller, but has no impact on the direction of the rotational vectors as it precedes the transformation from the polarization controller. As we can see from above, all rotational vectors are affected by the non-zero birefringence values of all succeeding actuators.

If the $\bar{\delta}_i$ is constant, $\hat{\boldsymbol{n}}_i$ can be experimentally determined along with $\delta_i(V_i)$. One way to determine this is through scanning the voltage across each piezoelectric actuator

$$\begin{aligned}\hat{\boldsymbol{n}}_i=\frac{1}{2}\Big[&\Big(\max(\boldsymbol{S}_i(V)\cdot\hat{s}_1)+\min(\boldsymbol{S}_i(V)\cdot\hat{s}_1)\Big)\hat{s}_1+\Big(\max(\boldsymbol{S}_i(V)\cdot\hat{s}_2)+\min(\boldsymbol{S}_i(V)\cdot\hat{s}_2)\Big)\hat{s}_2\\&+\Big(\max(\boldsymbol{S}_i(V)\cdot\hat{s}_3)+\min(\boldsymbol{S}_i(V)\cdot\hat{s}_3)\Big)\hat{s}_3\Big] \quad .\end{aligned} \tag{2.11}$$

One can find $\delta_i(V_i)$ from

$$\phi_i(V)=\arctan_2\left(\frac{\Big(\boldsymbol{S}_0\times\boldsymbol{S}(V)\Big)\cdot\hat{\boldsymbol{n}}_i}{\boldsymbol{S}_0\cdot\boldsymbol{S}(V)}\right) \tag{2.12}$$

where $\boldsymbol{S}_0$ is the state of polarization when there is zero voltage on the i^{th} piezoelectric actuator.

However, the piezoelectric actuators experience hysteresis. This means if starting at a birefringence value of $\delta_i(V_0)=\delta_0$ for some voltage V_0 and after ramping up to a different voltage V_1 and after returning to V_0 the phase is no longer guaranteed to be δ_0. The birefringence depends not only on the voltage, but the path to get to the voltage. This can be accounted for by having a changing value for the null-phase $\bar{\delta}_i$. However, as we have seen, a changing null-phase for all actuators, except for the first, causes the rotational vectors $\hat{\boldsymbol{n}}_i$ to move around relative to one another making calibration more challenging. Examples of the rotational vectors of the first three piezoelectric actuators measured on a polarimeter from a 1550 nm classical laser are shown in figure 13a and their non-ideal configuration can be seen. If all $\bar{\delta}_i=0$ then $\hat{\boldsymbol{n}}_1=\hat{\boldsymbol{n}}_3$ and $\hat{\boldsymbol{n}}_1\cdot\hat{\boldsymbol{n}}_2=0$, however this is not the case. The measured angle between $\hat{\boldsymbol{n}}_1$ and $\hat{\boldsymbol{n}}_2$ is 115° instead of the 90°, which would be expected if the second actuator was oriented at 45°. Our lab has three piezoelectric actuator polarization controllers and all three show similar non-ideal rotational vector locations where $\hat{\boldsymbol{n}}_1\neq\hat{\boldsymbol{n}}_3$, $\hat{\boldsymbol{n}}_2\neq\hat{\boldsymbol{n}}_4$ or $\hat{\boldsymbol{n}}_1\cdot\hat{\boldsymbol{n}}_{2,4}\neq 0$. Additionally, the impact of the hysteresis from the piezoelectric actuator can be seen in figure 13b. The voltage across the second piezoelectric actuator jumped to a fraction of V_π and back to $V=0$, where V_π is the voltage needed to return to the same polarization state on the Poincaré sphere, 20 times before being measured and the error angle, equation (1.35), was recorded. The repeated large jumps lead to changing $\bar{\delta}_i$ values, shown via the increasing error. The larger the jump, the more likely it is that the hysteresis of the piezoelectric controller was going to impact the error.

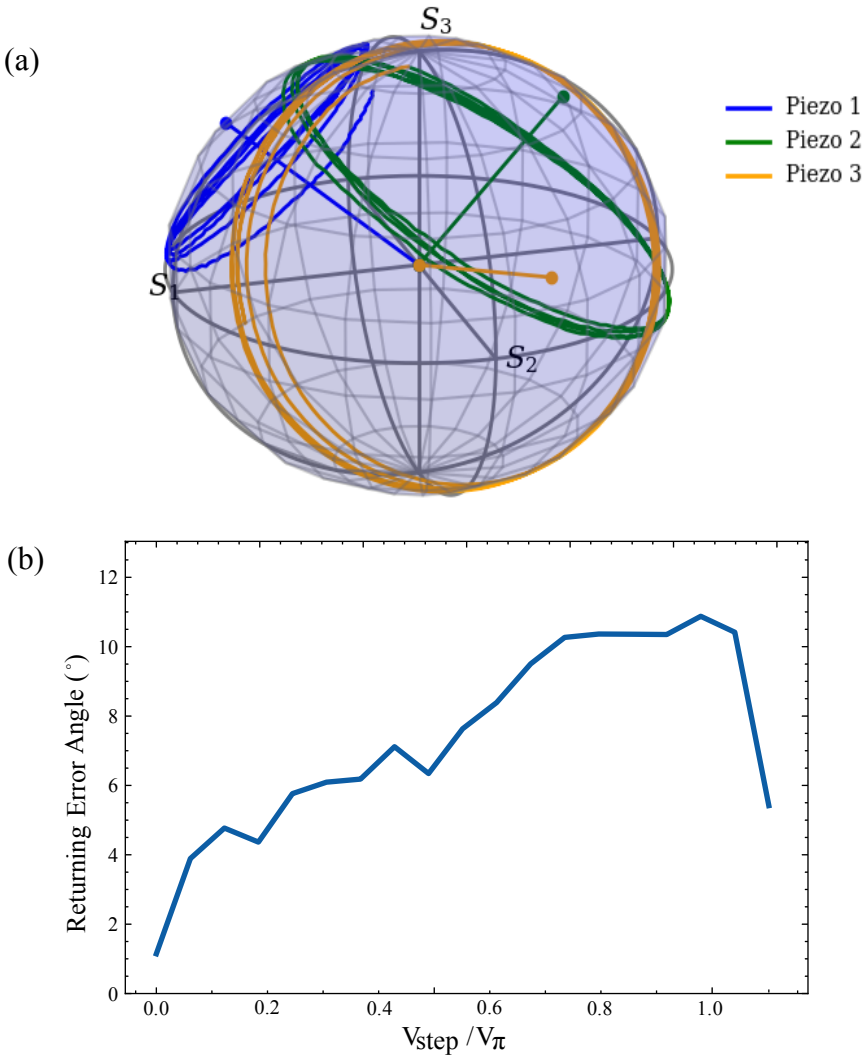

Figure 13: a)Rotational vector locations are shown as the vectors from the Poincaré sphere's center calculated from equation (2.11) and the rotational data that is also shown. The impact of the non-null birefringence at V_i=0 can be seen in the non-overlapping rotational vector locations of 1 and 3, as would be expected from the physical construction shown in figure 12. b) The impact of hysteresis is shown by recording the error from the polarization state before and after 20 voltage jumps of size V_{step}.

2.2 Polarization Entanglement Generation

The workhorse for entanglement generation for the past 30 years has been correlated and/or entangled photons produced from spontaneous parametric down conversion (SPDC) processes. Additional downstream linear optics make it possible to form maximally entangled Bell states in polarization [70–76]. SPDC is a second order nonlinear process through which an input wave at frequency ω_{pump} produces pairs of output photons at ω_s and ω_i where $\omega_s+\omega_i=\omega_{pump}$ by energy conservation. The subscripts s,i refer to the created photons typically called the signal and idler photons. If the signal and idler share the same polarization with each other and the destroyed pump photon it is called a type-0 SPDC process [77], if the signal and idler photon share the same polarization with each other, but are orthogonal to the destroyed pump photon it is a type-I SPDC process [78], and if the signal and idler photon are orthogonal to each other it is a type-II SPDC process [78]. More on second-order nonlinear optic effects and SPDC is provided in the appendix A.3.

The two main methods to generate a maximally entangled polarization Bell state is to split a correlated photon pair on a wavelength demultiplexer or on a 50/50 beam splitter [79–82]. This thesis uses the 50/50 beamsplitter method, which depends upon the arrival of the signal and idler photon in time and cross-polarized on the two input ports of a beam splitter. The two photons are initially split by a polarization beam splitter (PBS) and then recombined in time at the entangling 50/50 beamsplitter. From the PBS to the entangling beamsplitter, we will term it the entangling interferometer. It should also be noted that while this experiment has the SPDC process occur outside of the entangling interferometer, the SPDC process can occur inside in a Sagnac-like interferometer resulting in a more efficient production of the entangled state [83–87].

The simple, single-mode, quantum mechanical Hamiltonian for SPDC [83] is

$$\hat{H}_{SPDC}=\hbar\left(g\hat{a}_p^\dagger\hat{a}_s\hat{a}_i+g^*\hat{a}_p\hat{a}_s^\dagger\hat{a}_i^\dagger\right) \tag{2.13}$$

where the subscripts i,s,p correspond to the idler, signal, and pump photons, respectively, and g is the gain coefficient for the degenerate parametric amplifier that describes the SPDC process. The expression can be simplified by the strong coherent pump approximation $\hat{a}_p\rightarrow\alpha_p$, for complex coefficient α_p. This is valid because SPDC is an inefficient process where most pump photons do not undergo the SPDC process. The Hamiltonian is then

$$\hat{H}_{SPDC}=\hbar K\left(\hat{a}_s\hat{a}_i+\hat{a}_s^\dagger\hat{a}_i^\dagger\right) \tag{2.14}$$

where $K=g\alpha_p$. The unitary evolution operator for our state is then

$$\hat{U}_{SPDC}=e^{-\frac{i\hat{H}_{SPDC}t}{\hbar}}=e^{-iKt\left(\hat{a}_s\hat{a}_i+\hat{a}_s^\dagger\hat{a}_i^\dagger\right)} \tag{2.15}$$

where t is the interaction time within the nonlinear material. The wavefunction of the signal and idler photons can then be evaluated as

$$\begin{aligned}
|\Psi(t)\rangle_{si}&=\hat{U}_{SPDC}|0\rangle \\
&=e^{-iKt\left(\hat{a}_s\hat{a}_i+\hat{a}_s^\dagger\hat{a}_i^\dagger\right)}|0\rangle \\
&\approx\left(1-iKt\left(\hat{a}_s\hat{a}_i+\hat{a}_s^\dagger\hat{a}_i^\dagger\right)+(Kt)^2\left(\hat{a}_s\hat{a}_i+\hat{a}_s^\dagger\hat{a}_i^\dagger\right)^2+...\right)|0\rangle \\
&=|0\rangle+a_1|1\rangle_s|1\rangle_i+a_2|2\rangle_s|2\rangle_i+... \quad .
\end{aligned} \tag{2.16}$$

We can ignore the vacuum state as it will not lead to detection events, and since $Kt\ll1$, we can ignore the higher order multiple pair production events. The resulting output state is reduced to the

two photon state $|\Psi(t)\rangle_{si} \approx |1\rangle_s |1\rangle_i$. The true description of the downconversion process, taking into account the multiple pathways that could obey energy and momentum conservation within the entire nonlinear material, is best described in reference [75]. Assuming the nonlinear waveguide, of length L, is engineering to undergo type-II SPDC the signal and idler two-photon state is best represented by

$$|\Psi\rangle = \int d\omega_s d\omega_i f_0(\omega_s,\omega_i) \hat{a}_x^\dagger(\omega_s) \hat{a}_y^\dagger(\omega_i) |0\rangle \tag{2.17}$$

where $f_0(\omega_s,\omega_i)$ is the joint spectral amplitude for the signal and idler photons $\omega_{s,i}$ and x, y is the polarization state with x begin perpendicular to y. In general, the joint spectral amplitude is given by [88]

$$f_0(\omega_s,\omega_i) = N\alpha(\omega_s+\omega_i)\Phi(\omega_s,\omega_i) \tag{2.18}$$

where N is a normalization constant, $\alpha(\omega_s+\omega_i)$ is a function describing the pump field, and $\Phi(\omega_s,\omega_i)$ is a phase matching function to conserve momentum. The phase matching function is found to be a sinc profile [75]

$$\Phi(\omega_s,\omega_i) = \frac{\sin\Big(\Delta k(\omega_s,\omega_i)L/2\Big)}{\Delta k(\omega_s,\omega_i)L/2} \tag{2.19}$$

where $\Delta k = k_p(\omega_p) - k_s(\omega_s) + k_i(\omega_i) - \frac{2\pi}{\Lambda}$ is the quasi-phase matching bandwidth of the PPKTP waveguide, $k(\omega) = n(\omega)\omega/c$ is the wave number for the material, and Λ is the poling period length. For continuous wave pump sources, the pump field is $\alpha(\omega_s+\omega_i) = \sqrt{\delta(\omega_s+\omega_i-\omega_p)}$ where the delta function ensures energy conservation. The joint spectrum amplitude is then

$$f_0(\omega_s,\omega_i) \propto \text{sinc}\Big(\frac{\Delta k(\omega_s,\omega_i)L}{2}\Big)\sqrt{\delta(\omega_s+\omega_i-\omega_p)} \quad . \tag{2.20}$$

The type-II SPDC process using a periodically poled potassium titanyl phosphate (PPKTP) is

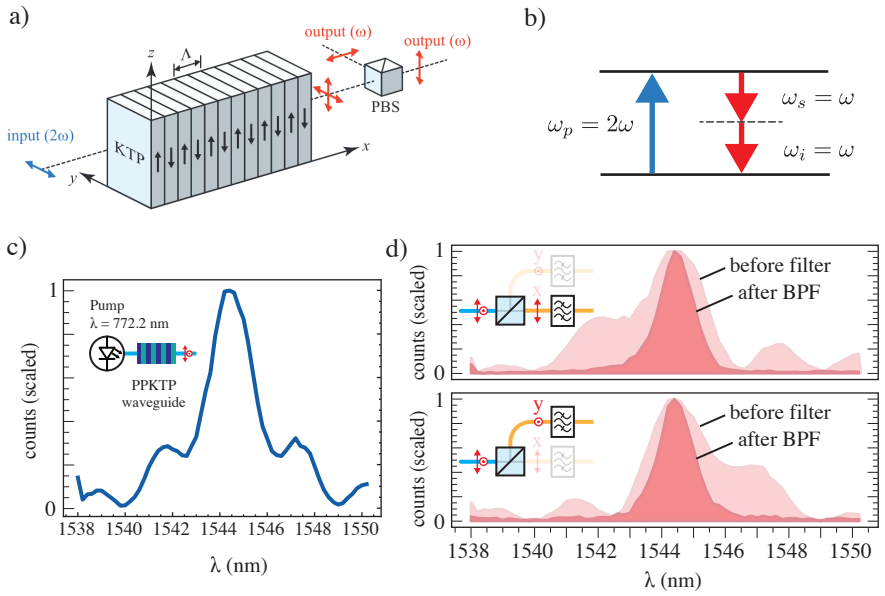

Figure 14: Type-II SPDC using PPKTP waveguide. a) Schematic of the periodic poling of KTP material with poling period Λ. b) Feynman diagram showing the consumption of a pump photon at ω_p=2ω and the production of two photons with the same energy, $\omega_{s,i}$=ω. c) The spectrum of the PPKTP down converted photons measured just after the PPKTP waveguide. d) The spectrum of the cross-polarized photons x,y is split by a PBS before and after a 1.4nm FWHM tunable bandpass filter.

shown in figure 14. The start of the entangling interferometer is the polarization beamsplitter that splits one photon, based on its polarization, to x path and the cross polarized photon to the y path. Both photons undergo filtering in their paths due to tunable bandpass filters. Each tunable filter can be assumed to be of Gaussian form with a center frequency $\Omega_{x,y}$ and bandwidth $\Delta\omega_{x,y}$

$$f_{\text{filter}}(\omega) \propto \exp\left\{\frac{-(\omega-\Omega)^2}{2\Delta\omega^2}\right\} \quad . \tag{2.21}$$

The filters used within our experiment have a full-width-half-max of 1.4 nm and are shown in figures 14d. If the filters are narrower than the central sinc width then the joint spectrum amplitude can be approximated as

$$f_0(\omega_s,\omega_i) \propto \exp\left\{\frac{-(\omega_s-\Omega_x)^2}{2\Delta\omega_x^2}\right\} \exp\left\{\frac{-(\omega_i-\Omega_y)^2}{2\Delta\omega_y^2}\right\} \sqrt{\delta(\omega_s+\omega_i-\omega_p)} \tag{2.22}$$

One of the two photons is relatively delayed by a controllable time delay stage (τ) before they arrive on the input ports of a 50/50 beamsplitter. This is shown in figure 15. Because the photons are in different polarization modes, their beamsplitter transformations are independent. The 50/50 beamsplitter transforms the creation operators

$$\begin{aligned}\hat{a}_x^\dagger(\omega_s) &\xrightarrow{\hat{U}_{BS}} \frac{1}{\sqrt{2}}\left(\hat{a}_x^\dagger(\omega_s)+i\hat{b}_x^\dagger(\omega_s)\right)\\ \hat{a}_y^\dagger(\omega_i) &\xrightarrow{\hat{U}_{BS}} \frac{1}{\sqrt{2}}\left(\hat{b}_y^\dagger(\omega_i)+i\hat{a}_y^\dagger(\omega_i)\right)\end{aligned} \tag{2.23}$$

where the output creation operators $\hat{a}^\dagger$ and $\hat{b}^\dagger$ correspond to photons in the spatial modes heading to Alice and Bob respectively. If the two photons arrive at the beamsplitter simultaneously the resultant state becomes

$$\begin{aligned}|\Psi\rangle \propto \hat{a}_x^\dagger(\omega_s)\hat{a}_y^\dagger(\omega_i)|0\rangle &\xrightarrow{\hat{U}_{BS}} \frac{1}{2}\left(\hat{a}_x^\dagger(\omega_s)+i\hat{b}_x^\dagger(\omega_s)\right)\left(\hat{b}_y^\dagger(\omega_i)+i\hat{a}_y^\dagger(\omega_i)\right)|0\rangle\\ &= \frac{1}{2}\Big[\left(\hat{a}_x^\dagger(\omega_s)\hat{b}_y^\dagger(\omega_i)-\hat{a}_y^\dagger(\omega_i)\hat{b}_x^\dagger(\omega_s)\right)\\ &\qquad +i\left(\hat{a}_x^\dagger(\omega_s)\hat{a}_y^\dagger(\omega_i)+\hat{b}_x^\dagger(\omega_s)\hat{b}_y^\dagger(\omega_i)\right)\Big]|0\rangle \quad .\end{aligned} \tag{2.24}$$

The first part $\left(\hat{a}_x^\dagger(\omega_s)\hat{b}_y^\dagger(\omega_i)-\hat{a}_y^\dagger(\omega_i)\hat{b}_x^\dagger(\omega_s)\right)$ is nothing more then the maximally entangled $|\Psi^-\rangle$ Bell state. The other term $\left(\hat{a}^\dagger(\omega_i)\hat{a}^\dagger(\omega_s)+\hat{b}^\dagger(\omega_i)\hat{b}^\dagger(\omega_s)\right)$ describes the case when two photons go to Alice or two photons go to Bob. Because our detection system only measures coincidences between Alice and Bob, these terms can be excluded by post-selection.

The general description of the emitted state depends on the relative temporal delay between the two photons at the entangling beamsplitter. Before the 50/50 beamsplitter, the overall two-photon state can be written as a superposition of the two photons arriving in time and out of time at the beamsplitter through a Gram-Schmidt process [48, 81]. This defines two temporal modes $|t_{in}\rangle$ and $|t_{out}\rangle$. Defining the time "in" as the arrival of the photon in the x path of the entangling

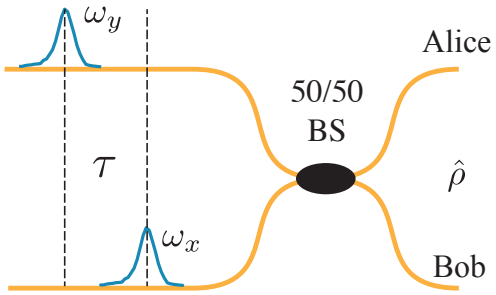

Figure 15: Entanglement interferometer schematic of two cross polarized photons ω_x,ω_y, arriving at a 50/50 beamsplitter. Alice and Bob share the joint state, $\hat{\rho}$, from the two exit ports.

interferometer at the entangling beamsplitter, the second photon's temporal state can be written as a superposition of the in and out of time temporal modes

$$|t_y\rangle = |t_{in}\rangle\langle t_{in}|t_y\rangle + |t_{out}\rangle\langle t_{out}|t_y\rangle \quad . \tag{2.25}$$

The inner products define the amount the two-photon wavepackets arrive in/out of time at the 50/50 beamsplitter. These terms are

$$\begin{aligned} k_{in} &= \langle t_{in}|t_y\rangle \\ k_{out} &= \langle t_{out}|t_y\rangle = \sqrt{1-|k_{in}|^2} \\ |t_{out}\rangle &= \frac{|t_y\rangle - k_{in}|t_{in}\rangle}{\sqrt{1-|k_{in}|^2}} \quad . \end{aligned} \tag{2.26}$$

If we assume the Gaussian profile of each photon heading towards the beamsplitter (due to equation (2.21)) has equal width, $\Delta\omega$, and central frequency, Ω, the temporal overlap can be written as a function of the temporal delay, τ, between each packet

$$\begin{aligned} |t\rangle &= \int d\omega \frac{1}{\pi^{1/4}\Delta\omega} e^{\frac{(\omega-\Omega_0)^2}{2\Delta\omega^2}} e^{i\omega t} \\ \langle t|t+\tau\rangle &= e^{i\tau\Omega} e^{-\frac{\Delta\omega^2\tau^2}{2}} \quad . \end{aligned} \tag{2.27}$$

When the photons do not arrive in time we would expect them to generate the classically mixed state $\hat{\rho}_{\text{class}}=\frac{1}{2}(|xy\rangle\langle xy|+|yx\rangle\langle yx|)$. The resulting state at the exit port of the 50/50 beamsplitter between Alice and Bob is the state

$$\hat{\rho}=k_e^2\left|\Psi^-\right\rangle\left\langle\Psi^-\right|+(1-k_e^2)\hat{\rho}_{class} \tag{2.28}$$

where $k_e^2=|\langle t|t+\tau\rangle|^2=e^{-\Delta\omega^2\tau^2}$ quantifies how much entanglement is present from the temporal overlap of the two photons. For large time delay, τ, we area able to generate the classically mixed state, $\hat{\rho}_{class}$, and for $\tau=0$ we are able to generate the maximally entangled Bell state $|\Psi^-\rangle\langle\Psi^-|=\frac{1}{2}(|xy\rangle\langle xy|+|yx\rangle\langle yx|-|xy\rangle\langle yx|-|yx\rangle\langle xy|)$. The 4x4 matrix representation of our state within the polarization x,y basis is

$$\hat{\rho}=\frac{1}{2}\begin{pmatrix} 0 & 0 & 0 & 0 \\ 0 & 1 & -e^{-\Delta\omega^2\tau^2} & 0 \\ 0 & -e^{-\Delta\omega^2\tau^2} & 1 & 0 \\ 0 & 0 & 0 & 0 \end{pmatrix} \tag{2.29}$$

where, for instance, the first row describes the coefficients $\langle xx|\hat{\rho}|xx\rangle$, $\langle xx|\hat{\rho}|xy\rangle$,$\langle xx|\hat{\rho}|yx\rangle$, and $\langle xx|\hat{\rho}|yy\rangle$. Looking at the concurrence entanglement quantifier, equation (1.70), we find the Hermitian matrix R, equation 1.69 is just $\hat{\rho}$, and the eigenvalues for $\hat{\rho}$ are $\lambda_1=\frac{1}{2}(1+k_e^2)$, $\lambda_2=\frac{1}{2}(1-k_e^2)$, and $\lambda_3=\lambda_4=0$. The concurrence is then just $\mathcal{C}=k_e^2$.

Quantum state tomography (QST) is the method of reconstructing the density matrix, $\hat{\rho}$, from the nine coordinated and alignment measurement bases shown in table 4 [89]. The methods of quantum state tomography use these various "cuts" across the many copies of the quantum state to reconstruct the entire density matrix. The quantum state tomography algorithm was done

Alice	Bob
H/V	H/V
H/V	D/A
H/V	R/L
D/A	H/V
D/A	D/A
D/A	R/L
R/L	H/V
R/L	D/A
R/L	R/L

Table 4: Nine coordinated measurements are needed for the reconstruction of $\hat{\rho}$ from the standard methods of quantum state tomography.

in software using the open-source quantum tomography library developed by Paul Kwiat's group [90] and the measurement results from the nine coordinated measurement bases. The alignment of each measurement base was done using a classical laser and polarimeter that generated a look-up table for the voltages on Alice's and Bob's polarization controller. The alignment signal was back-propagated through their polarization beam splitter and through their polarization controller and measured in one of the arms of the entangling interferometer. The results from the QST at τ=0 ps and at τ=5.25 ps are shown in figure 16. For τ=0 we generate close to the maximally entangled state $|\Psi^-\rangle$

$$\hat{\rho}_{\Psi^-} = |\Psi^-\rangle\langle\Psi^-| = \frac{1}{2}\begin{pmatrix} 0 & 0 & 0 & 0 \\ 0 & 1 & -1 & 0 \\ 0 & -1 & 1 & 0 \\ 0 & 0 & 0 & 0 \end{pmatrix} \tag{2.30}$$

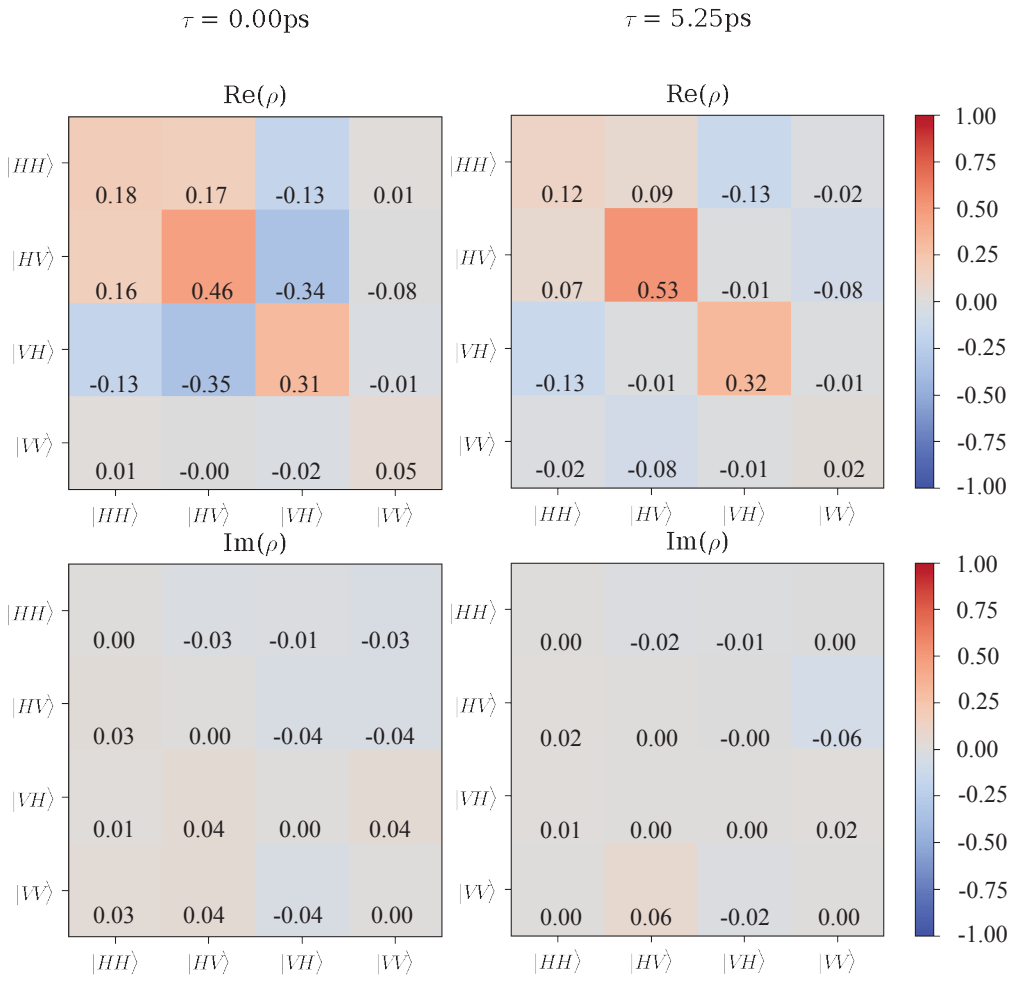

Figure 16: Reconstruction of our quantum source, $\hat{\rho}$, from the methods of quantum state tomography at two different temporal delays τ=0 ps and τ=5.25 ps.

and for large τ we see a state close to the classically mixed polarization state

$$\hat{\rho}_{\text{class}} = \frac{1}{2}\begin{pmatrix} 0 & 0 & 0 & 0 \\ 0 & 1 & 0 & 0 \\ 0 & 0 & 1 & 0 \\ 0 & 0 & 0 & 0 \end{pmatrix} . \tag{2.31}$$

An actual picture of our lab set up to generate entangled photons is shown in the labeled

figure 17.

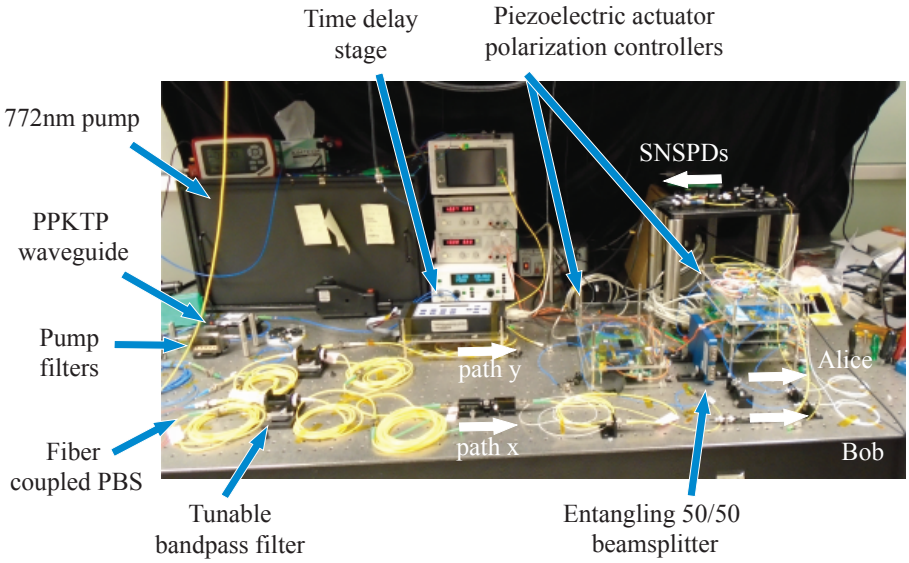

Figure 17: Picture of the entanglement generation experimental setup.

2.3 Polarization Measurement and Photon Detection

The polarization detection process of our experiment uses polarization beamsplitters (PBS), single photon detectors, and coincidence counting electronics. The PBSs are fiber-coupled in-line micro prisms, where the two orthogonal polarization modes are split into two different paths. If the polarization state heading into the PBS is described in terms of the H and V basis of the PBS as

$$|\psi\rangle = \cos\frac{\theta}{2}|H\rangle + \sin\frac{\theta}{2}e^{i\phi}|V\rangle \tag{2.32}$$

then the state is split into the H path with probability $\cos^2\frac{\theta}{2}$ and the V path with probability $\sin^2\frac{\theta}{2}$.

The photon is then detected by superconducting nanowire single-photon detectors (SNSPDs) where the nanowires are biased at the threshold of a superconducting state with no electrical resistance by cooling the nanowire down to $\sim$2 K, shown in figure 18. When a photon is absorbed by the nanowire the nanowire warms up and exits the superconducting state where a resistance

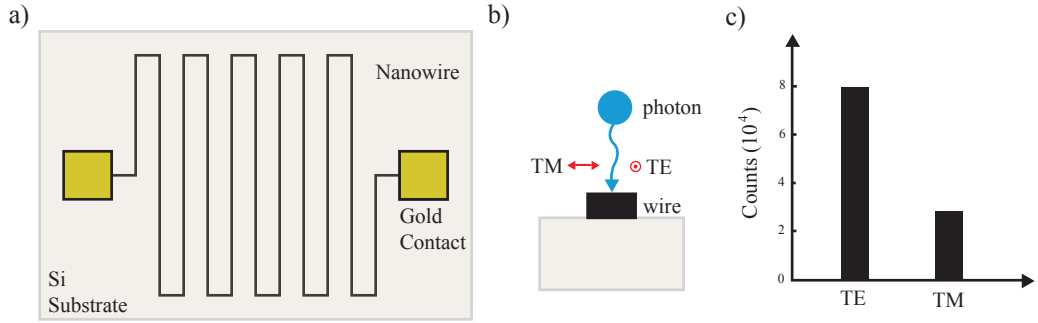

Figure 18: a) Top-down schematic of the superconducting nanowire single detector in a serpentine winding direction. This device is most sensitive to single photons polarized in the north and south direction, TE mode. b) Side schematic of one nanowire that is in and out of the plane, with the TE and TM electrical field modes. c) Measured count data from an attenuated CW laser at the TE and TM orientations.

to the current, and hence a voltage spike, can be recorded by voltage monitors. The quantum efficiency, defined as the ratio of detected versus total incident photons, is around 80% for the nanowire detectors used here. This is the maximum quantum efficiency attained for a specific polarization state. When the polarization is parallel to the winding of the nanowire, TE mode, the detection is highest, but when the polarization is orthogonal, TM mode, the detection is lowest. The impact of the polarization setting of the incident photon is shown in figure 18c. The count rate from an attenuated CW laser drops from 80,000 photons per second down to 29,000 photons per second. For photons polarized in the TM mode the quantum efficiency is reduced to roughly 30%.

The coincidence counting, or recording of two separate single photon detection events, is accomplished with the electronic timing equipment HydraHarp 400 produced by PicoQuant LLC, or the ID900 time correlator produced by IDQuantique LLC. These work by a simple start-stop time gating structure where an electrical impulse signal is fed to one starting port from the presence of one photodetection event of one SNSPD which starts a fast internal clock. That clock stops after another electrical impulse signal is recorded on the stopping port. Since the photons are always produced in pairs from the SPDC process, the distribution of interarrival times between the two

detectors should exhibit a distinct peak at a specific delay time that depends on the relative timing and cable/fiber lengths. The temporal width of this correlation signal depends on the timing jitter and temporal precision of the detection process. The timing jitter of the SNSPDs is on the order of 100 ps while the root-mean-square (rms) timing precision of the HydraHarp is <12 ps, and the timing precision of the ID900 in high-resolution mode is roughly <6 ps. We mainly use the ID900 in high-speed mode where bin widths are 100 ps, and timing jitter rms is 28 ps. While, functionally, the ID900 and Hydraharp both employ similar digital counting and time tagging methods, the ID900 allow for simultaneous coincidence counting between four different pairs of input channels, which allows any-to-any coincidence counting from all four ports (two at Alice and two at Bob) in that the start and stop channels can be dynamically assigned to any of four input ports allowing any-to-any coincidence counting from all four input ports.

Chapter 3

Polarization Alignment and Drift Compensation Using Entangled Photons

> "The difference between screwing around and science is writing it down.
>
> Adam Savage

This chapter describes the experimental investigation on aligning polarization measurement bases in deployed fiber using feedback measurements from entangled photons [1]. In section 3.1 we cover the prior literature for using quantum signals as feedback for polarization correction, in section 3.2 we describe the experiment, in section 3.3 we outline the theory using distributed measurements for measurement base alignment, in section 3.4 we discuss the experimental results, in section 3.5 we analyze the impact Poissonian statistics, accidental coincidence counts, and integration time have in alignment accuracy, and in 3.6 we study how this method works on deployed fiber and in an artificially drifting scenario. Additional work has been done beyond the scope published in Dowling *et al* [1] for full measurement frame alignment and is shown in section 3.8.

3.1 Introduction

A significant obstacle to entanglement distribution through fiber is that the majority of deployed fiber communication channels do not preserve the state of polarization of the optical signal. Even if the input polarization state is known, the state that emerges from a span of single-mode fiber is indeterminate and varies in time because of unpredictable and uncontrolled variations in temperature, bending, and stress [10, 15, 16, 18, 91]. Observation of polarization

entanglement relies upon alignment and calibration of the measurement bases between the two separate observers, which is hindered by these uncontrolled variations.

The problem of polarization alignment and stabilization is well-studied in classical fiber transmission systems [26, 27, 36, 37, 92, 93], but existing methods cannot be directly applied when the measured signals are at the single-photon level. Moreover, if the photons are polarization-entangled, the received photons in each fiber are statistically unpolarized, and polarization control cannot be achieved from local measurements alone.

One solution to this problem is to interleave well-polarized alignment signals, either in time or wavelength, that co-propagate with the quantum signal in the same fiber [21, 34, 35, 44]. However, time multiplexing can limit the overhead of the transmitted quantum signal because of leakage of the pilot tone into the quantum signal when repetition rates are too high. Wavelength multiplexing similarly places stringent constraints on optical filtering and is ultimately limited by polarization mode dispersion between the signal and pilot wavelengths [30]. Both methods add experimental complexity as they require pilot tone sources, multiplexers, and detectors for integration, separation, and measurement of these classical signals along with the quantum sources and detectors.

In QKD systems that employ the BB84 protocol, the transmitted photons are polarized along a prescribed, but randomly chosen direction, but are not entangled. In this case, the polarization axes of the receiver can be aligned locally by using only the sifted keys or basis reconciliation process, which requires only single-photon measurements [31, 41]. More recently, Shi *et al.* achieved polarization alignment in an entanglement-based QKD system, by using a stochastic optimization algorithm to minimize the quantum bit error rate between non-local receivers [43]. They report compensation in under 20 minutes, which is sufficient for tracking slower polarization drifts in shorter spans of underground deployed fiber. In addition, an alternative polarization

alignment strategy using Bayesian estimation was shown to work in low coincidence count and high shot noise regimes [94].

Here, we describe an experimental method for both polarization alignment and tracking that uses a simplex optimization algorithm based on non-local coincidence measurements to acquire and stabilize the observation of polarization-entangled photons. The method requires no temporal or spectral interleaving of classically polarized signals, and we confirm that when measured locally, the received photons carry no signature of the polarization state. Experimental results show that the method achieves alignment within approximately 160 seconds, to target states positioned arbitrarily on the Poincaré sphere. The system is shown to dynamically adapt to systematic variations in the opposite (uncontrolled) fiber channel. We finally demonstrate the successful operation of the system over a 7.1 km deployed fiber link.

3.2 Experiment

Fig. 19 shows the experimental apparatus used to demonstrate non-local polarization alignment and control. Polarization-entangled photons are generated using type-II spontaneous parametric downconversion (SPDC) in a periodically-poled potassium titanyl phosphate (PPKTP) waveguide (AdvR, Inc.). The PPKTP waveguide is pumped with a 772.2 nm, continuous-wave external cavity diode laser (Newport TLB-7100), and generates $\sim 1 \times 10^6$ pairs of orthogonally-polarized, wavelength degenerate photons per second [75, 76]. An anti-reflection coated silicon wafer and 1550 nm long pass filter are used to extinguish any residual pump light and other noise. Because of the birefringence of both the PPKTP waveguide and the polarization-maintaining (PM) output fiber, the downconverted photons acquire a differential group delay, making them distinguishable through their relative time of arrival [79]. The downconverted photons are separated in a polarizing beamsplitter, with a controllable time delay stage in one arm to equalize the timing.

Fig. 20a shows the spectra of the spontaneously-generated x- and y-polarized photons, measured after the polarization beamsplitter. A pair of matching 1.4 nm tunable bandpass filters (OZ Optics) was used to extinguish the distinguishable spectral tails caused by asymmetry in the phase-matching conditions. The time delay (τ) was adjusted by co-polarizing and combining the channels and recording the Hong–Ou–Mandel (HOM) interference, which shows 93% extinction in the coincidence rate, confirming the indistinguishability of the photons, as shown in Fig. 20(b). The quality of entanglement in terms of the CHSH parameter can be estimated from the HOM interference visibility or extinction [95].

To generate entangled photons, the polarization controllers in the arms of the source interferometer are then adjusted so that the two photons arrive at the (non-polarizing) 50/50 beam splitter with orthogonal polarizations. A variable attenuator is used to equalize the powers in the two polarization states, in order to eliminate any partial polarization component for the transmitted photons. After the beam splitter, the entangled photons are then transmitted, optionally through a fiber span, to the receivers.

The two spatially separated receivers (here denoted Alice and Bob) each include a piezoelectric fiber-based polarization controller (General Photonics PolaRITE III), polarization beamsplitter, and a pair of superconducting nanowire photon-counting detectors with quantum efficiencies of 80% [Opus One, Quantum Opus LLC.]. Because the nanowire detectors have a polarization-dependent efficiency, an additional manual polarization controller (not shown) is inserted between the polarizing beamsplitter output and the photon counter to maximize the quantum efficiency. The electronic signals are time-tagged, and correlation measurements are processed in real-time by a time-correlating single-photon counting (TCSPC) instrument with timing resolution up to 1 ps, which enables measurement of the pairwise coincidence rate between spatially separate detectors. Due to detector and electronic jitter a coincidence window of 100 ps is used for signal

detection. By using a small coincidence window, we improve the signal-to-noise ratio by ignoring the unpaired detection events that do not temporally coincide with our downconverted photons. A computer records the coincidence rate in real-time and uses the resulting measurement to control one or both of the piezoelectric polarization controllers.

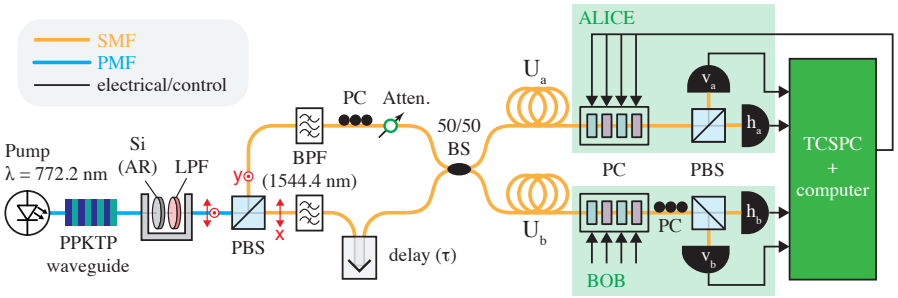

Figure 19: Diagram of the experimental setup used to demonstrate non-local polarization control. Entangled photons are generated through spontaneous parametric downconversion in a periodically poled potassium titanyl phosphate (PPKTP) waveguide, followed by longpass and bandpass filters (LPF, BPF) to extinguish the pump signal and ensure spectral indistinguishability (Fig. 20). The photons are transmitted to spatially separated receivers (Alice and Bob), which each record the photons after polarizing beamsplitters (PBS). Piezoelectric polarization controllers (PC) adjust the polarization state in each channel. A time-correlating single-photon counting (TCSPC) instrument records the coincidence rate.

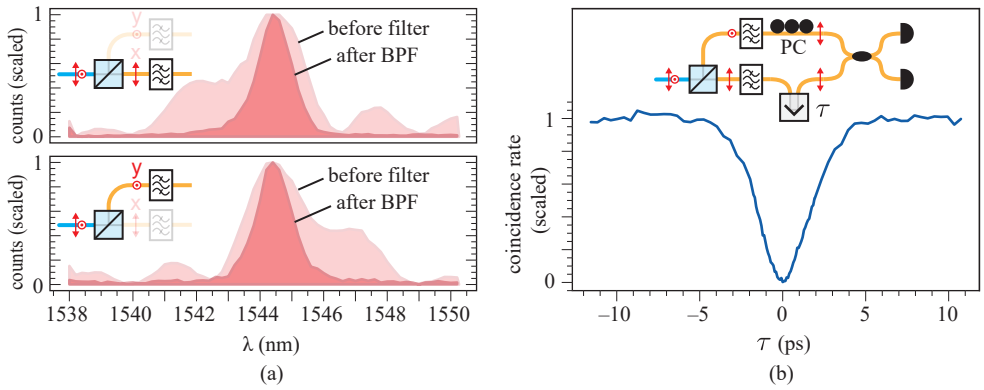

Figure 20: a) Spontaneous parametric downconversion spectrum from PPKTP waveguide before and after the bandpass filters (BPF), showing down converted signal (H polarized) and idler (V polarized) photons. b) Measured Hong-Ou-Mandel interference, demonstrating indistinguishability when the two combined, filtered photons are co-polarized and coincident.

3.3 Theory

As shown in chapter 2 equation (2.28) when $\tau=0$ the output entangled photon pair state emerging from the beam splitter can be expressed as:

$$|\Psi_{\text{out}}\rangle=\frac{1}{2}(|x_a\rangle|y_b\rangle-|y_a\rangle|x_b\rangle+|x_a\rangle|y_a\rangle+|x_b\rangle|y_b\rangle) \tag{3.1}$$

where, for example, the leading term $|x_a\rangle|y_b\rangle$ describes an x-polarized photon transmitted to Alice's port and a y-polarized photon transmitted to Bob's port. The first two terms in (3.1) represent the case when pairwise orthogonally polarized photons are transmitted to Alice and Bob, respectively, while the final terms represent the possibility that both photons go to either Alice or Bob. Because our experimental measurements are conditioned on coincidences between Alice and Bob, these final terms are excluded through post-selection[79, 83, 96]. The post-selected state then simplifies to the $|\Psi^-\rangle$ Bell state,

$$\left|\Psi^-\right\rangle=\frac{1}{\sqrt{2}}(|x_a\rangle|y_b\rangle-|y_a\rangle|x_b\rangle) \tag{3.2}$$

The fiber connecting to Alice transforms the polarization state of the optical signal so that an initially x-polarized state will, in general, emerge from the fiber as elliptically polarized, and conversely, an emerging linear polarization state would correspond to an elliptically polarized launch state. This transformation between the input and output states can be described by a complex unitary matrix (Jones matrix) $\boldsymbol{U}_a$ and its inverse:

$$\begin{bmatrix} h_a \\ v_a \end{bmatrix}=\boldsymbol{U}_a\begin{bmatrix} x_a \\ y_1 \end{bmatrix}, \qquad \begin{bmatrix} x_a \\ y_a \end{bmatrix}=\boldsymbol{U}_a^{\dagger}\begin{bmatrix} h_a \\ v_a \end{bmatrix} \tag{3.3}$$

where $|h_a\rangle$=(1,0) and $|v_a\rangle$=(0,1) denote the two output states that get separated and detected by the polarizing beamsplitter and photon detectors. The matrix $\boldsymbol{U}_a^\dagger$ describes how these output states are mapped back into an equivalent elliptical polarization basis at Alice's fiber input. A general form for a unitary matrix (ignoring the common phase associated with transmission) is:

$$\boldsymbol{U}_a^\dagger = \begin{bmatrix} a_x & -a_y^* \\ a_y & a_x^* \end{bmatrix} \tag{3.4}$$

where the first column of $\boldsymbol{U}_a^\dagger$ is a complex unit vector (Jones vector),

$$\tilde{\boldsymbol{a}} \equiv \begin{bmatrix} a_x \\ a_y \end{bmatrix}, \qquad |a_x|^2+|a_y|^2=1 \quad . \tag{3.5}$$

The vector $\tilde{\boldsymbol{a}}$ defines the input polarization state that would be fully transmitted into the "h" output of Alice's polarization beamsplitter. A polarizing beamsplitter that is preceded by a unitary transformation is thus equivalent to an elliptical polarization beamsplitter, that splits the incident light along an axis defined by the Jones vector $\tilde{\boldsymbol{a}}$.

Just like it was shown in section 1.1.1 the complex, two-dimensional Jones vector $\tilde{\boldsymbol{a}}$ can be translated into a real, three-dimensional Stokes vector $\boldsymbol{a}$, using equation (1.15) and Pauli matrices (1.17)

$$\boldsymbol{a} = \begin{bmatrix} S_{a_1} \\ S_{a_2} \\ S_{a_3} \end{bmatrix} = \begin{pmatrix} \langle\tilde{\boldsymbol{a}}|\hat{\sigma}_1|\tilde{\boldsymbol{a}}\rangle \\ \langle\tilde{\boldsymbol{a}}|\hat{\sigma}_2|\tilde{\boldsymbol{a}}\rangle \\ \langle\tilde{\boldsymbol{a}}|\hat{\sigma}_3|\tilde{\boldsymbol{a}}\rangle \end{pmatrix} = \begin{bmatrix} |a_x|^2-|a_y|^2 \\ a_x a_y^*+a_x^* a_y \\ i(a_x a_y^*-a_x^* a_y) \end{bmatrix}, \quad S_{a_1}^2+S_{a_2}^2+S_{a_3}^2=1 \tag{3.6}$$

that is easily visualized as a vector on the Poincaré sphere. $\boldsymbol{a}$, and its temporal variations can also be measured experimentally by transmitting a classical linearly polarized signal through the fiber and recording the output state on a polarimeter. Bob's channel undergoes a similar, but

different polarization transformation, described by analogous Jones and Stokes vectors $\tilde{\boldsymbol{b}}$ and $\boldsymbol{b}$ that characterize the polarization rotation occurring in Bob's fiber.

With these definitions, the probability that Alice and Bob both detect horizontally polarized photons can then be calculated as

$$P(h_a,h_b)=\left|\langle h_a|\langle h_b|\Psi^-\rangle\right|^2 \tag{3.7}$$

where we use (3.3)-(3.4) to express

$$|h_a\rangle=a_x^*|x_a\rangle+a_y^*|y_a\rangle, \quad |h_b\rangle=b_x^*|x_b\rangle+b_y^*|y_b\rangle$$

Upon substitution into (3.7), this yields, after algebraic simplification,

$$P(h_a,h_b)=\frac{1}{2}|a_xb_y-a_yb_x|^2=\frac{1}{2}\left(1-\left|\tilde{\boldsymbol{a}}^*\cdot\tilde{\boldsymbol{b}}\right|^2\right) \tag{3.8}$$

The inner product of two Jones vectors $\tilde{\boldsymbol{a}}^*\cdot\tilde{\boldsymbol{b}}$ can be related to the inner product of their corresponding Stokes vectors[97],

$$\left|\tilde{\boldsymbol{a}}^*\cdot\tilde{\boldsymbol{b}}\right|^2=\frac{1}{2}(1+\boldsymbol{a}\cdot\boldsymbol{b}) \tag{3.9}$$

which gives a simple expression for the coincidence probability

$$P(h_a,h_b)=\frac{1}{4}(1-\boldsymbol{a}\cdot\boldsymbol{b})=\frac{1}{4}(1-\cos\theta_{ab}) \tag{3.10}$$

where θ_{ab} represents the angular separation between polarization bases $\boldsymbol{a}$ and $\boldsymbol{b}$ on the Poincaré sphere, as shown in Fig. 21. The coincidence rate between horizontal and vertical channels, is,

analogously, found to be:

$$P(h_a,v_b)=\frac{1}{4}(1+\boldsymbol{a}\cdot\boldsymbol{b})=\frac{1}{4}(1+\cos\theta_{ab}) \tag{3.11}$$

These simple relationships are a generalization of the well-known result that for linearly polarized measurements of entangled photons, the coincidence rate depends only on the relative difference between their polarization axes. When $\boldsymbol{a}$ and $\boldsymbol{b}$ are matched, the coincidence rate is zero, as expected. When $\boldsymbol{a}$ and $\boldsymbol{b}$ are anti-aligned on the Poincaré sphere (which corresponds to orthogonal bases), the coincidence rate is 1/2, because the photons may emerge from the other pair of orthogonal output channels with equal probability. When $\boldsymbol{a}=\boldsymbol{b}$, then the total polarization transformation due to the fiber and polarization controller of Alice's and Bob's channel are equal for that polarization projection direction, and the two have an aligned measurement base.

An important consequence of equation (3.10) is that while non-local measurements are required to measure the coincidence rate, the adjustment needed to minimize the coincidence rate only needs to be performed at one location, i.e., Alice may adjust $\boldsymbol{a}$ to any target state $\boldsymbol{b}$ in order to minimize (3.10).

The polarization adjustment is achieved using piezoelectric fiber polarization actuators [92], which offer electric polarization control with negligible fiber insertion loss, an important advantage over liquid crystal actuators, electrooptic actuators, or rotating waveplates. The piezoelectric actuators provide four successive squeezing elements that produce a strain-induced fiber birefringence oriented at $0°$, $45°$, $0°$, and $45°$, shown in section 2.1. Each actuator produces a retardance in proportion to the applied voltage, which can be visualized on the Poincare sphere as an adjustable rotation about the axes S_1 or S_2 (in the reference frame of the piezoelectric actuator.)

In principle, if Alice's PBS is adjusted to be $45°$ relative to the axis of the final piezoelectric

actuator (i.e. if the PBS is oriented along S_1), then it would be possible to achieve complete alignment of $\boldsymbol{a}$ to $\boldsymbol{b}$ by using only the two piezoelectric stages of the actuator [36]. In practice, however, this condition is difficult to achieve. Therefore, we use three piezoelectric stages, which ensure full coverage of the Poincaré sphere regardless of how the PBS is aligned. The fourth actuator could be employed to achieve reset-free actuation[27], but was not used here.

We chose to employ the Nelder-Mead simplex algorithm [98] to minimize the measured rate of coincidence detection, by adjusting the piezoelectric polarization controller at Alice. The algorithm creates a four-vertex tetrahedral simplex in the 3D space defined by the voltages on three actuators. The Nelder-Mead method is agnostic to the actuation mechanism and does not rely on a mathematically-predictive model to determine the actuation voltages. Because it iteratively refines the actuator voltages in order to minimize the coincidence rate, it can be executed continuously in order to track sufficiently slow changes in the minimization condition. The Nelder-Mead algorithm is implemented through python's scipy library [99].

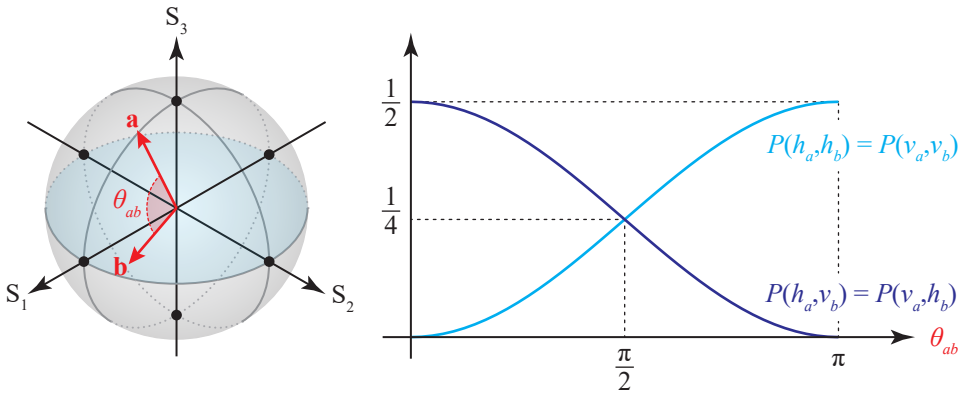

Figure 21: Alice's and Bob's horizontal measurement Stokes vectors, $\boldsymbol{a}$ and $\boldsymbol{b}$ on the Poincaré sphere. The joint probability of detection from the shared entangled state (3.2) is expressed in equation (3.10) as a function of the interior angle θ_{ab}.

3.4 Polarization Alignment

An example of the convergence between Alice's and Bob's horizontal measurement bases can be seen in Fig. 22. Alice's three voltages, Fig. 22a, change as they iterate through the Nelder-Mead algorithm minimizing the coincidence rate between Alice's and Bob's horizontal detectors, cyan line in Fig. 22b. The initial simplex begins around half the half-wave voltage for each piezoelectric actuator, denoted V_π. After thirty measurements, the extinction ratio between the coincidences of the two detectors being minimized (h_a,h_b) and the coincidences of the detectors being maximized (h_a,v_b) raises above 90%. It is important to note that Bob's and Alice's count rates, Fig. 22c, remain constant even though Alice's polarization controller is changing. This observation confirms that the alignment is reliant on the non-local entangled measurement, and that the local single photon signals do not carry any polarization signature.

To assess the robustness of our alignment algorithm, we used a second piezoelectric actuator in Bob's channel to manually set the target basis ($\boldsymbol{b}$), and then allowed the alignment algorithm to automatically adjust Alice's basis ($\boldsymbol{a}$) to match. Bob's measurement basis was pre-established by back-propagating a classical 1550 nm CW laser through one of the PBS exit ports and recording the resulting polarization state on a polarimeter inserted at the 50/50 beamsplitter. Bob's piezoelectric voltages were then manually adjusted (and recorded) in order to map his polarization basis to the six nodes of the Poincaré sphere, $\pm S_1$,$\pm S_2$,$\pm S_3$, as shown in the insets of Fig. 23. After re-connecting the entangled photon source and photon counters, we cycled through these six pre-configured target states, each time starting Alice at the same initial condition of $\boldsymbol{V}_{\text{Alice}}=$ $[V_\pi/2,V_\pi/2,V_\pi/2]$.

The cyan traces in Fig. 23 plot the measured coincidence rate between Alice's h_a photon and Bob's h_b photon, showing successful convergence with an extinction ratio of 95% within 160

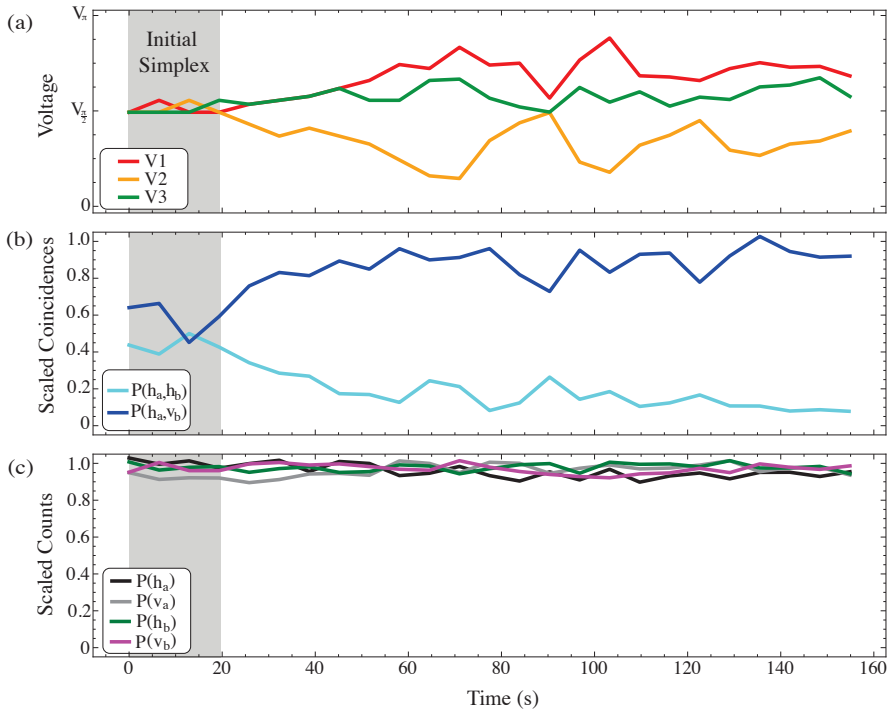

Figure 22: Representative example showing the adaptive alignment of Alice's measurement basis to minimize the observed coincidence rate. (a) The three voltages applied to Alice's piezoelectric polarization controller, which change as they iterate through the Nelder-Mead algorithm. (b) The Nelder-Mead algorithm finds the minimum of the measured h_a and h_b photon coincidence rate, seen in cyan. Conversely, the joint photodetection between the h_a and v_b photons rises to a maximum, seen in blue. (c) The single photon count rates remain unchanged for both Bob and Alice throughout the alignment process, indicating no polarization dependence within those signals.

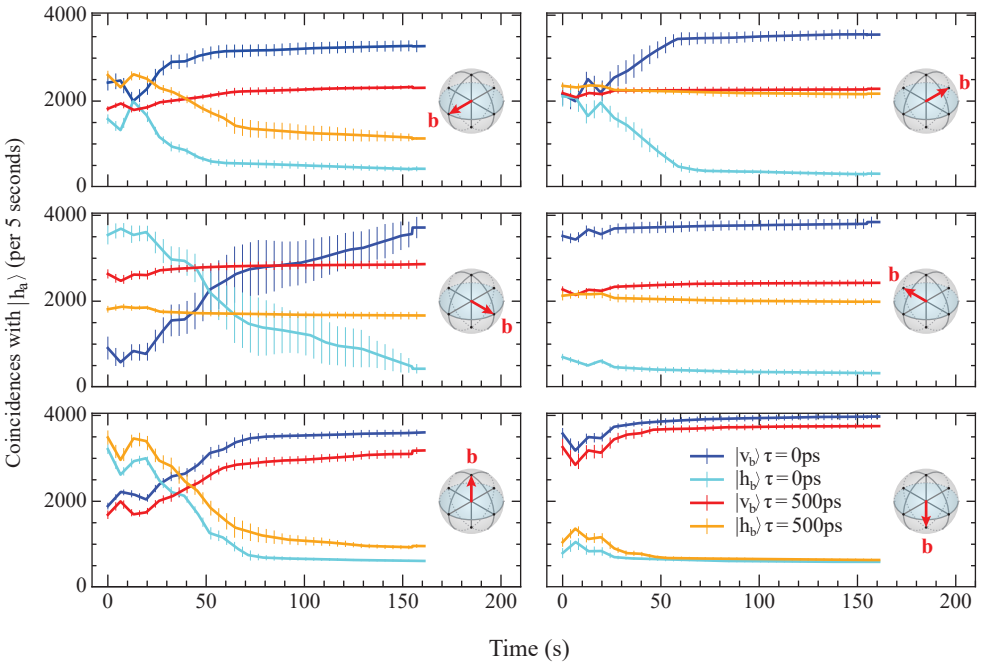

Figure 23: Automatic alignment of Alice's polarization basis, observed for six different target states of Bob's measurement basis (***b***), distributed as the six poles on the Poincaré sphere. In all cases, Alice's polarization controller starts at $\boldsymbol{V}=[V_\pi/2,V_\pi/2,V_\pi/2]$. Time averaging and standard deviations are shown from 20 identical runs for each configuration. Coincidence counts for Bob's two detectors (h_b,v_b) with Alice's (h_a) detector for both entangled (τ=0 ps) and non-entangled (τ=500 ps) photons are shown in cyan, blue, orange, and red respectively. Each initial configuration of Bob's h_b measurement direction is shown to the right of every panel.

seconds in all cases. The error bars indicate the statistical spread obtained from 20 independent trials. The dark blue traces show the complementary coincidence rate between h_a and v_b photons, which is maximized when the $P(h_a,h_b)$ is minimized.

The algorithm relies on the polarization entanglement between the two detected photons, and we, therefore, expect the method to fail when this entanglement is impaired or destroyed. To test this, we used the variable delay line to introduce a 500 ps temporal delay between the signal and idler photons prior to the 50/50 beamsplitter, which destroys the polarization entanglement shown in section 2.2. The orange (and red) traces in Fig. 23 show that in this case, the algorithm is unable to consistently minimize (and maximize) the coincidence rate between Alice and Bob, except for the case of $\boldsymbol{b}=\pm S_3$, which we presume was coincidentally close to the case of Bob's axes being aligned to the signal and idler axes of the PPKTP nonlinear crystal.

3.5 Alignment Accuracy

Simulations of our experiment allow us to examine how experimental parameters affect the Nelder-Mead algorithm's ability to align Alice's and Bob's measurement bases. Under stationary conditions, the degree of polarization alignment and attainable extinction ratio in the coincidence rates depends on the integration period per measurement, T, and two counting rates, r_p representing the maximum rate of pair detection (when $\theta_{ab}=\pi$), and r_a the background accidental coincidence rate. In experiments and simulations, the algorithm seeks to minimize the total measured coincidence count,

$$N=N_p+N_a \tag{3.12}$$

where, using the result from (3.10), we model N_p as a Poisson-distributed random variable with mean $r_pT(1-\cos\theta_{ab})$ and N_a as an independent Poisson-distributed random variables with mean r_aT. Taken together, the number of coincidences, N, measured in an integration interval, T, can

be modeled by a discrete Poisson distribution with a mean that depends on the misalignment angle θ_{ab}

$$p_N(k)=P(N=k)=\frac{(r(\theta_{ab})T)^k}{k!}e^{-r(\theta_{ab})T}\ , \qquad r(\theta_{ab})=r_p(1-\cos\theta_{ab})+r_a \quad . \tag{3.13}$$

To assess the impact of quantization noise and integration time on alignment, we conducted a series of Monte Carlo numerical simulations using different values of r_p, r_a and T. The simulations employ the same Nelder-Mead algorithm as the experiments and the polarization actuators were modeled as three successive variable retarder waveplates oriented at $0°$, $45°$, and $0°$. After converging to a coincidence minimum, we evaluate the angular deviation between Alice's final polarization state $\boldsymbol{a}$ and Bob's target state $\boldsymbol{b}$ as $\theta_{\text{error}}=\cos^{-1}(\boldsymbol{a}\cdot\boldsymbol{b})$. θ_{error} is then averaged over 100 uniformly distributed target states on the Poincaré sphere for each data point. Fig.24(a) shows the simulated alignment error θ_{error} as a function of the integration time T, for r_p = 800 pairs/s and r_a = 60 pairs/s, which correspond to one set of experimental conditions considered here. With these coincidence rates, we chose five seconds as a compromise between a low polarization alignment error angle and a fast total alignment time.

Fig. 24(b) shows the average alignment error as a function of r_pT and r_aT. As expected, for a fixed average background count level (r_aT), the alignment accuracy improves with increasing average pair count (r_pT). Conversely, for a fixed average pair count, increasing the average background count decreases the alignment accuracy. The diagonal lines are contours of constant coincidence-to-accidental ratio (r_p/r_a), indicating the performance that can be achieved by adjusting the integration period T alone when the count rates are otherwise fixed. The two data points, (i) and (ii), within figure 24(b) mark the experimental conditions used for the deployed fiber loopback configuration (with T=20 seconds) and for back-to-back conditions (with T=5 seconds), respectively.

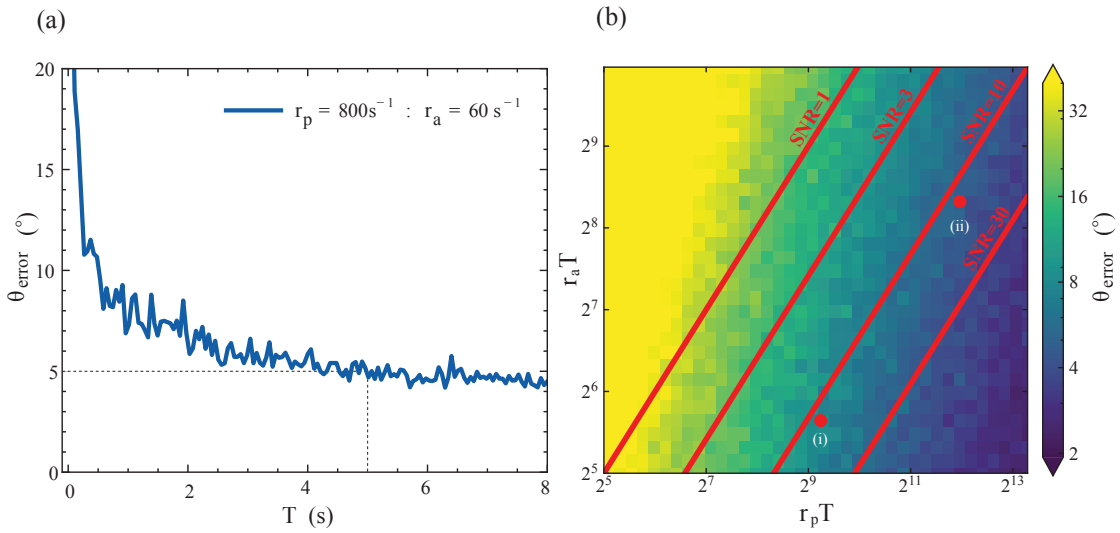

Figure 24: (a) Simulated alignment error as a function of the integration period T, assuming Poisson counting statistics for the coincidence detection rate (3.13). (b) Alignment error as a function of the average pair detection level r_pT and the average accidental coincidence count r_aT. The lines indicate contours of constant signal-to-noise (coincidence-to-accidental) ratios. The points marked (i) and (ii) correspond to the experimental data rates of the deployed and in-lab fiber spans respectively.

Though not shown here, the simulations produced an extinction ratio approaching r_a/r_p, provided the method converges.

3.6 Polarization Tracking

To evaluate the capability of the method in a real fiber transmission system, we used a 7.1 km deployed dark fiber link composed of a metropolitan buried SMF-28 singlemode fiber in a loopback configuration between the Laboratory for Telecommunication Sciences and the University of Maryland and back, shown in figure 25(a). Fig. 25(b) shows an optical time domain reflectometry (OTDR) trace of the fiber span, which has a net insertion loss of 4.2 dB, and a total round-trip delay of 34.6 μs. This latency adds additional time to the alignment time, but is small relative to the total integration time of 20 seconds. For larger networks where classical communication takes place over greater spatial spans and the information of photodetection must

be relayed, the latency will be greater than just the pure propagation time and will be something to investigate in the figure. Prior to alignment, we used a classical laser and polarimeter to observe the polarization evolution in this loop over a typical 72-hour period and observed an average drift rate of 0.1° per hour in the interior angle between the initial Stokes vector and the Stokes vector at later times. Using the analysis from section 1.2, the average time to hit 5% error was $\tau_{e_{th}=5\%}$=56.1 hours or a drift speed of P_{ds}=.008 °/hour. When the 7.1 km loop was inserted into Bob's channel, our tracking algorithm was able to quickly align Alice's detector basis and maintain alignment over a 4 hour period, as shown in Fig. 25(c).

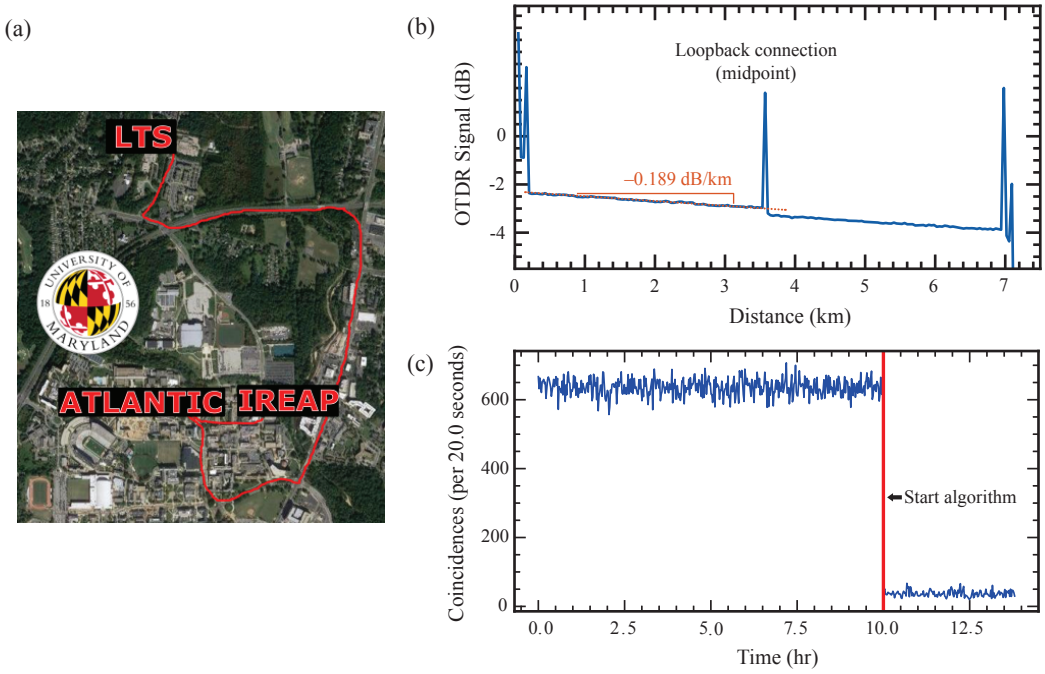

Figure 25: (a)Map of the underground fiber from LTS to the University of Maryland campus. (b) Optical time-domain reflectometry (OTDR) data of the deployed 7.1 km fiber span was inserted into Bob's channel to evaluate the polarization tracking method. (c) Measured coincidence rate between Bob's h_b detector and Alice's h_a detector, before and after enabling the alignment algorithm.

Because the drifts experienced in our deployed fiber are slow, we tested the tracking capability of our method by introducing a controlled drift in Bob's measurement basis using the piezoelectric actuator. Again, using a classical laser and polarimeter, the first three piezoelectric stages in

Bob's actuator were adjusted such that the remaining actuator caused the polarization to trace a great circle, thus providing the maximum amplitude of drift. The voltage across the fourth actuator controls the rotational angle θ_B seen in Fig. 26b. This actuator was then programmed with a sawtooth waveform with a voltage amplitude of V_π and a slope corresponding to $180°$/hr (shown by the green curve in Fig. 26(a)), which are nearly three orders of magnitude faster than what was observed in the 7.1 km deployed fiber. An additional manual polarization controller then projects this great circle into the nodes of Bob's PBS. Fig. 26 shows the great variability in coincidence counts observed during the first two hours when the alignment and tracking algorithm was disabled, and the subsequent minimization of the coincidence rate over a 2 hour period after the algorithm is enabled.

The main bottleneck in the algorithm's total alignment time and tracking speed is the coincidence count integration time, which determines the rate at which the coincidence rate can be sampled and the polarization setting updated. As shown in Fig. 6, the integration period required for accurate alignment also depends upon the counting rate, which decreases with the link loss and detection efficiency.

To assess the tracking capability of our system, we extended the Monte Carlo simulations to model the case when the target polarization state $\boldsymbol{b}(t)$ steadily traverses a great circle on the Poincaré sphere. While the tracking capability also depends upon the noise levels and numerical parameters of the algorithm, for the experimental rates considered here, simulations reveal that the algorithm could maintain alignment provided the target was moving slower than $0.5°$ per integration period. The Nelder-Mead algorithm, like most optimization algorithms, is not intended to track a moving minimum. The vertex record a prior memory of the past coincidence count values as a function of the polarization controller's settings. A moving minimum can interfere with accuracy of prior, well performing vertex points and cause problems with convergence if the drift

is too fast. One area of future work is to investigate optimization algorithms with no measurement history, like stochastic gradient descent, for their ability to track drifts in comparison to derivative free algorithms like the Nelder-Mead simplex method. To allow the Nelder-Mead to work in a tracking fashion the maximum number of iterations a given convergence could take was capped at 30, which as figure 23 shows, is just enough for any orientation of Alice's and Bob's projection orientation to become coaligned. After 30 iterations a new Nelder-Mead simplex process was started with new measurements to reset the vertex values.

The timescale of polarization drift in optical fibers depends upon the length of the fiber as well as the deployed environment (spooled, aerial, buried, or subsea). For the 7.1 km length buried fiber considered here, the drift rate was well below this limit, even for integration periods as long as 20 seconds. The forced drifting measurements in Fig. 26 show successful tracking when the target is drifting 0.25° per measurement period.

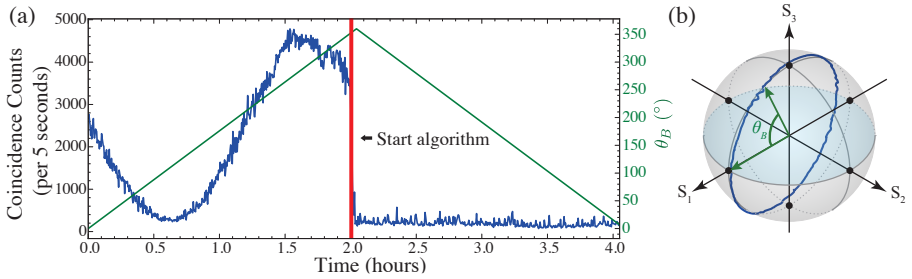

Figure 26: Alice tracking Bob's drifting measurement base. a) Coincidence counts between Alice's and Bob's horizontal detectors when Bob's measurement base drifts at a speed, $\omega_B = \Delta\theta_B/\Delta t = 176.1^\circ$ per hour. b) An example of a great circle sweep of Bob's measurement base where the rotation angle $\theta_B(t)$ is controlled by the voltage.

3.7 Conclusion

In this chapter, we reported on a way to use non-local correlations of an entangled state to orient and dynamically track two spatially separated measurement bases. We present a theory for the coincidence rate for arbitrarily polarized measurement bases, which generalizes the more

commonly used result from linearly polarized bases. The alignment routine uses the Nelder-Mead algorithm to manipulate the polarization controller of one individual to minimize the joint coincidence counts between separate observers. The experimental implementation acquires alignment and minimizes the coincidence rate within approximately 160 seconds.

The alignment strategy is confirmed to work for any arbitrary initial orientation of the two observers' measurement bases and can achieve alignment by minimizing coincidences even when the underlying photon count rates are observed to be statistically unpolarized. The method relies on the entangled state $|\Psi^-\rangle$, and we show that when the entanglement is broken, the method fails to converge.

In addition to acquiring alignment on a stationary basis, the method is able to dynamically track and stabilize the measurement of entanglement over a 7.1 km deployed fiber loop over several hours of operation and also under a controlled drifting environment.

Our method relies only on the entangled state and does not employ classical polarized pilot tones, temporal multiplexers, wavelength filters, or additional polarimetry in order to achieve alignment. This technique could find applications in quantum key distribution, teleportation, entanglement swapping, or locality-violation experiments. Although these applications may require a series of coordinated sequential measurements between receivers, the polarization alignment and tracking method presented here lays the groundwork for more sophisticated alignment methods demanded by future quantum measurement systems.

3.8 Full Measurement Frame Alignment

As discussed in section 1.1.2, for Alice and Bob to align their measurement frames fully, and hence their Poincaré spheres from fully equalizing the unitary transforms of their fibers, two nonorthogonal measurement bases must be aligned. After the publication of the work contained

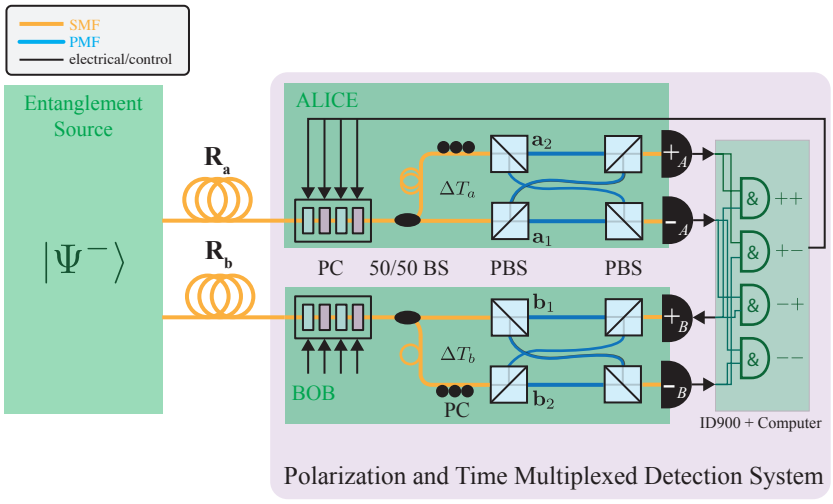

Figure 27: Experimental diagram for full polarization alignment using the polarization and time multiplexed detection setup.

within this chapter, the timing correlator produced by IDQuantique, ID900, was purchased so that two measurement frames could be aligned simultaneously. The specifics of the experiment and how all the coincidence signals are pieced out from the inter-arrival time are presented in more detail in the following section 4.3. The main advantage is that only four detectors and four electrical inputs are needed within the coincidence counting electronics to process all sixteen coincidence signals. The inspiration for this setup was based on the polarization and time multiplexed setup from Grünenfelder *et al* [100] and extended to work for coincidence counts from photon pairs produced from SPDC sources. The polarization and time multiplexed setup is shown in figure 27.

Alice's h port from before is now the positive port from her two projection bases $\boldsymbol{a}_1$ and $\boldsymbol{a}_2$ and likewise with Bob. The coincidence count $N_{+_1-_1}$ refers to the coincidence count from the positive port of Alice's $\boldsymbol{a}_1$ PBS and the negative port of Bob's $\boldsymbol{b}_1$ PBS. Through backpropagation a classical signal and using a manual polarization controller in Alice's and Bob's polarization and time multiplexed setup we can align Alice's and Bob's Stoke measurement projection directions to be orthogonal to each other, i.e. $\boldsymbol{a}_1 \cdot \boldsymbol{a}_2 = 0$ and $\boldsymbol{b}_1 \cdot \boldsymbol{b}_2 = 0$. Using the Nelder-Mead optimization

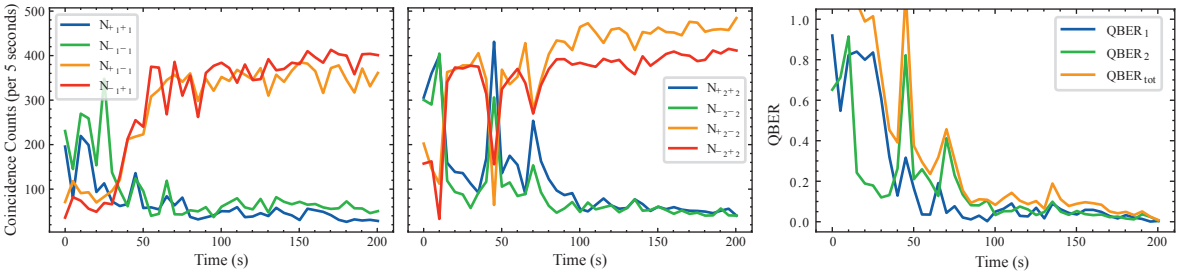

Figure 28: Representative example of full polarization state alignment minimizing the coincidence counts of all like ports where Alice and Bob share the maximally entangled $|\Psi^-\rangle$.

algorithm we can iteratively converge on the minimization of the coincidence count rate from all like ports $+_1+_1$, $+_2+_2$,$-_1-_1$, and $-_2-_2$. This is shown in figure 28. Additionally, after subtracting out the accidental coincidence count rates we plot the quantum bit error rate (QBER) in each measurement base where QBER_1 refers to the QBER from misaligned $\boldsymbol{a}_1$ and $\boldsymbol{b}_1$ and QBER_2 refers to the QBER from misaligned $\boldsymbol{a}_2$ and $\boldsymbol{b}_2$. The total QBER is the sum of each (1.84).

Chapter 4

CHSH Parameter Optimization as an Entanglement Estimate

"Quantum theory is nonlocal."

Nicolas Gisin

This chapter describes the experimental investigation on aligning polarization measurement frames to maximize the CHSH parameter as an estimate for the amount of entanglement shared between two people, Alice and Bob [2]. In section 4.1 we cover the prior literature for using quantum signals as feedback for CHSH parameter estimation, in section 4.2 we briefly outline the theory behind the CHSH parameter that was also shown in section 1.6, in section 4.3 and 4.4 we outline the experiment and experimental impairments, in 4.5 we present the data on finding maximal CHSH violations, and in 4.6 we discuss how we chose the hyperparameters values for the alignment algorithms.

4.1 Introduction

When a quantum state is transmitted and distributed over uncontrolled fiber spans, the spatially separated observers will observe errors in their quantum information protocols associated with the misalignment of their measurement bases. This is also true for measurements that are used to characterize the amount of entanglement the quantum state possesses. A method to evaluate the quality of entanglement in a system in an automated way is, therefore, highly desirable. Such characterization would guarantee, in practical real-world scenarios, that the quality of the distributed polarization entangled photon pairs is sufficient for the relevant quantum information protocols that will use them.

Many approaches for ensuring entanglement quality require knowledge of the density matrix acquired from quantum state tomography. For a bipartite entangled state, quantum state tomography requires the two individuals to make nine coordinated measurements from all combinations of three aligned measurement directions (3^2=9) [89], for more information see section 2.2. One way to reduce the number of aligned and coordinated measurement bases is to use an entanglement witness as a proxy for full quantum state tomography [49, 101, 102]. A common entanglement witness for two qubits is the measurement of nonlocality through the violation of a Bell inequality [49, 52, 103, 104]. The Bell violation we use here is the version first studied by Clauser, Horne, Shimony, Holt (CHSH) [51], where the measurement of a parameter S exceeding 2 indicates the presence of nonlocality and importantly, entanglement. Although entanglement could exist in mixed states even when $S<2$, the Bell parameter S is nonetheless a common, useful measure of entanglement quality. The value of S is determined by two individuals using 4 measurements consisting of all combinations of two measurement directions (2^2=4), see section 1.6 for more information. The reduction from three to two measurement projection directions per observer reduces the experimental complexity and is commonly used in QKD experiments.

To find optimal measurement projection vectors in the presence of uncontrolled polarization transformations, various experimental and computational methods have been explored, including multiplexing classical pilot tone calibration signals with the quantum signals [21, 34–37, 44, 93] or using only quantum signal-based polarization control [1, 31, 41–43, 94]. To specifically find maximal Bell violations using only feedback from measurements of the entangled photons, computational studies using various optimization techniques and machine learning have been investigated [105–111], but experimentally only a free space implementation at 800 nm has been studied [60]. Our fiber-based, telecom wavelength experiment using commercial off-the-self components, with controllable impairments, investigates entanglement quality using Bell violations

in a much more realistic setting for quantum networks.

We report here on an experiment to find the optimal orientation for the four needed projection vectors using a time and polarization multiplexed detection system modeled after the QKD experiment by Grünenfelder [100]. This setup has a few key advantages: it reduces the number of detectors needed by half and it allows the value of S to be determined in one measurement integration period without needing to toggle between different polarization settings, which could otherwise introduce hysteresis errors in the polarization actuators. Our entanglement source also allows us to tune the amount of entanglement shared between two observers by varying the relative arrival time of two photons at an entangling 50/50 beamsplitter. Using this setup, we examined the ability of several optimization algorithms to maximize the CHSH inequality in the presence of different levels of entanglement. The methods we investigated were Nelder-Mead optimization [98], stochastic gradient descent, and Bayesian optimization [112].

4.2 Theory on CHSH parameter estimation

As discussed in the introduction 1.6 the value of the CHSH parameter, S, is calculated using four sets of local measurements from two separated parties, Alice and Bob, on a two particle quantum state $\hat{\rho}$. To describe S we assume Alice performs polarization-resolved measurements along two different projection directions denoted by the unit vectors $\boldsymbol{a}_1$ and $\boldsymbol{a}_2$ in Stokes space. Bob likewise performs his polarization-projected measurements along directions $\boldsymbol{b}_1$ and $\boldsymbol{b}_2$. For two qubits the CHSH parameter [51] is

$$S(\boldsymbol{a}_1,\boldsymbol{a}_2,\boldsymbol{b}_1,\boldsymbol{b}_2)=\mathrm{Tr}(\hat{\rho}\hat{A}_1\otimes\hat{B}_1)+\mathrm{Tr}(\hat{\rho}\hat{A}_1\otimes\hat{B}_2)+\mathrm{Tr}(\hat{\rho}\hat{A}_2\otimes\hat{B}_1)-\mathrm{Tr}(\hat{\rho}\hat{A}_2\otimes\hat{B}_2) \tag{4.1}$$

where for example $\hat{A}_i=\boldsymbol{a}_i\cdot\boldsymbol{\sigma}$ and $\boldsymbol{a}_i$ is the Stokes measurement projection direction for Alice's i^{th} measurement and $\boldsymbol{\sigma}=(\sigma_1,\sigma_2,\sigma_3)$ are Pauli matrices [61]. This is the same for Bob's j^{th} measurement $\hat{B}_j=\boldsymbol{b}_j\cdot\boldsymbol{\sigma}$. When the shared state is the maximally entangled singlet state $\hat{\rho}=|\Psi^-\rangle\langle\Psi^-|$ where $|\Psi^-\rangle=1/\sqrt{2}(|H_aV_b\rangle-|V_aH_b\rangle)$ equation (4.1) reduces to

$$S(\boldsymbol{a}_1,\boldsymbol{a}_2,\boldsymbol{b}_1,\boldsymbol{b}_2)=-(\boldsymbol{a}_1\cdot\boldsymbol{b}_1+\boldsymbol{a}_1\cdot\boldsymbol{b}_2+\boldsymbol{a}_2\cdot\boldsymbol{b}_1-\boldsymbol{a}_2\cdot\boldsymbol{b}_2) \quad . \tag{4.2}$$

Using the well known Bell linear polarization projection orientations $\boldsymbol{a}_1=(1,0,0)$, $\boldsymbol{a}_2=(0,1,0)$, $\boldsymbol{b}_1=1/\sqrt{2}(1,1,0)$, and $\boldsymbol{b}_2=1/\sqrt{2}(1,-1,0)$ we get the maximal Bell violation $|S|=2\sqrt{2}$.

The CHSH parameter S can be experimentally measured using the coincidence counts from the four combinations of Alice's and Bob's two measurement bases

$$\begin{aligned} S&=C(\boldsymbol{a}_1,\boldsymbol{b}_1)+C(\boldsymbol{a}_1,\boldsymbol{b}_2)+C(\boldsymbol{a}_2,\boldsymbol{b}_1)-C(\boldsymbol{a}_2,\boldsymbol{b}_2) \\ C(\boldsymbol{a},\boldsymbol{b})&=\frac{N_{++}(\boldsymbol{a},\boldsymbol{b})+N_{--}(\boldsymbol{a},\boldsymbol{b})-N_{+-}(\boldsymbol{a},\boldsymbol{b})-N_{-+}(\boldsymbol{a},\boldsymbol{b})}{N_{++}(\boldsymbol{a},\boldsymbol{b})+N_{--}(\boldsymbol{a},\boldsymbol{b})+N_{+-}(\boldsymbol{a},\boldsymbol{b})+N_{-+}(\boldsymbol{a},\boldsymbol{b})} \end{aligned} \tag{4.3}$$

where $C(\boldsymbol{a},\boldsymbol{b})$ is typically referred to as the correlation measure and $N_{+-}(\boldsymbol{a},\boldsymbol{b})$, for instance, is the coincidence count between Alice's plus detector and Bob's minus detector for an integration time T where the polarization measurement projections on $\hat{\rho}$ given the fiber and Alice's and Bob's polarization controllers' rotational transformations are $\boldsymbol{a}$ and $\boldsymbol{b}$. The correlation measure is the sum of the probability that like detectors fire together ($++$ and $--$) minus the probability that opposite detectors fire together ($+-$ and $-+$). For example, the probability that $+-$ detectors fire together is

$$P_{+-}=\frac{N_{+-}(\boldsymbol{a},\boldsymbol{b})}{N_{++}(\boldsymbol{a},\boldsymbol{b})+N_{--}(\boldsymbol{a},\boldsymbol{b})+N_{+-}(\boldsymbol{a},\boldsymbol{b})+N_{-+}(\boldsymbol{a},\boldsymbol{b})} \quad . \tag{4.4}$$

In maximizing the CHSH parameter, the optimal orientation for the measurement projection directions is for $\boldsymbol{a}_1$ and $\boldsymbol{a}_2$ to lie within the plane spanned by $\boldsymbol{b}_1$ and $\boldsymbol{b}_2$. Specifically, $\boldsymbol{a}_1=$

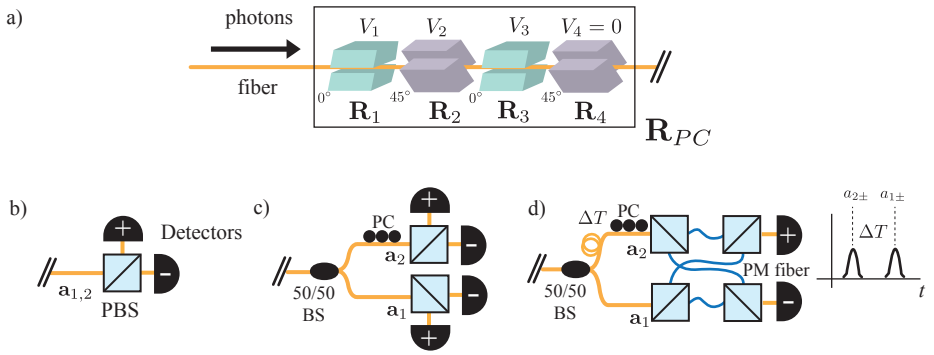

Figure 29: a) Schematic of our piezoelectric actuator polarization controller. Four in series actuators expand due to an applied voltage, V_i, and compress the fiber along specific orientations around the circumference of the fiber. The photons get rotated by a total rotational transformation of $\boldsymbol{R}_{PC}$. The photons can be projected onto two projection bases, $\boldsymbol{a}_{1,2}$, from toggling known polarization transforms controlled by the polarization controller (b), from probabilistic splitting of a 50/50 beamsplitter and four photon detectors (c), or from probabilistic splitting of a 50/50 beamsplitter and two photon detectors from a polarization and time multiplexed setup (d).

$\frac{1}{\sqrt{2}}(\boldsymbol{b}_1+\boldsymbol{b}_2)$ and $\boldsymbol{a}_2=\frac{1}{\sqrt{2}}(\boldsymbol{b}_1-\boldsymbol{b}_2)$.

Alice can adjust the relative orientation of her measurement bases by preceding her receiver by a polarization controller. Figure 29(a) shows the configuration of the polarization controllers employed here, which use piezoelectric transducers to produce a voltage-controlled birefringence. Three independent stages, nominally oriented at $0°$, $45°$, and $0°$ provide sufficient degrees of freedom to adjust and orient the projection direction $\boldsymbol{a}$ arbitrarily on the Poincaré sphere. The cumulative transformation of the controller can be described as a product of three rotation matrices,

$$\boldsymbol{R}_{\mathrm{PC}}(V_1,V_2,V_3)=\boldsymbol{R}_3(\boldsymbol{r}_3,\delta_3(V_3))\boldsymbol{R}_2(\boldsymbol{r}_2,\delta_2(V_2))\boldsymbol{R}_1(\boldsymbol{r}_1,\delta 1(V_1)) \tag{4.5}$$

where V_i is the voltage applied to the i^{th} piezoelectric actuator, and $\boldsymbol{R}(\boldsymbol{r},\delta)$ is a 3×3 matrix describing a rotation by an angle δ about a unit Stokes vector $\boldsymbol{r}$ [6]:

$$\boldsymbol{R}(\boldsymbol{r},\delta)=(\boldsymbol{r}\boldsymbol{r}\cdot)+\sin\delta(\boldsymbol{r}\times)-\cos\delta(\boldsymbol{r}\times\boldsymbol{r}\times) \tag{4.6}$$

This analysis would apply for any polarization controller that uses fixed-axis, variable-retardance actuators, including liquid crystals or electrooptic controllers. In principle, the three input voltages could be computed based upon observations in order to reverse the polarization misalignment [38, 69]. However, for the piezoelectric controllers used here, the dependence of θ_i on the applied voltage V_i and the orientation $\boldsymbol{r}_i$ are unknown a priori and can exhibit hysteresis under large steps. The optimization methods reported here, therefore, treat $\boldsymbol{R}_{\mathrm{PC}}$ as a black box with three voltage inputs that are adjusted iteratively.

As shown in Fig. 29(b), if the photon emerging from the controller is detected using a polarizing beamsplitter and photon counters, the preceding polarization controller can arbitrarily steer the polarization projection $\boldsymbol{a}$. To resolve the photon along two independent directions, a non-polarizing 50/50 coupler can be used to randomly pass the photon to one of two polarizing beamsplitters, which define $\boldsymbol{a}_1$ and $\boldsymbol{a}_2$ as shown in Fig. 29(c). In this configuration, the relative angle between $\boldsymbol{a}_1$ and $\boldsymbol{a}_2$ is preserved by the upstream polarization controller. Fig. 29(d) shows the arrangement used here, in which the four output channels are polarization multiplexed with a relative time delay ΔT [100]. This configuration allows two detectors to distinguish between four different outcomes by their relative arrival times, provided the photon counting detectors can resolve both polarization states.

4.3 Experiment

Fig. 30 shows the experimental apparatus used to create and measure polarization-entangled photons. Polarization-entangled photons are generated from the arrival of two cross polarized photons produced from a type-II spontaneous parametric downconversion process at an entangling 50/50 beam splitter. This process is described more extensively in the prior chapter 2.

This setup affords us specific control over the amount of entanglement generated by controlling

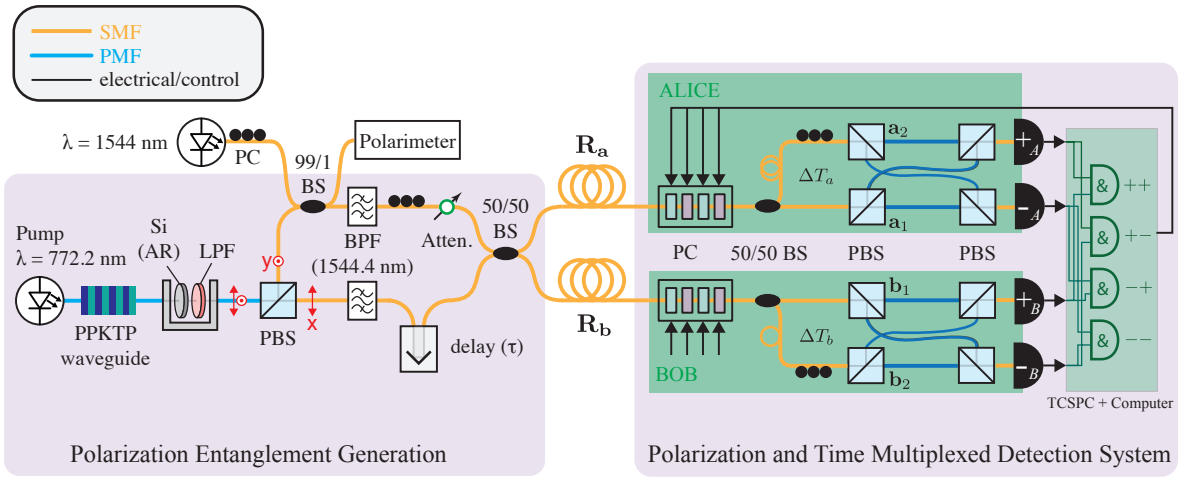

Figure 30: Experimental diagram of our polarization entanglement generation setup and our time-multiplexed polarization detection system, both outlined in purple. Entanglement is controlled through the temporal overlap of each photon (τ), at a 50/50 beam splitter. SMF: single-mode fiber, PMF: polarization-maintaining fiber, AR:anti-reflection coating, LPF:longpass filter, PC:polarization controller, BPF:bandpass filter, $\boldsymbol{R}_a(\boldsymbol{R}_b)$: rotational transformation of Alice's (Bob's) fiber span, PBS:polarization beamsplitter, BS:beamsplitter, TCSPC:time-correlating single-photon counting module.

the temporal overlap of the two cross polarized (horizontal and vertical) photons at the entangling beamsplitter from a controllable time delay stage (τ) in one arm of the entangling interferometer. As was shown in chapter 2, when Alice and Bob post select on events that are measured by both parties, the output state is cast into a superposition of a pure maximally entangled state, $|\Psi^-\rangle\langle\Psi^-|$, and the classically correlated mixed state, $\hat{\rho}_{\text{class}}$ using equation (2.28) [81, 82],

$$\hat{\rho}=\mathcal{C}\left|\Psi^-\right\rangle\left\langle\Psi^-\right|+(1-\mathcal{C})\rho_{\text{class}} \tag{4.7}$$

where $\mathcal{C}$ is the concurrence of $\hat{\rho}$, and defines the amount of entangled versus classical correlation between the two exiting photons. With central frequency ω_0 and bandwidth $\Delta\omega$ for each photon, the concurrence can be written as

$$\mathcal{C}=e^{-\Delta\omega^2\tau^2} \tag{4.8}$$

where τ is the controllable time delay between the photons incident on the entangling beamsplitter. The bandwidth, $\Delta\omega$, is related to the full-width-half-maximum (FWHM) of the filter measured to be 1.4 nm. The corresponding frequency bandwidth is

$$\Delta\omega = \frac{\pi c \Delta\lambda_{\text{FWHM}}}{\sqrt{2\ln 2}\lambda_0^2} = 0.46 \text{ rad/ps} \quad .$$

Imperfections in the splitting ratios of the entangling beamsplitter, the relative location and spectral width of the filters, white noise sources, and the polarization orientation of the classically mixed state can have an impact on the density matrix, CHSH parameter, and entanglement quality. The impact of these can be seen in the following section and in Brewster *et al* [113]. When the polarization projection directions are optimally aligned, substituting equations (4.7) and (4.8) into (4.1) gives

$$|S(\tau)| = \sqrt{2}\left(1 + e^{-\Delta\omega^2\tau^2}\right) \quad . \tag{4.9}$$

The maximal Bell violation of $2\sqrt{2}$ occurs for $\tau = 0$. This theoretical line, data from our experiment, and the linear fit of $|S(\tau)| = A + Be^{-\Delta\omega^2\tau^2}$ is shown in figure 31. The fit parameters, A and B, are discussed in the following section.

The alignment for the linear polarization basis, shown within figure 31a, was done using a classical 10mW CW 1544nm pilot tone with a polarimeter and power meters to measure all eight output ports of $\boldsymbol{a}_1$,$\boldsymbol{a}_2$,$\boldsymbol{b}_1$,$\boldsymbol{b}_2$. Alignment of the proper projection directions, say $\boldsymbol{a}_1$ to $(1,0,0)$, was done by first adjusting the PC after the pilot tone until the polarization state recorded by the polarimeter was $(1,0,0)$ then Alice's piezoelectric actuator PC was adjusted until all power was transmitted through the positive port of $\boldsymbol{a}_1$'s polarization beam splitter and near zero through the negative port. This was done for $\boldsymbol{a}_2$ to $(0,1,0)$ through the same method only a manual polarization controller before $\boldsymbol{a}_2$ was adjusted leaving $\boldsymbol{a}_1$ unchanged. The same technique was used to align $\boldsymbol{b}_1$

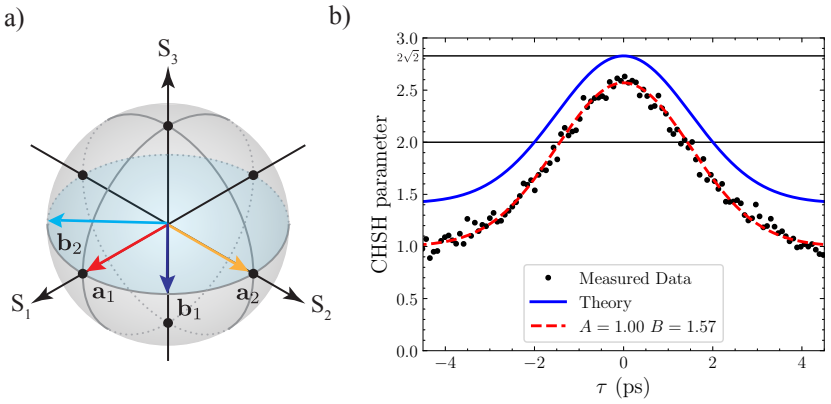

Figure 31: (a) Measurement of the projectors $\boldsymbol{a}_{1,2}$ and $\boldsymbol{b}_{1,2}$. (b) CHSH parameter as a function of the temporal mismatch of the two photons at our entangling 50:50 beam splitter. A fit to the data $|S(\tau)|{=}A{+}Be^{-\Delta\omega^2\tau^2}$ is shown in red alongside the theoretical line in blue from equation (4.9).

to $1/\sqrt{2}(1,1,0)$, and $\boldsymbol{b}_2$ to $1/\sqrt{2}(1,{-}1,0)$. The alignment pilot tone and polarimeter were inserted into one of the entangling interferometer arms with a 99/01 beam splitter to minimize photon loss from the SPDC source, but to still permit classical power measurements above the power meters' noise floor. After aligning to the known maximal projection directions, turning off the pilot tone, disconnecting the power meters and reconnecting the super conducting single photon counting nanowire detectors (SNSPDs), care was taken to attempt to align the two photon's polarization within the entanglement interferometer arms to the horizontal and vertical polarization orientation set by $\boldsymbol{a}_1$. In theory near perfect alignment to the horizontal and vertical polarization direction is possible, but was not achieved here due to unavoidable polarization rotations that occur when the fiber is disconnected and reconnected.

The two spatially separated receivers (here denoted Alice and Bob) each include a fiber-based polarization controller with four piezoelectric actuators [General Photonics PolaRITE III], 50/50 beamsplitters, polarization beamsplitters, a pair of SNSPDs with quantum efficiencies up to 80% [Opus One, Quantum Opus LLC.], and a time-correlating single-photon counting (TCSPC) instrument [ID900, ID Quantique] where real time coincidence measurements can be processed

and results can be fed back to the upstream polarization controllers.

The polarization and time multiplexed detection setup that both Alice and Bob have has been constructed so that the path difference between a photon heading towards $\boldsymbol{a}_1$ is 40 cm (2 ns) shorter than the photon heading towards $\boldsymbol{a}_2$. Likewise the photon heading towards $\boldsymbol{b}_1$ experiences a 20 cm (1 ns) shorter path than a photon heading towards $\boldsymbol{b}_2$ leaving $\Delta T_a{=}2\Delta T_b$. All other fiber paths within the detection setup were kept as close to equal as possible. The coincidence peaks in our experiment exhibit a statistical width of approximately 300 ps due to timing jitter in detection, and the path delays of 1 ns and 2 ns were chosen to ensure that the correlation peaks are clearly distinguishable. In this configuration, the interarrival time histogram between one of Alice's detectors and one of Bob's detectors will exhibit four distinct correlation peaks, representing early-early, late-early, early-early, and late-late photon pairs. This temporal correlation pattern can be measured even though the photons are continuous-wave (not pulsed) and spontaneously generated.

This allows us to make the 16 different measurement combinations needed within equation (4.3) in one time integration period without toggling between polarization projection directions for Alice and Bob. An example of a given 16 signal coincidence measurement and the related joint detection probability leading to a Bell violation ($S{=}2.56$), is shown in figure 32.

One assumption of this method is that the photon counters can detect both polarization states with comparable efficiency. However, as we showed in section 2.3, the superconducting nanowire detectors employed here have a polarization-dependent efficiency so a manual polarization controller (not shown) was inserted prior to each detector in order to equalize the quantum efficiency between the early and late arriving photon channels. If the efficiencies are not equalized, the resulting polarization dependent loss (PDL) can impact the count rates and alter the calculated CHSH value (4.3). We note that newer nanowire constructions such as winding different nanowire geometries

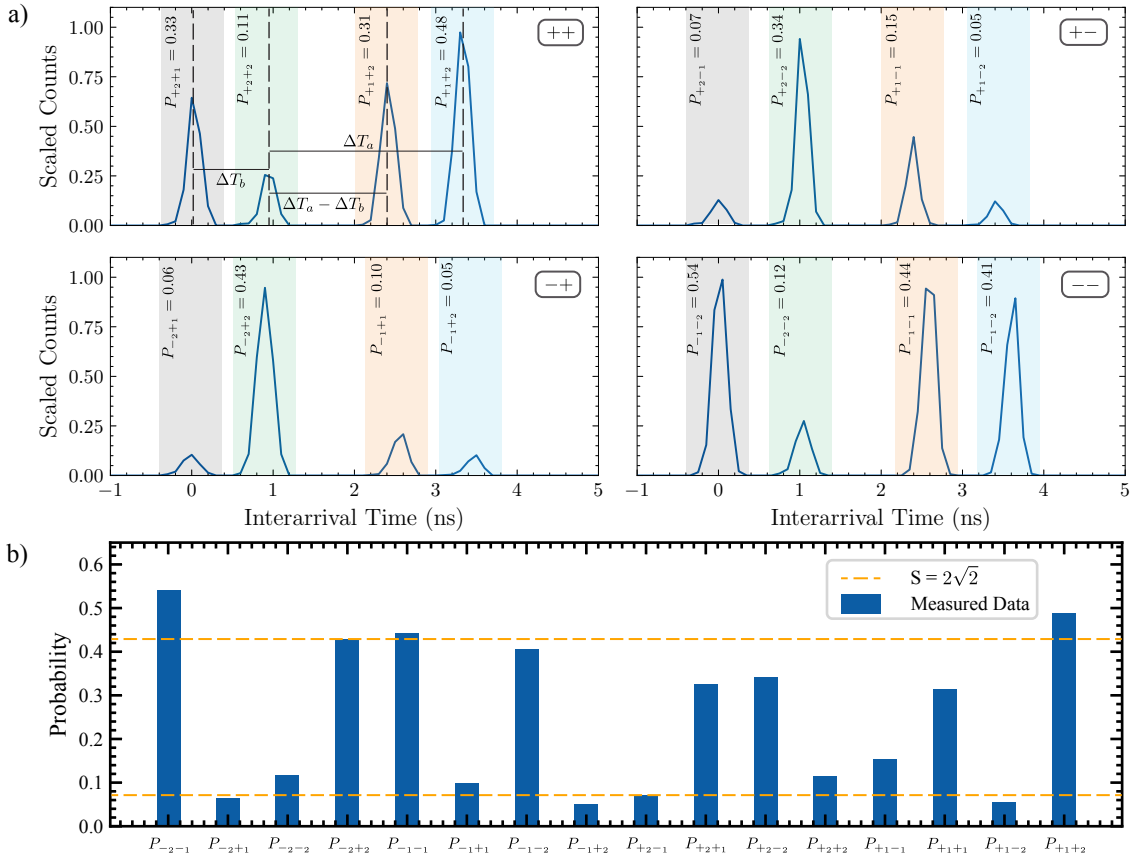

Figure 32: a) Example of a 16 peak signal from the four histograms across Alice's and Bob's two detectors ($\pm\pm$) due to the time multiplexed set up of Figure 30. The detector pair used for each histogram is given in the top right of each plot. These measurements were made after a Nelder-Mead optimization routine maximized the CHSH parameter with a final value of $|S|=2.56$. The total counts within each colored portion can be used to determine the coincidental probabilities from equation (4.4). Within the first plot the temporal separation of the four signals are shown with respect to the temporal delays, ΔT_a and ΔT_b, from the different paths within the polarization and time multiplexed setup. b) For ideal $S=2\sqrt{2}$ and state $\hat{\rho}=|\Psi^-\rangle\langle\Psi^-|$ the probability should be either $\frac{1}{4}(1\pm\frac{1}{\sqrt{2}})\approx 0.07$ or 0.43, shown as the dotted orange line with respect to measured probabilities.

together in stacks, using spiral winding geometries, or stacking different materials with near field optic effects can reduce this polarization-dependent efficiency [114–117].

An example of Alice's and Bob's measurement bases before and after Alice tries to align to a random configuration of Bob's measurement bases from the maximization of S is shown in figure 33. As before, the orientation of the projection bases is determined using the pilot tone laser and power meters. The pilot tone was not used during the maximization process and only used before and after the fact to determine the orientation of the projection bases to confer that their measurement bases are interleaved as would be expected for the condition that maximizes equation (4.2). The insets above figure 33 show an initially arbitrary orientation of Alice's and Bob's projection bases, but after the maximization of S Alice's and Bob's projection bases are nearly interleaved on the same plane, shown as red and blue dotted lines, as is expected.

4.4 Impairments on CHSH parameter

Experimental imperfections can impact the density matrix, equation (4.7), and also the CHSH parameter. The first section deals with spectral imperfections in the entanglement interferometer, and the second deals with deviations from general photon indistinguishability and polarization misalignment between the classically mixed state and projection bases of Alice and Bob.

4.4.1 Filter Impairments

Instead of having identical filters in the entanglement interferometer, let us assume that the two filters can differ in both spectral width and location. The emitted photon pair coming out of the PPKTP waveguide is best described by the state

$$|\psi\rangle = \int d\omega_s d\omega_i f_0(\omega_s,\omega_i)\hat{a}_x^\dagger(\omega_s)\hat{a}_y^\dagger(\omega_i)|0\rangle \tag{4.10}$$

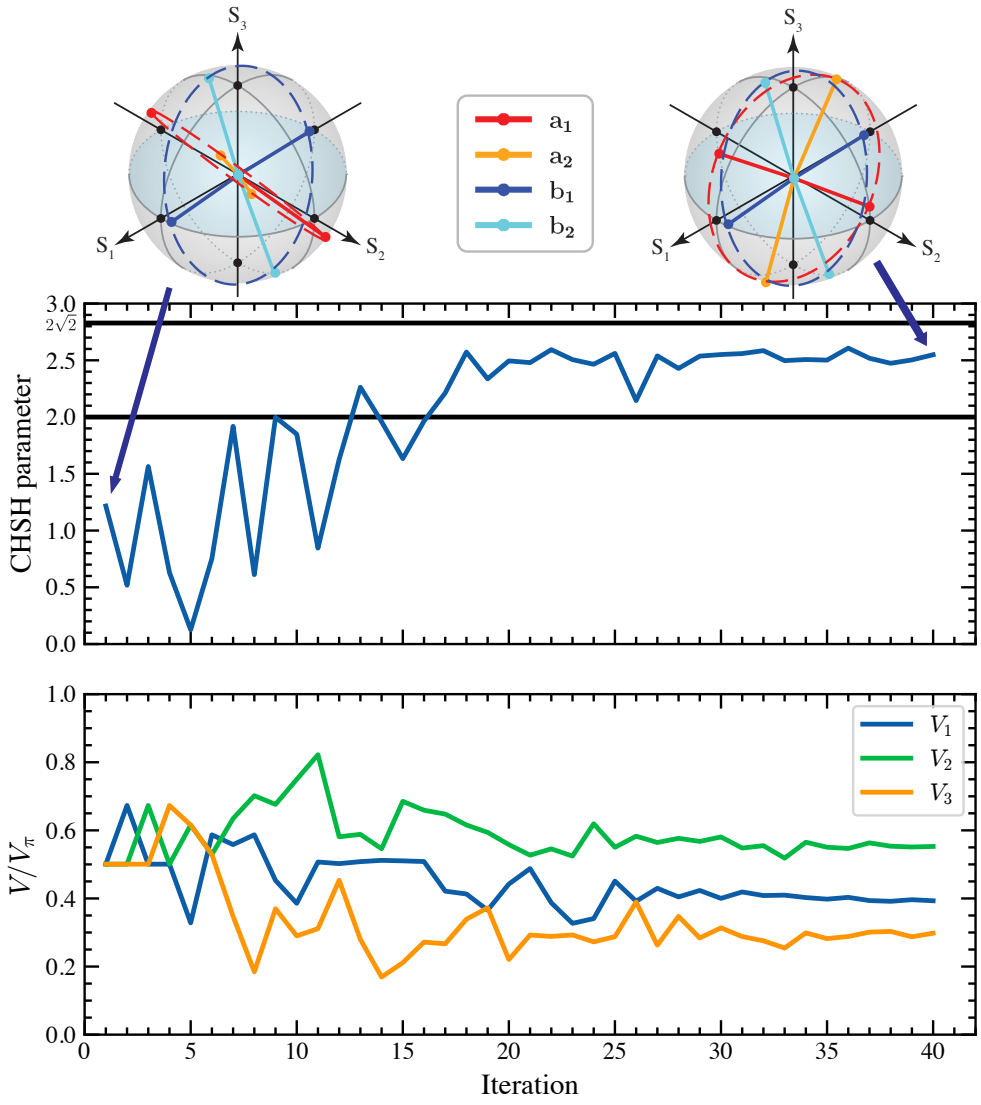

Figure 33: Representative example of maximizing the CHSH parameter by changing the voltages of Alice's polarization controller. Here the optimization algorithm was the Nelder-Mead method. The orientation of Alice's and Bob's projection direction is measured before and after maximizing the CHSH parameter using the alignment method mentioned in the body and shown above the CHSH plot.

where x, y is the horizontal and vertical polarization and f_0 is the joint spectral amplitude for the signal and idler photons $\omega_{s,i}$. For continuous wave pump sources with pump frequency ω_p, pumping a second order nonlinear waveguide with length L, the joint spectrum is seen to produce a sinc profile as was shown and defined in section 2.2:

$$f_0(\omega_s,\omega_i)\propto\text{sinc}\left(\frac{\Delta k(\omega_s,\omega_i)L}{2}\right)\sqrt{\delta(\omega_s+\omega_i-\omega_p)} \tag{4.11}$$

where $\Delta k=k_p(\omega_p)-k_s(\omega_s)+k_i(\omega_i)-\frac{2\pi}{\Lambda}$ is the quasi-phase matching bandwidth of the PPKTP waveguide. The delta function, $\delta(\omega_s+\omega_i-\omega_p)$, ensures energy conservation in the downconversion process. The polarization beamsplitter sends the horizontal photon to the x path and the vertical photon to the y path. Both photons undergo filtering in their paths due to tunable bandpass filters. Each filter can be assumed to be of Gaussian form with a center frequency $\Omega_{x,y}$ and bandwidth $\Delta\omega_{x,y}$

$$f_{\text{filter}}(\omega)\propto\exp\left\{\frac{-(\omega-\Omega)^2}{2\Delta\omega^2}\right\} \quad .$$

If the filters are narrower than the central sinc width then the joint spectrum can be approximated as

$$f_0(\omega_s,\omega_i)\propto\exp\left\{\frac{-(\omega_s-\Omega_x)^2}{2\Delta\omega_x^2}\right\}\exp\left\{\frac{-(\omega_i-\Omega_y)^2}{2\Delta\omega_y^2}\right\}\sqrt{\delta(\omega_s+\omega_i-\omega_p)} \tag{4.12}$$

In [95] the CHSH parameter is determined through the formula

$$S(\tau)=\sqrt{2}\left(1+\frac{K(\tau)}{I}\right) \tag{4.13}$$

for integral quantities

$$I=\frac{1}{2}\int d\omega_s d\omega_i |f_0(\omega_s,\omega_i)|^2 \tag{4.14}$$

$$K(\tau)=\frac{1}{2}\int d\omega_s d\omega_i e^{i(\omega_s-\omega_i)\tau} f_0^*(\omega_i,\omega_s) f_0(\omega_s,\omega_i) \quad . \tag{4.15}$$

Assuming small central frequency and frequency width errors: $\Omega_x=\Omega_y+\varepsilon=\Omega$ and $\Delta\omega_x=\Delta\omega_y+\delta=\Delta\omega$ gives a value for $S(\tau)$

$$S(\tau)=\sqrt{2}\left(1+\exp\left\{\left[-\frac{(2\Delta\omega^2\varepsilon+(\delta^2+2\Delta\omega\delta)(\omega_p-2\Omega))^2}{4\Delta\omega^2(\Delta\omega+\delta)^2[\Delta\omega^2+(\Delta\omega+\delta)^2]}\right]\right\}\exp\left\{\left[-\frac{\Delta\omega^2(\Delta\omega+\delta)^2\tau^2}{\Delta\omega^2+(\Delta\omega+\delta)^2}\right]\right\}\right) \quad . \tag{4.16}$$

The first exponential term represents the reduction factor from the ideal case of $S(\tau=0)=2\sqrt{2}$. For $\Omega=\omega_p/2$ it is interesting to note that any $\varepsilon\neq 0$ reduces S, but increasing the relative width of one filter with respect to the other enhances S as it increases the denominator within the first exponential term.

4.4.2 Photon indistinguishability and the orientation of the classically mixed state

In general, even when $\tau=0$, the temporal overlap of the two cross polarized photons at our entangling 50/50 beamsplitter won't produce the $|\Psi^-\rangle$ state 100% of the time. This could be due to the filter mismatch, shown above, transmission and reflection coefficients that differ from the ideal 50/50 ratio [113], and other frequency and temporal mode imperfections. In fact, this is identical to the reason why when polarization aligned photons meet at a 50/50 beamsplitter the extinction of coincidences from the exit ports of the beamsplitter never perfectly go to zero [95]. This experiment, often named the Hong-Ou-Mandel (HOM) experiment, gives a measure of the two photons indistinguishably [118]. The visibility, V_{HOM}, is the ratio

$$V_{\text{HOM}}=\frac{N(\tau\to\infty)-N(\tau=0)}{N(\tau\to\infty)} \tag{4.17}$$

where τ is the relative temporal delay between the two photon wave packet at the beamsplitter and N is the coincidence rate at the exit ports. Accounting for this we can modify our density matrix describing our experiment, equation (4.7), by letting $\mathcal{C}=V_{\text{HOM}}e^{-\Delta\omega^2\tau^2}$.

In addition to the impairment arising from non-identical photons, when Alice's and Bob's measurement projection directions are not aligned to those of the classically mixed state, the estimated value of S will deviate from the model. Assuming Alice and Bob measure at the normal linear polarization orientations, $\boldsymbol{a}_1=(1,0,0)$, $\boldsymbol{a}_2=(0,1,0)$, $\boldsymbol{b}_1=1/\sqrt{2}(1,1,0)$, and $\boldsymbol{b}_2=1/\sqrt{2}(1,-1,0)$, but that the classically mixed polarization state is created in the basis

$$\hat{\rho}_{\text{class}}=\frac{1}{2}\Big(|nn_\perp\rangle\langle nn_\perp|+|n_\perp n\rangle\langle n_\perp n|\Big) \tag{4.18}$$

where $|n\rangle=\cos(\theta/2)|H\rangle+e^{i\phi}\sin\theta/2|V\rangle$ and $|n_\perp\rangle=-e^{-i\phi}\sin(\theta/2)|H\rangle+\cos\theta/2|V\rangle$. Written out in detail the classically mixed density matrix is

$$\hat{\rho}_{\text{class}}=\frac{1}{2}\begin{pmatrix} \frac{1}{2}s^2 & -cse^{-i\phi} & -cse^{-i\phi} & -\frac{1}{2}s^2e^{-i2\phi} \\ -cse^{i\phi} & 1-\frac{1}{2}s^2 & -\frac{1}{2}s^2 & cse^{-i\phi} \\ -cse^{i\phi} & -\frac{1}{2}s^2 & 1-\frac{1}{2}s^2 & cse^{-i\phi} \\ -\frac{1}{2}s^2e^{i2\phi} & cse^{i\phi} & cse^{i\phi} & \frac{1}{2}s^2 \end{pmatrix} \tag{4.19}$$

where $s=\sin\theta$ and $c=\cos\theta$. The density matrix of our experiment is then written as

$$\hat{\rho}=V_{\text{HOM}}e^{-\Delta\omega^2\tau^2}\big|\Psi^-\big\rangle\big\langle\Psi^-\big|+\Big(1-V_{\text{HOM}}e^{-\Delta\omega^2\tau^2}\Big)\hat{\rho}_{\text{class}} \quad . \tag{4.20}$$

Plugging equation (4.20) into (4.1) gives a CHSH parameter

$$\begin{aligned}|S(\tau)| &= \sqrt{2}\left[1+V_{\text{HOM}}e^{-\Delta\omega^2\tau^2}-(\sin\theta\sin\phi)^2\left(1-V_{\text{HOM}}e^{-\Delta\omega^2\tau^2}\right)\right] \\ &= \sqrt{2}\left[1+V_{\text{HOM}}e^{-\Delta\omega^2\tau^2}-|\boldsymbol{n}\cdot\hat{s}_3|^2\left(1-V_{\text{HOM}}e^{-\Delta\omega^2\tau^2}\right)\right] \\ &= \sqrt{2}\left[1+V_{\text{HOM}}e^{-\Delta\omega^2\tau^2}-(\cos\varphi)^2\left(1-V_{\text{HOM}}e^{-\Delta\omega^2\tau^2}\right)\right]\end{aligned} \tag{4.21}$$

where $\boldsymbol{n}$ is the Stokes vector that corresponds to the Jones projection vector $|n\rangle$, $\hat{s}_3$ is the Stokes unit vector in the right circular polarization direction, and φ is the angle between $\boldsymbol{n}$ and $\hat{s}_3$. With $\varphi=0$ we recover the CHSH parameter expression given within Brewster et al. [95]. The maximum CHSH parameter value attainable at $\tau=0$ is between a maximum value of $|S|=\sqrt{2}(1+V_{\text{HOM}})$ and minimum value $|S|=\sqrt{2}(2V_{\text{HOM}})$ depending upon φ. The HOM visibility for our filtered SPDC source was measured with a maximum value of 93%, shown in figure 20. The theoretical best CHSH parameter given this HOM visibility is between $S=2.63$ and $S=2.73$, which is dependent on the orientation of the classically mixed state.

Brewster et al. have shown that the effect of additive white nose can be modeled by replacing the density matrix with:

$$\hat{\rho}\rightarrow\eta\hat{\rho}+\frac{1-\eta}{4}\hat{I} \quad . \tag{4.22}$$

White, unpolarized, noise can have many origins: polarization independent dark count or accidental coincidence count rates, electrical noise in the detection process, etc [119]. The η term within the density matrix affects the CHSH parameter by a scaling term $|S(\tau)|\rightarrow\eta|S(\tau)|$ [113]. Measuring $|S(\tau)|$ along the linear polarization directions is shown in figure 31, along with a fit to $|S(\tau)|=\sqrt{2}A+Be^{-\Delta\omega^2\tau^2}$. Using equation (4.21), the fit parameters are determined to be $A=\eta(1-\cos^2\varphi)=1.00$ and $B=\sqrt{2}\eta V_{\text{HOM}}(1+\cos^2\varphi)=1.57$. Assuming $V_{\text{HOM}}=0.93$, the white noise term is found to be equal to $\eta=0.95$ and the misalignment term $\cos^2\varphi=0.25$. This equates to a misalignment

from the linear polarization equator of $30°$.

4.5 Finding Maximal CHSH Violations

Being able to change the relative degree of entanglement between Alice and Bob allowed us to examine how various optimization algorithms compare to each other in a real-world setting. Nelder-Mead methods have been used in quantum experiments on entangled photons to orient measurement frames and determine CHSH values [1, 2, 60]. Stochastic gradient descent methods have been used for aligning measurement bases for BB84 QKD protocols [15, 43, 105]. Bayesian optimization algorithms have been used for control of filters and polarization controllers to maximize the indistinguishability of two photons [94]. This prior work motivated us to compare these algorithms in our experiment to maximize the CHSH parameter for photon pairs with varying entanglement.

The Nelder-Mead method, also known as the downhill simplex method, creates a four-vertex tetrahedral simplex in the 3D parameter space defined by the voltages on the first three piezoelectric actuators within Alice's polarization controller. It iteratively modifies the simplex vertex voltages until they converge on a setting that maximizes the CHSH parameter, S [98]. Since the CHSH parameter is maximized through the relative location of Alice's and Bob's projector when they share the singlet state, $|\Psi^-\rangle$, only one receiver's polarization controller needs to be varied. This algorithm has the advantage that it does not require knowledge of the function's derivative, which would require additional measurements and whose measured accuracy can be low when the system has significant noise. The Nelder-Mead algorithm used in our experiment and simulations is implemented using python's scipy library [99].

The stochastic gradient descent algorithm is an iterative method that moves through parameter space along randomized directions using gradient estimates along those directions. For our 3D

parameter space, having only one direction along which to evaluate the gradient saves four measurements compared to if the total derivative vector gradient were to be estimated. The method works by first selecting a random direction in 3D parameter space, $\boldsymbol{V}_{\text{rand}}$, and evaluating the symmetric derivative

$$\Delta S_n(\boldsymbol{V}_n) = \frac{S(\boldsymbol{V}_n + dV\boldsymbol{V}_{\text{rand}}) - S(\boldsymbol{V}_n - dV\boldsymbol{V}_{\text{rand}})}{2dV} \quad , \tag{4.23}$$

the next parameter point is then updated to

$$\boldsymbol{V}_{n+1} = \boldsymbol{V}_n + \lambda \cdot \Delta S_n(\boldsymbol{V}_n) \cdot \boldsymbol{V}_{\text{rand}} \quad . \tag{4.24}$$

The "hyper-parameters" λ and dV control how much to step in the direction of the gradient and how much to step in parameter space. For large values of λ, convergence can exhibit oscillations about the extrema while for small values of λ the algorithm converges slowly. If the value of dV is too small, the accuracy of the derivative estimate is susceptible to noise, while if the value of dV is too large, the symmetric difference estimate of the derivative becomes inaccurate. Finally, because the piezoelectric polarization controllers used in our experiment exhibit hysteresis, we wish for the voltage jumps to be as small as possible. The optimum values were determined through simulations and found to be $\lambda = 0.8$ and $dV = V_\pi/12$. Details on how these were determined are shown in the following section.

Bayesian optimization uses prior knowledge from measurements to build a probability distribution over possible functions to fit the measured data. Here, measurements are values of the CHSH parameter, with the variables being the voltages on Alice's polarization controller. The probability distribution of possible functions is generated through the use of a Gaussian process. Because there is a probability distribution over possible fitting functions it is possible to calculate a mean function and variances to indicate confidence regions. More details about how Bayesian

optimization works are given in the following section. Using the mean function and the variances, an acquisition function then picks the next point in parameter space, weighing areas of parameter space that are not sampled (exploration) and areas where the mean function is estimated to be maximal (exploitation) with some built-in exploration vs exploitation trade-off setting established. When exploitation is preferred, the acquisition function picks points where the mean function is maximal with less regard to the variance caused by unsampled parameter space locations, but if exploration is preferred, the acquisition function's next point is skewed to unsampled parameter space. Both the Gaussian process covariance kernels and acquisition functions have different functional forms and associated hyper-parameters that come with them. For a full mathematical description of Gaussian process Bayesian optimization and its application to optimizing photon indistinguishability see the recent work of Cortes *et al* [94]. We implement Bayesian optimization through the use of the python package bayes_opt [120] for its ease of implementation. Due to hysteresis in our polarization controllers, we chose hyper-parameters that are biased towards nearby parameter space exploitation rather than exploring non-sampled parameter space because introducing large exploratory jumps cause errors within the optimization process. The acquisition function that we chose was the upper confidence bound with hyperparameter κ=0.4 and Gaussian process kernel hyperparameter α=10^{-8} for their ability to find the minimum condition the fastest and without introducing a large exploratory behavior the optimization procedure.

We used these methods to analyze experiments with various amounts of entanglement to determine how well they perform relative to each other. For ten different delay values, τ, we determined the maximum CHSH parameter each method attained relative to equation (4.9). At each τ value we performed ten alignment procedures to maximize the CHSH parameter for each method: Nelder-Mead, Bayesian optimization, and stochastic gradient descent. For each given alignment, we randomly assign each piezoelectric actuator in Bob's polarization controller a

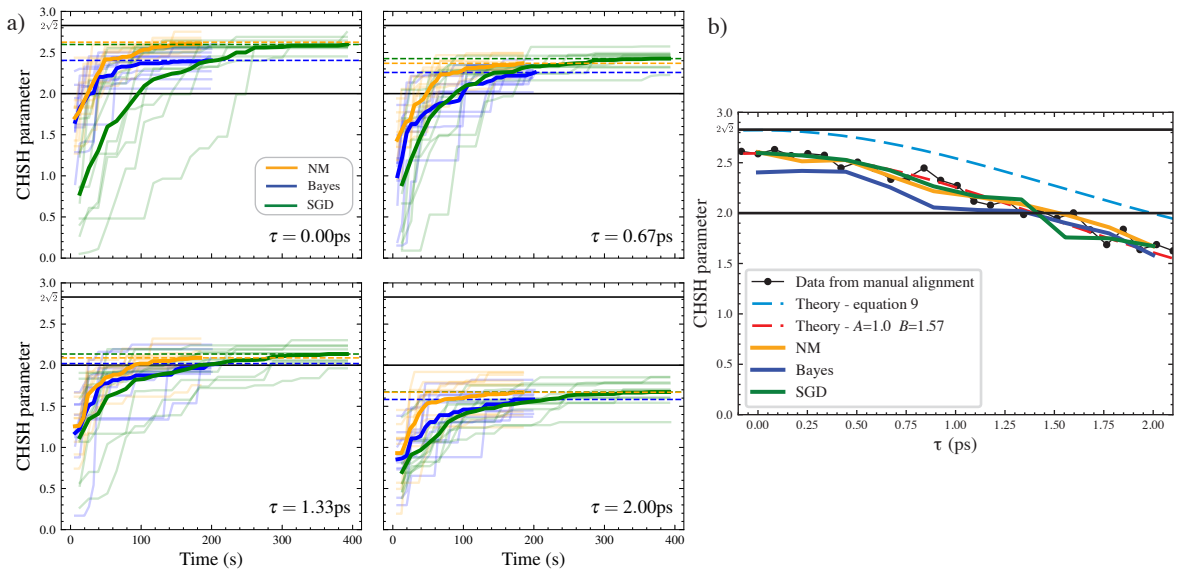

Figure 34: (a) Experimental data comparing the Nelder-Mead (orange), Bayesian optimization (blue), and stochastic gradient descent (green) methods for maximizing the CHSH parameter. In the top left, τ=0, Alice and Bob share the approximately maximally entangled singlet state. For increasing values of τ the entanglement shared by Alice's and Bob's photons decrease and also their ability to violate Bell's inequality. Light lines represent the individual alignment runs and bold lines are the statistical average of the 10 runs. Each measurement of S was based on an integration time of five seconds. The dotted lines show the final averaged S values the optimization algorithms converged to. (b) The average final convergence S value from each optimization method as a function of the relative delay within the entanglement interferometer.

value in $[0,V_\pi]$ to randomize the location of his projectors, $\boldsymbol{b}_{1,2}$, relative to Alice's projectors $\boldsymbol{a}_{1,2}$. Alice's initial polarization controller is set to the middle of her parameter space $\boldsymbol{V}_0$= $[V_\pi/2,V_\pi/2,V_\pi/2]$ so that going outside the bounds ($V<0$ and $V>V_\pi$) rarely occurs within the algorithm. When this does happen, the control code converts the voltage values used by the algorithm to be in the range $[0,V_\pi]$ by modulo V_π ,which may introduce hysteresis effects if frequent jumps across this boundary occur. Note, reset-free actuation is possible, but was not implemented here [27].

Several results using different values of τ can be seen in Figure 34a, where each faint orange, blue, and green line represent one of the ten runs for the Nelder-Mead, Bayesian optimization, and stochastic gradient descent algorithms, respectively. For all three algorithms, the best vertex

found up to that point is plotted since not every sampled parameter space point yields a better CHSH value, as can be seen from the Nelder-Mead example shown in figure 33. The bold lines are the averaged convergence behavior across the 10 runs on their historical staircasing ascent.

The first observation one can make is that the Nelder-Mead and Bayesian optimization, in general, start with a higher CHSH value than the stochastic gradient descent. This is because they initially sample four points around and including $\boldsymbol{V}_0$ and each point may generate up to four CHSH values depending on where the minus sign is located within (4.1). This amounts to changing one of the four projectors to its orthogonal counterpart, as an example $\boldsymbol{a}_2 \rightarrow -\boldsymbol{a}_2$. After this initial sampling, both the Nelder-Mead and Bayesian optimization algorithms then maximized the CHSH parameter that was highest. When $\tau=0$, both the Nelder-Mead and Bayesian optimization algorithms typically found states where $S>2$ (i.e., greater than the classical limit) in the first four measurements. This shows the effectiveness of random measurements that have been demonstrated for pairs of qubits, N qubits, and also higher dimensional quantum states [121, 122]. This is in contrast to the stochastic gradient descent algorithm that must pick one of the four CHSH measures to maximize at the beginning and, therefore, does not get the potential initial boost from reducing parameter space by picking one of the four CHSH parameters that are maximal near the initial starting condition.

Another observation is that the stochastic gradient descent takes about twice as long to reach a steady state value. This is because each of these algorithms takes roughly the same number of iterations to converge to a maximum ($\approx$30 iterations), but the gradient calculation requires two evaluations at each iteration. The stochastic gradient descent and Nelder-Mead algorithms both perform nearly identically when considering the final values they converge to. The Bayesian optimization appears to perform the worst in finding the true maximum, which we attribute to the hysteresis effects of the polarization controllers and the large jumps the Bayesian optimization

algorithm performs to sample unknown regions of parameter space. This happens even when the acquisition function is still weighted for exploitation rather than exploration. After returning from sampling a distant region of parameter space the polarization settings that were giving near optimal CHSH parameter values are now slightly altered, but all past priors do not take this into account. Since gradient-based and also simplex-based algorithms do not have this changing parameter space memory problem, they are not as affected by hysteresis.

The final CHSH value to which the methods converged is plotted versus the temporal mismatch τ in figure 34b. The Nelder-Mead and stochastic gradient descent perform nearly identically and reproduce the results from the optimal configuration shown in figure 31 with Bayesian optimization performing slightly worse. All of the optimization methods can detect a Bell violation up for $\tau<1.3$ picoseconds. The density matrix with this τ, using the quantum state tomography measurements from section 2, has the concurrence of ≈ 0.42 which means the photons are still entangled, but the entanglement can no longer be detected by Bell's inequalities.

4.6 Hyperparameters for Bayesian optimization and stochastic gradient descent

These optimization methods all have adjustable parameters called "hyper-parameters", that can be used to tune the performance of the algorithm. Because of the time needed to carry out experimental measurements, it is challenging to experimentally determine the optimal settings. Therefore, we developed a numerical simulation of the actuator and alignment method. To simulate our experiment we use equation (4.1) where $\boldsymbol{a}_i$ and $\boldsymbol{b}_j$ for $i,j\in\{1,2\}$ are initially randomly distributed to simulate the fiber's birefringence with the condition $\boldsymbol{a}_1\cdot\boldsymbol{a}_2=0$ and likewise $\boldsymbol{b}_1\cdot\boldsymbol{b}_2=0$. Alice's polarization controller then rotates her projectors to new states

$$\boldsymbol{a}_i'=\boldsymbol{R}_{PC}(\theta_1,\theta_2,\theta_3)\boldsymbol{a}_i=\boldsymbol{R}(\hat{s}_1,\theta_3)\boldsymbol{R}(\hat{s}_2,\theta_2)\boldsymbol{R}(\hat{s}_1,\theta_1)\boldsymbol{a}_i \tag{4.25}$$

with $\boldsymbol{R}(\boldsymbol{r},\theta)=(\boldsymbol{r}\boldsymbol{r}\cdot)+\sin\theta(\boldsymbol{r}\times)-\cos\theta(\boldsymbol{r}\times\boldsymbol{r}\times)$, where $\boldsymbol{r}$ is the rotation vector around which the polarization projection directions rotates by angle θ. We use the iterative algorithms discussed earlier to adjust the three angles, with the goal of maximizing S to the ideal value of $2\sqrt{2}$.

4.6.1 Bayesian Optimization

For an introduction to Bayesian optimization and application of Bayesian optimization to the task of engineering photon indistinguishability see the textbook *Bayesian Optimization* by Roman Garnett [112] and the paper of Cortes *et al* [94]. Bayesian optimization attempts to find the maximum of an objective function $\phi(\boldsymbol{x})$, where the variable $\boldsymbol{x}\in\mathbb{R}^D$ and D is the dimension size of the input variables. Here, our objective function is the CHSH parameter, and the variable is $\boldsymbol{\theta}=(\theta_1,\theta_2,\theta_3)\in\mathbb{R}^3$. In pursuit of this goal, the Bayesian optimization incrementally builds a probabilistic model of our objective function which reflects the current knowledge of it from prior measurements. The probabilistic model is generated via a Gaussian process (GP). A GP generates a probabilistic distribution of functions over the domain:

$$\mathrm{p}(f,\mathcal{D})=\mathcal{GP}\Big(f;\mu,K\Big) \tag{4.26}$$

where μ is a mean function, K is a positive semidefinite covariance function (or kernel) and $\mathcal{D}$ is the total sampled data defined as $\mathcal{D}=(y,X)$. The quantities within the sampled data $\mathcal{D}$ are samples of the objective function $y=\{y_1,y_2,...,y_n\}$, using the input parameters $X=\{\boldsymbol{x}_1,\boldsymbol{x}_2,...,\boldsymbol{x}_n\}$. The mean function $\mu(\boldsymbol{x})$ is the average value over all functions in the distribution for all points $\boldsymbol{x}$ within the parameter space. The covariance function determines how deviations from the mean are structured, encoding expected properties of the function's behavior. Intuitively one can think of a GP as analogous to a function, but instead of returning a scalar $f(\boldsymbol{x})$ for an arbitrary $\boldsymbol{x}$, it returns the mean and variance of a normal distribution over the possible values of f at $\boldsymbol{x}$. Importantly, the

mean function and knowledge of the variance can be used within the acquisition function, defined below, to determine the point in parameter space to sample next.

Common kernels are the squared exponential covariance kernel

$$K(\boldsymbol{x},\boldsymbol{x}')=\exp\Big(-\frac{||\boldsymbol{x}-\boldsymbol{x}'||^2}{2\alpha^2}\Big) \tag{4.27}$$

with α being a hyperparameter length scale which ensures nearby points have similar function values and the Matern kernel,

$$K(\boldsymbol{x},\boldsymbol{x}')=\frac{1}{\Gamma(\nu)2^{\nu-1}}\Big(\frac{\sqrt{2\nu}}{\alpha}||\boldsymbol{x}-\boldsymbol{x}'||^2\Big)^{\nu}\mathcal{K}_{\nu}(\frac{\sqrt{2\nu}}{\alpha}||\boldsymbol{x}-\boldsymbol{x}'||^2) \tag{4.28}$$

with Γ being the Gamma function, $\mathcal{K}_{\nu}$ the modified Bessel function, and ν a hyperparameter that controls the smoothness of the function. The GP is updated using Bayesian inference via Bayes' theorem, where new measurements of the objective function change the probabilistic model to fit the data better. Bayes' theorem, at a simple level, can be stated as the posterior probability of a model M given data $\mathcal{D}$ is proportional to the likelihood of $\mathcal{D}$ given M multiplied by the prior probability of M

$$\mathrm{p}(M|\mathcal{D})\propto\mathrm{p}(\mathcal{D}|M)\mathrm{p}(M) \quad . \tag{4.29}$$

To sample efficiently, Bayesian optimization uses an acquisition function on the GP (after a new measurement) and the acquisition function generates the best point to sample the objective function next. Like GP kernels, many acquisition functions exist, such as the probability of improvement, expected improvement, and upper confidence bound (UCB). An optimization of the acquisition function over all possible points within the parameter space determines the next

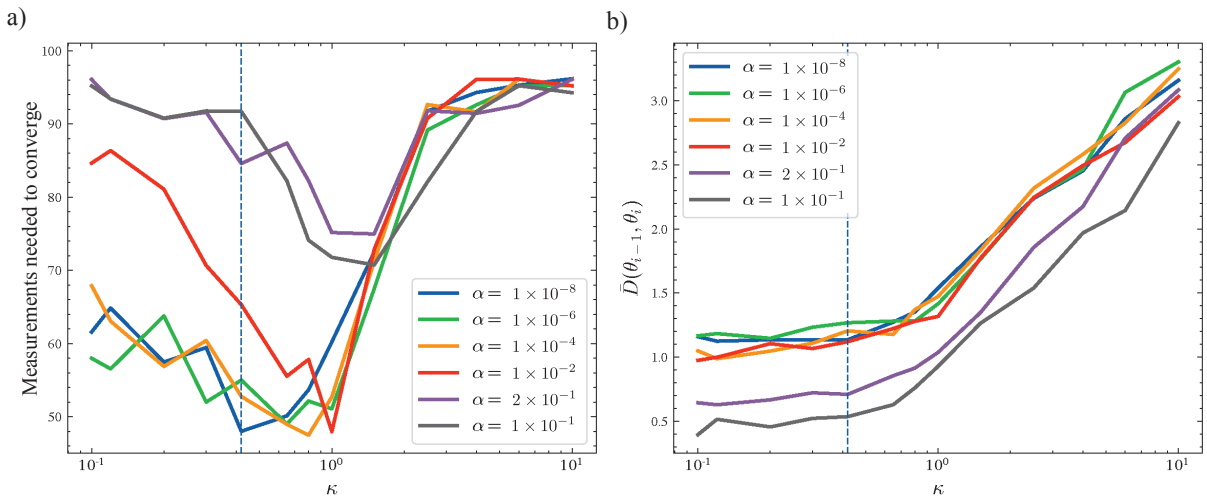

Figure 35: Simulated experiments performing Bayesian optimization with various hyperparameters to maximize the CHSH parameter. a) Number of measurements needed for the Bayes optimization to converge S to 99% of $2\sqrt{2}$ versus the hyperparameter κ used within the upper confidence bound acquisition function. Plotted are various values of the hyperparameter α used within the Matern covariance kernel of the Gaussian process. b) Average distance over the course of CHSH parameter maximization in $\boldsymbol{\theta}$ parameter space between successive points picked by the acquisition function.

sample point. As an example the UCB acquisition function is

$$a_{\text{UCB}}=\mu(\boldsymbol{x})+\kappa\sigma(\boldsymbol{x}) \quad . \tag{4.30}$$

When the hyperparameter κ is large, the acquisition function will be maximal in locations where the uncertainty, σ, is large, giving exploratory behaviors to the optimization process. When κ is small the acquisition function will be maximal in locations closer to the maximal of the mean function.

An extensive examination of different Bayesian kernels and acquisition functions, as done in Cortes' work, was not done here and remains a project for future investigation. Instead, we used Cortes' findings that the Matern kernel is the optimal kernel with $\nu{=}5/2$ and the upper confidence bound acquisition function being the optimal acquisition function. Since Cortes was also concerned with photon polarization, along with temporal alignment and spectral filtering for

photon indistinguishability, this assumption seems to be a good starting point. We numerically simulated various size hyperparameters, α within the Matern kernel and κ values within the upper confidence bound acquisition function, to determine what parameters would be best to implement within our experiment. We used the bayes_opt python package which builds upon the sklearn library. Since we are concerned with the speed of convergence to the maximal CHSH parameter value, we average over 100 simulated alignments to determine how many measurements of S are needed before the Bayesian optimization routine finds a condition where the sampled S is within 1% of $2\sqrt{2}$. The plot of this is seen in figure 35a. In general, a smaller length scale with $\alpha{=}10^{-8}$ and $\kappa{=}0.4$, shown as a dotted line, performed best and was determined as the best points to implement within our experiment.

Additionally, we want to reduce the distance between consecutive points chosen by the acquisition function due to hysteresis within our polarization controllers. While we did not seek to numerically model the effect of hysteresis, our numerical models do allow us to estimate the average parameter step-size, and to evaluate how this depends on the hyper-parameter settings. The distance between parameter points $\boldsymbol{\theta}_i$ and $\boldsymbol{\theta}_{i+1}$ is the Euclidean distance $||\theta_{i+1}{-}\theta_i||$. After a given alignment run with N samples, we can get an overall average distance between all consecutive samples

$$D(\boldsymbol{\theta}_{i-1},\boldsymbol{\theta}_i){=}\frac{1}{N{-}1}\sum_{i}^{N-1}||\boldsymbol{\theta}_{i+1}{-}\boldsymbol{\theta}_i|| \quad . \tag{4.31}$$

A plot of this distance averaged over the 100 simulated alignments for each value of κ and α are shown in figure 35b. The $\alpha{=}10^{-8}$ and $\kappa{=}0.4$ parameters chosen also perform well in minimizing this distance.

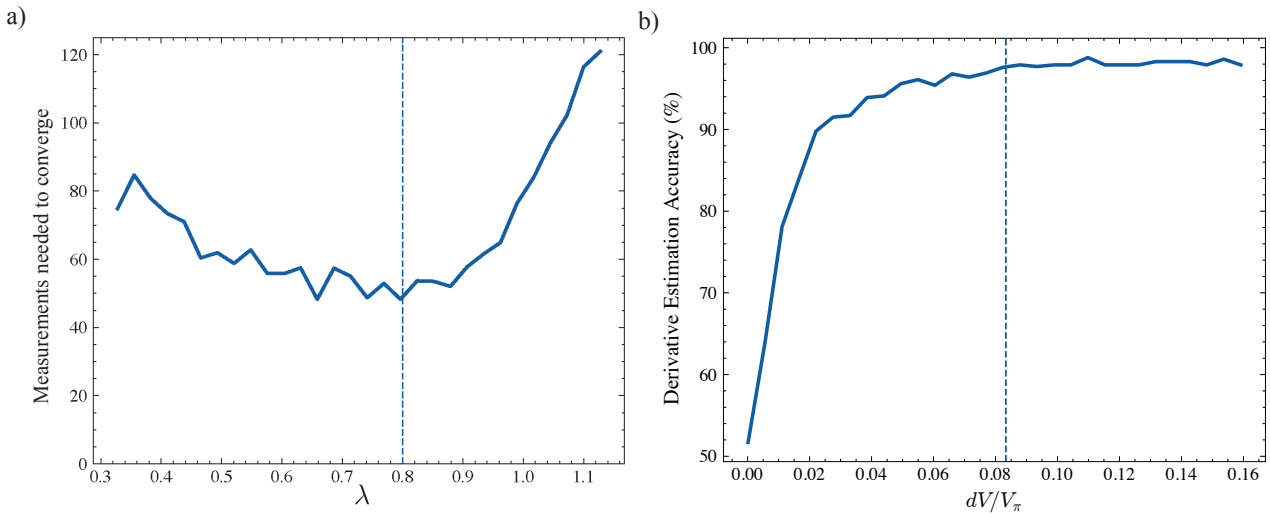

Figure 36: a) Number of measurements needed for the stochastic gradient descent method to converge S to 99% of $2\sqrt{2}$ versus the hyperparameter λ, which determines how much to step in the direction of the gradient. b) In the presence of background counts and Poissonian statistics the estimation of the derivative of S from equation (4.23) needs a large enough step in parameter space to overcome the noise from accidental coincidence counts, but cannot be so large as to introduce errors and bring hysteresis effects into play. With r_s=400 pairs per second, r_b=80 pairs per second, and an integration time T=5 seconds we get an optimal $dV=V_\pi/12$.

4.6.2 Stochastic Gradient Descent

For the stochastic gradient descent, the size of the steps in the direction of the gradient, λ, and the parameter space step size to determine the gradient, dV, are hyperparameters. To find the optimal value of λ within equation (4.24), sometimes referred to as the learning parameter, we ran 200 simulated alignments maximizing equation (4.1) for 30 values of λ ranging from 0.3 to 1.1. Because we are interested in choosing a setting that maximizes the value of S, we set the stopping condition at 99% of the optimal value $2\sqrt{2}$. The number of measurements needed for Alice's polarization controller to reach this threshold average over the 200 runs is shown in figure 36a. The dotted line corresponds to λ=0.8, which performed the best at finding the true maximum with the fewest number of measurements at 50. With gradient estimates taking two measurements, this amounts to roughly 25 iterations of the stochastic gradient descent method, which is what was observed experimentally in figure 34a.

To determine the parameter step needed for accurate estimation of the symmetric derivative, equation (4.23), we model the coincidence count rate between any two projectors, i for Alice and j for Bob, based on Poisson statistics with signal rate, r_s, and probability of detection $\mathrm{Tr}(\hat{\rho}\hat{A}_i\otimes\hat{B}_j)$, a constant background coincidence count rate, r_b, and integration time T [1]. Taken together, the number of coincidences, N, measured in an integration interval, T, can be modeled by a discrete Poisson distribution with a mean that depends on Alice's rotational angles θ_1,θ_2,θ_3 from her polarization controller

$$\begin{aligned} \mathrm{N}(\boldsymbol{a}_i,\boldsymbol{b}_j)_{N=k} &= \frac{(r_{i,j}(\theta_1,\theta_2,\theta_3)T)^k}{k!}e^{-r_{i,j}(\theta_1,\theta_2,\theta_3)T} \\ r_{i,j}(\theta_1,\theta_2,\theta_3) &= r_s\mathrm{Tr}(\hat{\rho}\hat{A}_i(\theta_1,\theta_2,\theta_3)\otimes\hat{B}_j)+r_b \\ \hat{A}_i(\theta_1,\theta_2,\theta_3) &= \boldsymbol{R}_{PC}(\theta_1,\theta_2,\theta_3)\boldsymbol{a}_i\cdot\boldsymbol{\sigma} \end{aligned} \quad . \tag{4.32}$$

In our experiment, we are concerned with taking a large enough step so that the noise from the background counts does not impair the accuracy of the symmetric derivative (4.23). In the time multiplexed set up we observe a maximal count with coaligned measurement bases of r_s=400 pairs/sec and a background accidental coincidence count r_b=80 pairs/sec. We use an integration time of T=5 seconds. The simulated coincidence probability of a photon from Alice's i^{th} projector and Bob's j^{th} projector is then

$$P_{i,j} = \frac{\mathrm{N}(\boldsymbol{a}_i,\boldsymbol{b}_j)}{\mathrm{N}(\boldsymbol{a}_i,\boldsymbol{b}_j)+\mathrm{N}(\boldsymbol{a}_i,-\boldsymbol{b}_j)+\mathrm{N}(-\boldsymbol{a}_i,\boldsymbol{b}_j)+\mathrm{N}(-\boldsymbol{a}_i,-\boldsymbol{b}_j)} \tag{4.33}$$

The accuracy of the symmetric derivative is determined from the percent overlap of the derivative with and without background accidentals (r_b=0) shown in figure 36b. With the observed rates we determined $dV=V_\pi/12$, shown as the dotted line, performed optimally while being small enough that hysteresis effects from the voltage jumps were not as impactful.

4.7 Conclusion

Rather than performing measurement intensive quantum state tomography to estimate the entanglement quality, proving the violation of a Bell's inequality is a much easier experimental task. Evaluation of the CHSH parameter can give a quantitative measure of the concurrence or entanglement quality of the entangled systems. This still requires the careful alignment of two parties' measurement bases which is difficult in a fiber optic environment. In this paper, we have experimentally demonstrated the ability to find the optimal configuration of Alice's polarization controller when Alice and Bob share entangled photon pairs that maximize the violation of Bell's inequality in the presence of uncontrolled birefringent fiber spans. We investigated several iterative optimization methods that have been used within the quantum communication literature — namely, Nelder-Mead optimization, stochastic gradient descent, and Bayesian optimization— for their ability to maximize the CHSH parameter. These methods were tested using various levels of entanglement shared between the photons sent to Alice and Bob. All three methods were able to violate Bell's inequality for a temporal mismatch in our entangling interferometer of $\tau < 1.3$ picoseconds, corresponding to an entanglement concurrence value of 0.42. The Nelder-Mead and Bayesian optimization found the optimum condition the quickest, while the Nelder-Mead and stochastic gradient descent were the most accurate in finding the optimum value.

Our experiment used a polarization and time multiplexed detection system that reduces the experimental demands on photon detection instruments. Using half the number of detectors allows off-the-shelf coincidence counting electronic boards to process the 16 signals in a signal measurement, without alternating between measurement settings. This allows real-time measurements of two pairs of projection bases to be used as feedback for upstream polarization controllers. Additionally, this time-multiplexed detection system is more robust to polarization controller

hysteresis problems, where jumping between two nonorthogonal polarization projection bases introduces measurement errors. This setup and evaluation methods may prove useful for the entanglement quantification of distributed entangled particles in future quantum networks where no alignment pilot tones are used and only feedback signals from the entangled particles are leveraged.

Chapter 5

Conclusion

> Whereas digital computing was the definitive technology of the twentieth century, quantum technologies will be for the 21st.
>
> Peter R. Rohde

5.1 Findings summarized

In conclusion, this dissertation has examined the use of measuring polarization entangled photons as a tool for correcting polarization drift and estimating the amount of entanglement through the violation of a Bell's inequality through automated optimization methods. When this dissertation project was developed in early 2020, no experiment had yet been performed to examine the use of distributed measurements on entangled particles to correct for polarization drift between two individuals or the maximization of the CHSH parameter. Several groups had begun to examine the use of single photons from attenuated lasers conducting BB84 QKD to align the measurement frames of the sender and receiver [31, 41], but the extension to two measurement bases sharing an entangled quantum source, like the diagram shown in figure 9, had yet to be thoroughly investigated. Before our publication, Shi *et al* [43] first studied this problem in a deployed network, but left details to be examined more closely. Within our work [1] we showed polarization drift correction is possible within a 7.1 km deployed fiber loop between the University of Maryland and the Laboratory for Telecommunication Sciences. We explored how different

signal-to-accidental coincidence count rates and integration times impacted the ability of the measurement frames to align using the Nelder-Mead simplex optimization method. We also probed how quickly our method could correct polarization drifts and showed in an experiment with low coincidence count rates that it was able to keep up with a controlled polarization drift rate of 0.25° per integration period.

After showing we could align one pair of measurement projection bases using entangled photons, we looked for ways how to perform complete polarization frame alignment by orienting two measurement projection directions in parallel. This required the development of a new polarization and time multiplexed detection setup to reduce the demands on the real-time coincidence counting electronics. This polarization and time multiplexed detection setup allowed us to reduce the number of detectors from eight to four and all sixteen coincidence counts from Alice's and Bob's two measurement bases can be pieced out from the interarrival time using only four real-time start-stop based coincidence counting processors. With this setup, we showed that total measurement frame alignment was possible and that we could also orient Alice's and Bob's projection bases in an interleaved fashion, to maximize the CHSH parameter. When this parameter is found to be greater than two, it is a valid measure of entanglement for our two-particle source. We explored the ability of three numerical algorithms: Bayesian optimization, Nelder-Mead simplex optimization, and stochastic gradient descent to find CHSH parameters that violated Bell's inequality for differing values of entanglement. These methods have all been used to control the polarization of photons within the quantum optics literature, but this is the first study to examine how well they do with respect to each other. The amount of entanglement was controlled by the relative temporal delay of the arrival of one photon at an entangling 50/50 beamsplitter with respect to the other. We found the Nelder-Mead simplex method worked the best out of the three in terms of its ability to find the maximum CHSH parameter the quickest without being affected by the hysteresis of our

polarization controller like the Bayesian optimization method.

5.2 Future work

For future plans, we intend to continue studying the ability to use quantum signals for alignment and calibration within quantum networks. Within this section, I will outline a few projects that we have already started working on to address the next iteration of polarization measurement base alignment using quantum signals.

We plan on studying how polarization dependent loss and polarization mode dispersion can affect entanglement measures and, in general, how it affects the coincidence counting from the polarization and time multiplexed setup we engineered when the polarizations of the photons impinging on the superconducting nanowire detectors give different polarization dependent detection efficiencies for each photon. This is in contrast to the experiments reported in this dissertation where the quantum efficiencies were equalized to reduce the impact of polarization dependent loss. We plan on implementing our full polarization measurement frame alignment procedure within our LTS and UMD fiber loop, as well as investigating whether this method can work within portions of the DC-Qnet. We plan on investigating pulsed sources, rather than continuous wave sources that we have used up until now. This also opens new investigations into how these pulsed signals can perform polarization control and aid in timing synchronization. It is also interesting to theoretically speculate if extensions to higher-order singlet states (4+ qubits) can offer interesting alignment strategies for star networks rather than daisy-chaining the alignment for every node within the quantum network. However, using our method of measurement frame alignment, if one node was deemed the chosen reference frame then all other nodes sharing the $|\Psi^-\rangle$ with that frame can align to it in parallel. In addition to studying other numerical algorithms for polarization control, we are also interested in using calibrated transforms to speed up the

polarization drift correction process. Since iterative alignment techniques take 20-40 iterations to find the optimal configuration and with integration times taking several seconds, the total time taking measurements is a bottleneck to correcting for polarization drifts. Using new polarization controllers, we are looking to implement controlled polarization reversal transformations, shown in the next section, that should reduce the number of measurements by an order of magnitude [38, 39].

5.2.1 Reversal Operator from Quantum Signals

Chapters 3 and 4 dealt with aligning the polarization to some configuration based off the iterative maximization or minimization of a signal, whether that be coincidence counts or the CHSH parameter. This allows us to ignore the underlying physical model of the polarization controller and use its settings as variables for iterative algorithms like the Nelder-Mead simplex optimization in chapters 3 and 4, or Bayesian optimization and stochastic gradient descent in chapters 4. This was necessary as the configuration of the rotational vectors for each piezoelectric actuator does not align to the optimal conditions $\boldsymbol{n}_1{=}\boldsymbol{n}_3$ and $\boldsymbol{n}_2{=}\boldsymbol{n}_4$, due to nonnull birefringence values when the voltage across each were zero, as described in section 2.1. While arbitrary any-to-any polarization transformation can be done with three actuators whose rotational vectors aren't aligned, the solutions for the correct voltage must be numerically solved using a nonlinear solver. To make matters worse, if the rotational vectors change with respect to each other due to hysteresis effects, then frequent calibration to find their new locations is needed.

Instead of using piezoelectric actuators as polarization controllers, other fixed-axis, variable birefringence devices exist, such as liquid crystals or electrooptic controllers. Because these devices operate in free space, the coupling in and out of singlemode fiber inherently generates more loss (along with losses due to the polarization controller) than the actuator based polarization

controller where the light stays within the guiding medium. Our lab has just acquired a Boston Applied Technologies' (BATi) polarization controller using electrooptic ceramic materials where the birefringence of each ceramic is proportional to the voltage squared, $\delta \propto V^2$. This system is compact, fiber-coupled, high speed with response times under 30μs and relatively low loss with an insertion loss of $\approx$1.0 dB. Unlike our piezoelectric actuator-based polarization controllers, these have virtually zero hysteresis. With relatively low loss and high repeatability, this makes them ideal candidates for polarization controllers within our quantum experiments that use calibrated transformations to convert from one polarization state to another through analytic formulas rather than iterative strategies.

An example of one analytical formula is shown in figure 37. To transform the initial state $\boldsymbol{S}_0=(S_1,S_2,S_3)$ into $\boldsymbol{S}_f=(S_{f,1},S_{f,2},S_{f,3})$ can be done with three birefringent elements with rotation vectors $\boldsymbol{n}_1=\boldsymbol{n}_3$ and $\boldsymbol{n}_1\cdot\boldsymbol{n}_2=0$. For simplicity we can assume $\boldsymbol{n}_1=\boldsymbol{n}_3=\hat{s}_1$ and $\boldsymbol{n}_2=\hat{s}_2$, but if this wasn't the case we could rotate into the polarization controller's frame by rotation operator $\boldsymbol{R}$ where $\boldsymbol{n}_1$ now equals $\hat{s}_1$ and $\boldsymbol{n}_2=\hat{s}_2$ and then transform the polarization state $\boldsymbol{S}'_0=\boldsymbol{R}\boldsymbol{S}_0$ to $\boldsymbol{S}'_f=\boldsymbol{R}\boldsymbol{S}_f$. The first birefringent element rotates the polarization until the state is within the $\hat{s}_1/\hat{s}_3$ plane, shown in figure 37a. This is accomplished for birefringence

$$\tan\delta_1=\frac{S_2}{S_3} \quad \longrightarrow \quad \delta_1=\arctan\frac{S_2}{S_3} \quad . \tag{5.1}$$

The initial polarization is now in the polarization state

$$\boldsymbol{S}_{\delta_1}=\begin{pmatrix} S_1 \\ 0 \\ S_2\sin\delta_1+S_3\cos\delta_1 \end{pmatrix}=\begin{pmatrix} S_1 \\ 0 \\ S'_3 \end{pmatrix} \quad .$$

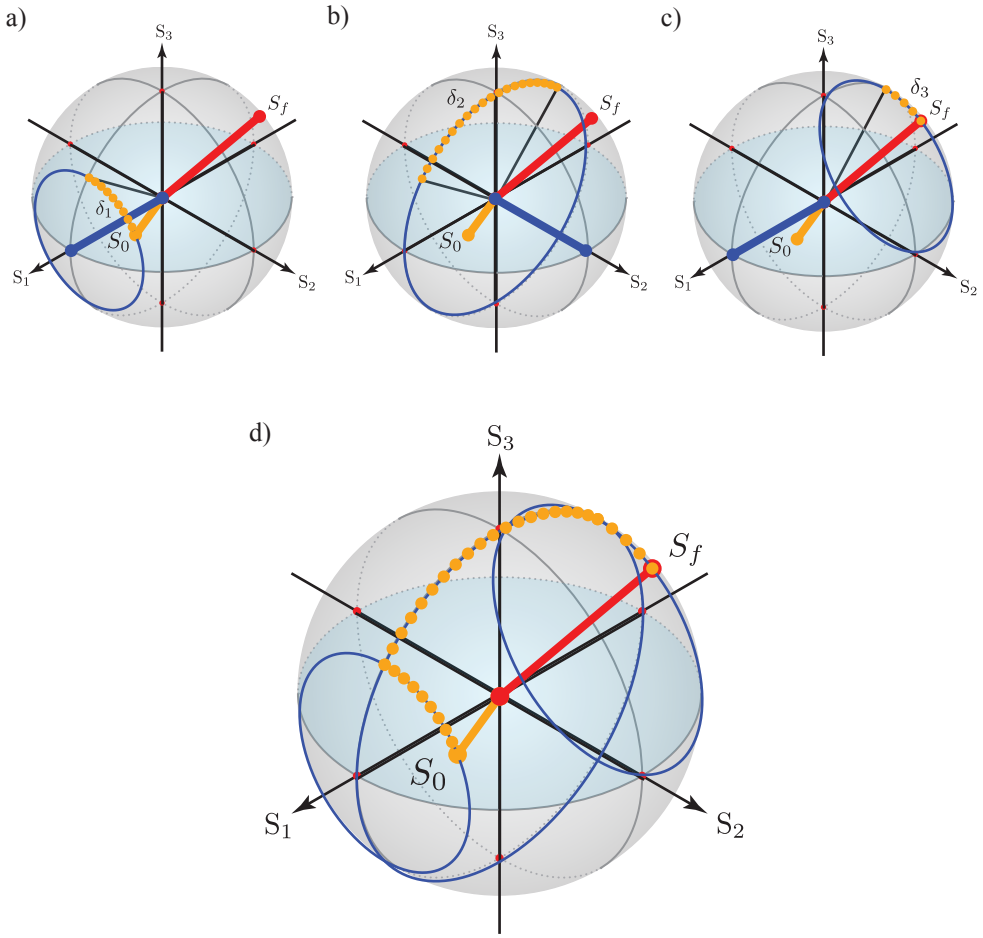

Figure 37: Reversal operator for calibrated polarization controller to convert $\boldsymbol{S}_0$ in orange to $\boldsymbol{S}_f$ in red. (a) The birefringence δ_1 moves $\boldsymbol{S}_0$ to the $\hat{s}_1/\hat{s}_3$ plane by rotation about the rotational vector $\hat{s}_1$ shown in blue. (b) The birefringence δ_2 moves $\boldsymbol{S}_0$ until the $\hat{s}_1$ components from $\boldsymbol{S}_0$ and $\boldsymbol{S}_f$ are equal by rotation about the rotational vector $\hat{s}_2$ shown in blue. (c) Final birefringence δ_3 to equalize $\boldsymbol{S}_0$ and $\boldsymbol{S}_f$ by rotation about the rotational vector $\hat{s}_1$ shown in blue. (d) Total rotational transform.

The second birefringent element rotates the polarization until the component in the $\hat{s}_1$ equals $S_{f,1}$ and is shown in figure 37b. This is accomplished for birefringence δ_2

$$S_x \cos\delta_2 + S_3' \sin\delta_2 = S_{f,1} \quad . \tag{5.2}$$

An algebraic equation can be calculated when $S_3' \neq 0$

$$\delta_2 = \arcsin \frac{S_{f,1}}{\sqrt{S_1^2 + {S_3'}^2}} - \arctan \frac{S_1}{S_3'} \tag{5.3}$$

which will leave the polarization in the state

$$\vec{S}'' = \begin{pmatrix} S_{f,1} \\ 0 \\ -\sin\delta_2 S_1 + \cos\delta_2 S_3' \end{pmatrix} = \begin{pmatrix} S_{f,1} \\ 0 \\ S_3'' \end{pmatrix} \quad .$$

The third birefringent element rotates the polarization until the components in the $\hat{s}_{2,3}$ equals $S_{f,2-3}$, and is shown in figure 37c. This is accomplished for

$$\delta_3 = \arctan_2 \frac{-S_{f,2}}{S_{f,3}} \quad . \tag{5.4}$$

The total rotational transform, figure 37d, that moves the polarization from state $\boldsymbol{S}_0$ to $\boldsymbol{S}_f$ is

$$\begin{aligned} \boldsymbol{R}_{\text{tot}} &= \boldsymbol{R}_3(\hat{s}_1, \delta_3) \boldsymbol{R}_2(\hat{s}_2, \delta_2) \boldsymbol{R}_1(\hat{s}_1, \delta_1) \\ \delta_1 &= \arctan \frac{S_2}{S_3} \\ \delta_2 &= \arcsin \frac{S_{f,1}}{\sqrt{S_1^2 + (S_2 \sin\delta_1 + S_3 \cos\delta_1)^2}} - \arctan \frac{S_1}{S_2 \sin\delta_1 + S_3 \cos\delta_1} \\ \delta_3 &= \arctan \frac{-S_{f,2}}{S_{f,3}} \quad . \end{aligned} \tag{5.5}$$

Using this strategy two orthogonal polarization directions, $\boldsymbol{S}_1=(S_{11},S_{12},S_{13})$ and $\boldsymbol{S}_2=(S_{21},S_{22},S_{23})$ can be aligned in a single step to the rotational angles, $\boldsymbol{n}_1=\hat{s}_1$ and $\boldsymbol{n}_2=\hat{s}_2$ by the rotational angles

$$\begin{aligned}
\delta_1&=\arctan\frac{S_{11}}{S_{12}}\\
\delta_2&=\arcsin\frac{1}{\sqrt{S_{11}^2+(S_{12}\sin\delta_1+S_{13}\cos\delta_1)^2}}-\arctan\frac{S_{11}}{S_{12}\sin\delta_1+S_{13}\cos\delta_1}\\
\delta_3&=\arctan\frac{-S_{22}}{S_{23}} \quad .
\end{aligned} \tag{5.6}$$

If Alice and Bob each have two measurement projection directions $\boldsymbol{a}_{1,2}$ and $\boldsymbol{b}_{1,2}$ and if they need them to be coaligned, Alice can do so using five birefringent elements that are oriented in the configuration $\boldsymbol{n}_1=\boldsymbol{n}_3=\boldsymbol{n}_5=\hat{s}_1$ and $\boldsymbol{n}_2=\boldsymbol{n}_4=\hat{s}_2$. The idea is that Alice's first three elements rotate her projection directions $\boldsymbol{a}_{1,2}$ to $\hat{s}_{1,2}$ and then the last three perform the inverse rotation that would convert Bob's projection directions $\boldsymbol{b}_{1,2}$ to $\hat{s}_{1,2}$. If $(\delta_{a1},\delta_{a2},\delta_{a3})$ are the rotational angles that orient Alice's projection directions $\boldsymbol{a}_{1,2}$ to $\hat{s}_{1,2}$ and $(\delta_{b1},\delta_{b2},\delta_{b3})$ are the rotational angles that orient Bob's projection directions $\boldsymbol{b}_{1,2}$ to $\hat{s}_{1,2}$, from equations (5.6), then the rotational transform to orient $\boldsymbol{a}_{1,2}$ to $\boldsymbol{b}_{1,2}$ is

$$\begin{aligned}
\boldsymbol{R}(\delta_1,\delta_2,\delta_3,\delta_4,\delta_5)&=\boldsymbol{R}_5(\hat{s}_1,\delta_5)\boldsymbol{R}_4(\hat{s}_2,\delta_4))\boldsymbol{R}_3(\hat{s}_1,\delta_3)\boldsymbol{R}_2(\hat{s}_2,\delta_2)\boldsymbol{R}_1(\hat{s}_1,\delta_1)\\
&=[\boldsymbol{R}_b(\delta_{b1},\delta_{b2},\delta_{b3})]^{-1}\boldsymbol{R}_a(\delta_{a1},\delta_{a2},\delta_{a3})\\
&=\boldsymbol{R}_5(\hat{s}_1,-\delta_{b1})\boldsymbol{R}_4(\hat{s}_2,-\delta_{b2}))\boldsymbol{R}_3(\hat{s}_1,\delta_{a3}-\delta_{b3})\boldsymbol{R}_2(\hat{s}_2,\delta_{a2})\boldsymbol{R}_1(\hat{s}_1,\delta_{a1}) \quad .
\end{aligned} \tag{5.7}$$

To perform this operation using only signals from quantum measurements means one must deduce all three components of the projection Stokes' vector from the quantum signals. This is planned to be done using a similar approach to theoretical ideas proposed by Ramos *et al* [38, 39]. An experiment using single photons or entangled photons to preform calibrated reversal transforms to correct for polarization drifts has yet to be performed, which our group hopes to

be the first. The planned experimental setup for single and entangled photons is shown in figure 38. When Alice either emits single photons with polarization $\boldsymbol{a}_1$ or measures the entangled state $|\Psi^-\rangle=\frac{1}{\sqrt{2}}(|H_aV_b\rangle-|V_aH_b\rangle)$ with projector $\boldsymbol{a}_1$ then the probability of Bob measuring a photon with projector $\boldsymbol{b}_i$ (i=1,2) is

$$\begin{aligned} P_{\text{single}}(\boldsymbol{a}_1,\boldsymbol{b}_i)&=\frac{1}{2}\Big(1+\boldsymbol{a}_{1,\text{Bob}}\cdot\boldsymbol{b}_i\Big)=\frac{1}{2}\Big(1+(\boldsymbol{R}_b\boldsymbol{a}_1)\cdot\boldsymbol{b}_i\Big) \\ P_{\text{entangled}}(\boldsymbol{a}_1,\boldsymbol{b}_i)&=\frac{1}{4}\Big(1-\boldsymbol{a}_{1,\text{Bob}}\cdot\boldsymbol{b}_i\Big)=\frac{1}{4}\Big(1-(\boldsymbol{R}_b\boldsymbol{R}_a^{-1}\boldsymbol{a}_1)\cdot\boldsymbol{b}_i\Big) \end{aligned} \tag{5.8}$$

where $\boldsymbol{a}_{1,\text{Bob}}$ is Alice's projector as measured in Bob's measurement frame due to fiber rotation $\boldsymbol{R}$. The QBER is traditionally defined as $1-P$ for the single photon configuration and $2P$ for the entangled photon configuration. Bob, not knowing $\boldsymbol{a}_{1,\text{Bob}}$, can restrict the locus of Alice's projector to a circle on the Poincaré sphere, shown in figure 39. With two nonorthogonal measurement directions (H/V=$\boldsymbol{b}_1$ and D/A=$\boldsymbol{b}_2$) the intersection of those pin Alice's polarization to two points at locations

$$\boldsymbol{r}_\pm=\begin{pmatrix} \cos\theta_{11} \\ \cos\theta_{12} \\ \pm\sqrt{1-\cos^2\theta_{11}-\cos^2\theta_{12}} \end{pmatrix} \quad \text{with} \quad \begin{aligned} \theta_{1i}^{\text{single}}&=\arccos 1+2P_{\text{single}}(\boldsymbol{a}_1,\boldsymbol{b}_i) \\ \theta_{1i}^{\text{entangled}}&=\arccos 1-4P_{\text{entangled}}(\boldsymbol{a}_1,\boldsymbol{b}_i) \end{aligned} . \tag{5.9}$$

Bob chooses one of the two points randomly, say $\boldsymbol{r}_-$, and preforms reversal operator, $\boldsymbol{R}_{\text{PC},-}$, calculable from his calibrated polarization controller to orient $\boldsymbol{a}_{1,\text{Bob}}=\boldsymbol{R}_{\text{PC},-}\boldsymbol{R}\boldsymbol{a}_1$ to $\boldsymbol{b}_1$. If he chose incorrectly he preforms the rotation $\boldsymbol{R}_{\text{PC},+}\boldsymbol{R}_{\text{PC},-}^{-1}$ will orient $\boldsymbol{a}_{1,\text{Bob}}$ with $\boldsymbol{b}_1$. Double checking that this correctly aligns their measurement base $\boldsymbol{a}_1$ and $\boldsymbol{b}_1$ requires at most three measurements. This is roughly an order of magnitude faster than iterative algorithms that took 20-40 measurements for general polarization alignment. This strategy can easily be extended for all measurement frames $\boldsymbol{a}_{1,2}$ and $\boldsymbol{b}_{1,2}$ for complete polarization drift compensation through the

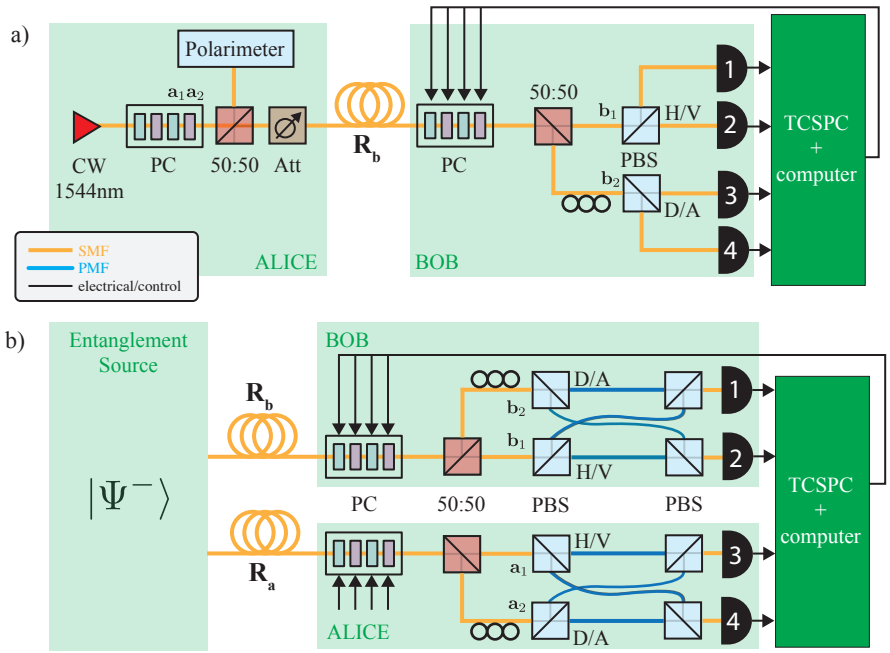

Figure 38: Experimental diagram for future work on reversal operator using single (a) and entangled photon signals (b). In (a), Alice controls the emitted of single photon polarization, $\boldsymbol{a}_{1,2}$, from an attenuated laser and a polarization controller where Bob works to align his $\boldsymbol{b}_{1,2}$ based on the single photon count rates. In (b), Bob works to align his $\boldsymbol{b}_{1,2}$ to Alice's $\boldsymbol{a}_{1,2}$ from feedback coincidence measurements on the shared entangled $|\Psi^-\rangle$. Both Alice and Bob use the polarization and time multiplexed setup shown in chapter 3 and 4.

methods outlined above once $\boldsymbol{a}_{1,2}$ is recorded in Bob's frame through the use of equation (5.9).

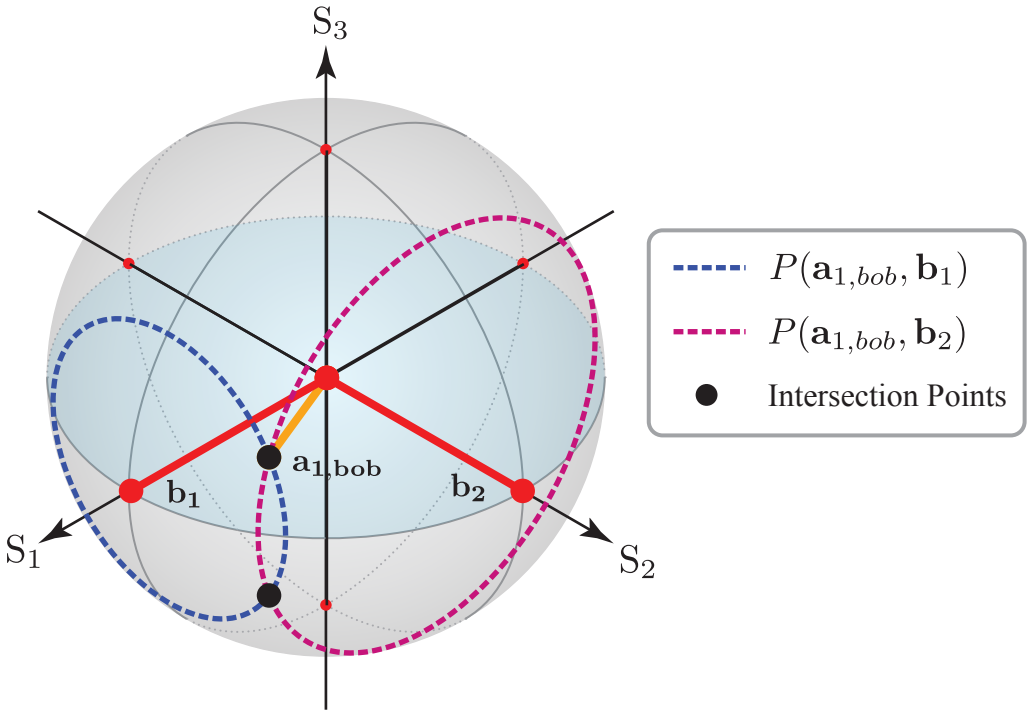

Figure 39: Bob mapping Alice's projection basis $\boldsymbol{a}_1$ onto his measurement frame $\boldsymbol{a}_{1,bob}$ to two intersection points from the probability of joint detection between his measurement bases $\boldsymbol{b}_{1,2}$.

Chapter A

Appendix

A.1 Polarization Ellipse

The electric field can be written as

$$\boldsymbol{E}(\mathbf{0},t)=\boldsymbol{E}_0 e^{-i\omega t}=\begin{pmatrix} E_{0x}e^{i\phi_x} \\ E_{0y}e^{i\phi_y} \end{pmatrix} e^{-i\omega t} \tag{A.1}$$

where E_{0x}, E_{0y}, ϕ_x, and ϕ_y are real numbers. This complex 2-row column vector is called the Jones polarization vector. The real-valued counterpart can be written as

$$\boldsymbol{E}(\mathbf{0},t)=E_{0x}\cos(\omega t+\phi_x)\hat{x}+E_{0y}\cos(\omega t+\phi_y)\hat{y} \quad . \tag{A.2}$$

This describes an ellipse as can be seen after some algebra. Define the time-dependent amplitudes as

$$X(t)=E_{0x}\cos(\omega t+\phi_x)$$

$$Y(t)=E_{0y}\cos(\omega t+\phi_y) \quad .$$

Rearranging these definitions, using the double angle formula for cosine/sine,

$$\frac{X}{E_{0x}}=\cos(\omega t)\cos\phi_x-\sin(\omega t)\sin\phi_x$$
$$\frac{Y}{E_{0y}}=\cos(\omega t)\cos\phi_y-\sin(\omega t)\sin\phi_y$$

multiplying by common factors,

$$\frac{X}{E_{0x}}\sin\phi_y=\cos(\omega t)\cos\phi_x\sin\phi_y-\sin(\omega t)\sin\phi_x\sin\phi_y$$
$$\frac{Y}{E_{0y}}\sin\phi_x=\cos(\omega t)\cos\phi_y\sin\phi_x-\sin(\omega t)\sin\phi_y\sin\phi_x$$
$$\frac{X}{E_{0x}}\cos\phi_y=\cos(\omega t)\cos\phi_x\cos\phi_y-\sin(\omega t)\sin\phi_x\cos\phi_y$$
$$\frac{Y}{E_{0y}}\cos\phi_x=\cos(\omega t)\cos\phi_y\cos\phi_x-\sin(\omega t)\sin\phi_y\cos\phi_x$$

and equating terms

$$\begin{aligned}\frac{X}{E_{0x}}\sin\phi_y-\frac{Y}{E_{0y}}\sin\phi_x&=\cos(\omega t)(\cos\phi_x\sin\phi_y-\cos\phi_y\sin\phi_x)\\&=\cos(\omega t)\sin(\phi_y-\phi_x)\\\frac{X}{E_{0x}}\cos\phi_y-\frac{Y}{E_{0y}}\cos\phi_x&=\sin(\omega t)(\sin\phi_y\cos\phi_x-\sin\phi_x\cos\phi_y)\\&=\sin(\omega t)\sin(\phi_y-\phi_x)\quad .\end{aligned}$$

Squaring the last two expressions gives

$$\frac{X^2}{E_{0x}^2}\sin^2\phi_y+\frac{Y^2}{E_{0y}^2}\sin^2\phi_x-2\frac{XY}{E_{0x}E_{0y}}\sin\phi_x\sin\phi_y=\cos^2(\omega t)\sin^2(\phi_y-\phi_x)$$
$$\frac{X^2}{E_{0x}^2}\cos^2\phi_y+\frac{Y^2}{E_{0y}^2}\cos^2\phi_x-2\frac{XY}{E_{0x}E_{0y}}\cos\phi_x\cos\phi_y=\sin^2(\omega t)\sin^2(\phi_y-\phi_x)$$

Adding them together gives the polarization ellipse equation

$$\begin{aligned}\frac{X^2}{E_{0x}^2}+\frac{Y^2}{E_{0y}^2}-2\frac{XY}{E_{0x}E_{0y}}(\sin\phi_x\sin\phi_y+\cos\phi_x\cos\phi_y)&=\sin^2(\phi_y-\phi_x)\\\frac{X^2}{E_{0x}^2}+\frac{Y^2}{E_{0y}^2}-2\frac{XY}{E_{0x}E_{0y}}\cos(\phi_y-\phi_x)&=\sin^2(\phi_y-\phi_x)\end{aligned}\qquad\text{(A.3)}$$

A.2 Electrodynamics in Cylindrical Wave guides

The propagation of optical fields in fiber is governed by the Maxwell equations [5]. Without free charges and currents and $\boldsymbol{M}=0$ due to the nonmagnetic nature of silica, these equations take the form

$$\begin{aligned}
\nabla\times\boldsymbol{E}(\boldsymbol{r},t)&=-\frac{\partial}{\partial t}\mu_0\boldsymbol{H}(\boldsymbol{r},t)\\
\nabla\times\boldsymbol{H}(\boldsymbol{r},t)&=\frac{\partial}{\partial t}\boldsymbol{D}(\mathbf{r},\mathbf{t})\\
\nabla\cdot\boldsymbol{D}(\boldsymbol{r},t)&=0\\
\nabla\cdot\mu_0\boldsymbol{H}(\boldsymbol{r},t)&=0
\end{aligned} \tag{A.4}$$

with $\boldsymbol{D}=\varepsilon_0\boldsymbol{E}+\boldsymbol{P}$. Taking the curl of (A.4), gives a Helmholtz equation similar to the wave equation (1.1)

$$\nabla^2\boldsymbol{E}(\boldsymbol{r},t)=-\frac{1}{c^2}\frac{\partial^2}{\partial t^2}\boldsymbol{E}-\mu_0\frac{\partial^2}{\partial t^2}\boldsymbol{P} \tag{A.5}$$

The Fourier transform of the electric field can be expressed as

$$\tilde{\boldsymbol{E}}(\boldsymbol{r},\omega)=\int_{-\infty}^{\infty}dt\boldsymbol{E}(\boldsymbol{r},t)e^{i\omega t} \tag{A.6}$$

With this in mind taking the Fourier transform of (A.5) gives

$$\nabla\times\nabla\times\tilde{\boldsymbol{E}}=\frac{\omega^2}{c^2}\tilde{\boldsymbol{E}}-\mu_0\omega^2\tilde{\boldsymbol{P}} \tag{A.7}$$

For linear optics $\tilde{\boldsymbol{P}}(\boldsymbol{r},\omega)=\varepsilon_0\chi^{(1)}(\boldsymbol{r},\omega)\tilde{\boldsymbol{E}}(\boldsymbol{r},\omega)$ (nonlinear optics is explained in section A.3) equation (A.9) can be simplified to

$$\nabla\times\nabla\times\tilde{\boldsymbol{E}}=\frac{\omega^2}{c^2}(1+\chi^{(1)})\tilde{\boldsymbol{E}} \quad . \tag{A.8}$$

Assuming $\nabla\cdot\tilde{\boldsymbol{E}}=0$ (valid for most practical $\chi^{(1)}$ materials) simplifies the expression to

$$\nabla^2\tilde{\boldsymbol{E}}+\frac{\omega^2}{c^2}(1+\chi^{(1)})\tilde{\boldsymbol{E}}=\nabla^2\tilde{\boldsymbol{E}}+n^2k_0^2\tilde{\boldsymbol{E}}=0 \quad . \tag{A.9}$$

where $k_0=\omega/c=2\pi/\lambda$ is the free-space wave number, λ is the vacuum wavelength of the optical field oscillating at frequency ω, and $n^2(\rho,\omega)=\left(1+\chi^{(1)}(\rho,\omega)\right)$ is the index of refraction of the material.

Because of the cylindrical symmetry of our waveguide, seen in figure 40a, we can rewrite (A.9) in terms of cylindrical coordinates ρ, ϕ, and z,

$$\frac{\partial^2}{\partial\rho^2}E_j+\frac{1}{\rho}\frac{\partial}{\partial\rho}E_j+\frac{1}{\rho^2}\frac{\partial^2}{\partial\phi^2}E_j+\frac{\partial^2}{\partial z^2}E_j+n^2k_0^2E_j=0 \quad . \tag{A.10}$$

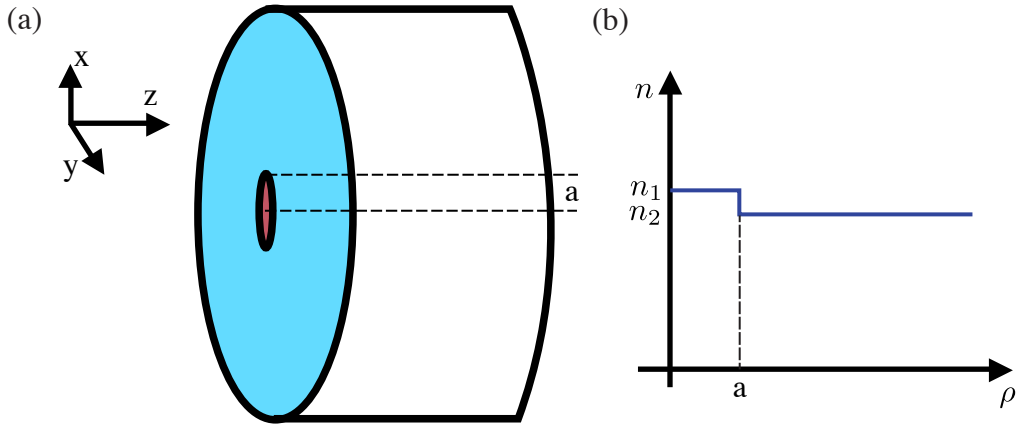

Figure 40: Schematic of single mode fiber]a) Step index cylindrical waveguide diagram with core radius a. Propagation direction is in z direction. b) Step index of refraction under weakly guiding approximation: $n_1\approx n_2$, but $n_1>n_2$.

For simplicity of notation, the tilde has been dropped, and the frequency dependency of the electric field E_j (for j=$\{\rho,\phi,z\}$), index of refraction, and wave number is implicitly assumed. For fibers used in our lab, the index of refraction of the material is a step-index where the material

changes a radius a away where $\rho \leq a$ defines the core.

$$n(\rho,\omega)=\begin{cases} n_1\ ; & \rho \leq a \\ n_2\ ; & \rho > a \end{cases} \tag{A.11}$$

with n_1,n_2 being real valued constants. Only two components of the electromagnetic field (E_z,H_z,E_ϕ,$H_\phi E_\rho H_\rho$) are truly independent, and the other 4 can be written in terms of the two independent components. Using E_z and H_z as our independent components we can solve equation (A.10) through the method of separation of variables.

$$\begin{aligned} E_z(\rho,\phi,z)&=F_E(\rho)\Phi_E(\phi)Z_E(z) \\ H_z(\rho,\phi,z)&=F_H(\rho)\Phi_H(\phi)Z_H(z) \end{aligned} \tag{A.12}$$

Only looking at the electric field and plugging this in we get

$$\frac{\partial^2 F_E}{\partial \rho^2}\Phi_E Z_E+\frac{1}{\rho}\frac{\partial F_E}{\partial \rho}\Phi_E Z_E+\frac{1}{\rho^2}F_E\frac{\partial^2 \Phi_E}{\partial \phi^2}Z_E+F_E\Phi_E\frac{\partial^2 Z_E}{\partial z^2}+n^2k_0^2F_E\Phi_E Z_E=0$$

$$\frac{1}{F_E}\frac{\partial^2 F_E}{\partial \rho^2}+\frac{1}{\rho F_E}\frac{\partial F_E}{\partial \rho}+n^2k_0^2+\frac{1}{\rho^2\Phi_E}\frac{\partial^2 \Phi_E}{\partial \phi^2}+\frac{1}{Z_E}\frac{\partial^2 Z_E}{\partial z^2}=0$$

Since the last term is purely a function of z it must be equal to some constant (we set this constant equal to $-\beta^2=\alpha+i\gamma$, but assuming losses are negligible $\gamma=0$) for the solution to hold for all values of ρ,ϕ. Thus

$$Z_E(z)=Z_0e^{-i\beta z} \quad .$$

Here we see β has the physical significance as the propagation constant for light moving down the

fiber. The remaining solution is

$$\frac{1}{F_E}\frac{\partial^2 F_E}{\partial \rho^2}+\frac{1}{\rho F_E}\frac{\partial F_E}{\partial \rho}+n^2k_0^2+\frac{1}{\rho^2\Phi_E}\frac{\partial^2\Phi_E}{\partial\phi^2}-\beta^2=0$$
$$\frac{\rho^2}{F_E}\frac{\partial^2 F_E}{\partial \rho^2}+\frac{\rho}{F_E}\frac{\partial F_E}{\partial \rho}+(n^2k_0^2-\beta^2)\rho^2+\frac{1}{\Phi_E}\frac{\partial^2\Phi_E}{\partial\phi^2}=0$$

Again, the last term is purely a function of ϕ, so it must also be equal to a constant $(-m)$. Here we make the additional restriction that m must be an integer because $\Phi_E(\phi)$ must be 2π periodic in ϕ (continuity of electric field for axial symmetric fibers). Our solution for Φ_E is

$$\Phi_E(\phi)=\Phi_0 e^{-im\phi} \quad .$$

We are left with the modified Bessel equation for $F_E(\rho)$:

$$\frac{\rho^2}{F_E}\frac{\partial^2 F_E}{\partial \rho^2}+\frac{\rho}{F_E}\frac{\partial F_E}{\partial \rho}+(n^2k_0^2-\beta^2)\rho^2-m=0$$
$$\rho^2\frac{\partial^2 F_E}{\partial \rho^2}+\rho\frac{\partial F_E}{\partial \rho}+\big((n^2k_0^2-\beta^2)\rho^2-m\big)F_E=0 \quad .$$

In the core and outside the core this has the expressions:

$$F_E(\rho):\begin{cases}\rho^2\frac{\partial^2 F_E}{\partial \rho^2}+\rho\frac{\partial F_E}{\partial \rho}+\big((n_1^2k_0^2-\beta^2)\rho^2-m\big)F_E=0; & \rho\leq a\\ \rho^2\frac{\partial^2 F_E}{\partial \rho^2}+\rho\frac{\partial F_E}{\partial \rho}-\big((\beta^2-n_2^2k_0^2)\rho^2+m\big)F_E=0; & \rho>a\end{cases}$$

This has Bessel function solutions [123] of the first and second kind (with integer m set by Φ solution) inside the core ($\rho\leq a$) and modified Bessel function solutions of the first and second kind

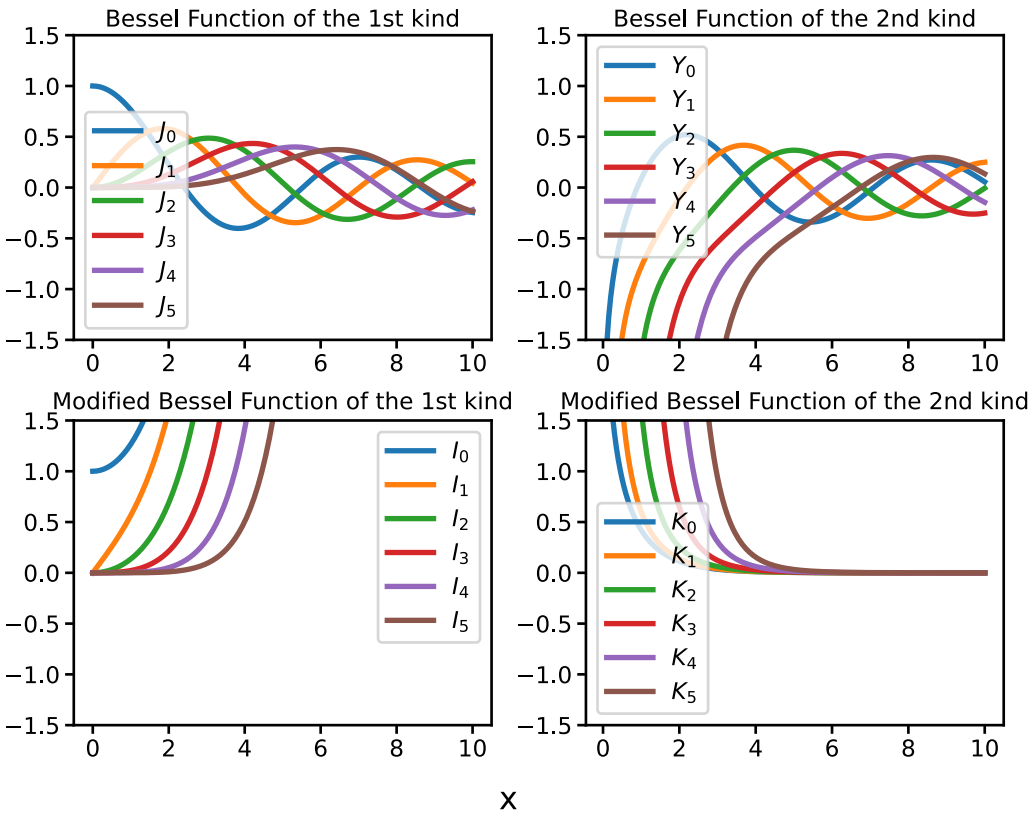

Figure 41: The first six Bessel and modified Bessel functions as a function of x.

outside the core ($\rho>a$). The behavior of each is seen in figure 41. The general equation for F_E is

$$F_E(\rho)=\begin{cases} A_m J_m((n_1^2k_0^2-\beta^2)\rho)+B_m Y_m((n_1^2k_0^2-\beta^2)\rho); & \rho\leq a \\ C_m K_m((\beta^2-n_2^2k_0^2)\rho)+D_m I_m((\beta^2-n_2^2k_0^2)\rho); & \rho>a \end{cases}$$

where A_m,B_m,C_m,D_m are constants. Looking at the behavior of these Bessel functions $Y_m\to\infty$ as $\rho\to 0$, therefore $B_m=0$ for realizable solutions. Likewise $I_m\to\infty$ as $\rho\to\infty$, therefore $D_m=0$. The full solutions for E_z and H_z (the same procedure is held for magnetic field) are

$$\begin{aligned} E_z&=\begin{cases} \sum_m A_m J_m((n_1^2k_0^2-\beta^2)\rho)e^{im\phi}e^{i\beta z}; & \rho\leq a \\ \sum_m C_m K_m((\beta^2-n_2^2k_0^2)\rho)e^{im\phi}e^{i\beta z}; & \rho>a \end{cases} \\ H_z&=\begin{cases} \sum_m B_m J_m((n_1^2k_0^2-\beta^2)\rho)e^{im\phi}e^{i\beta z}; & \rho\leq a \\ \sum_m D_m K_m((\beta^2-n_2^2k_0^2)\rho)e^{im\phi}e^{i\beta z}; & \rho>a \end{cases} \end{aligned} \tag{A.13}$$

Maxwell's equations in cylindrical coordinates for axially symmetric wave propagation are

$$\begin{cases} \frac{1}{\rho}\frac{\partial E_z}{\partial\phi}-i\beta E_\phi=i\omega\mu_0 H_\rho \\ i\beta E_\rho-\frac{\partial E_z}{\partial\rho}=i\omega\mu_0 H_\phi \\ \frac{1}{\rho}\frac{\partial}{\partial\phi}(\rho E_\phi)-\frac{1}{\rho}\frac{\partial E_\rho}{\partial\phi}=i\omega\mu_0 H_z \\ \frac{1}{\rho}\frac{\partial H_z}{\partial\phi}-i\beta H_\phi=-i\omega\varepsilon_0 n^2 E_\rho \\ i\beta H_\rho-\frac{\partial H_z}{\partial\rho}=-i\omega\varepsilon_0 n^2 E_\phi \\ \frac{1}{\rho}\frac{\partial}{\partial\phi}(\rho H_\phi)-\frac{1}{\rho}\frac{\partial H_\rho}{\partial\phi}=-i\omega\varepsilon_0 n^2 E_z \end{cases} \tag{A.14}$$

Solving for E_ρ,E_ϕ,H_ρ,H_ϕ in terms of E_z and H_z give

$$\begin{aligned}
E_\rho &= \frac{i}{h^2}\left(\beta\frac{\partial E_z}{\partial \rho}+\mu_0\frac{\omega}{\rho}\frac{\partial H_z}{\partial \phi}\right) \quad , \\
E_\phi &= \frac{i}{h^2}\left(\frac{\beta}{\omega}\frac{\partial E_z}{\partial \phi}-\mu_0\omega\frac{\partial H_z}{\partial \rho}\right) \quad , \\
H_\rho &= \frac{i}{h^2}\left(\beta\frac{\partial H_z}{\partial \rho}+\varepsilon_0 n^2\frac{\omega}{\rho}\frac{\partial E_z}{\partial \phi}\right) \quad , \\
H_\phi &= \frac{i}{h^2}\left(\frac{\beta}{\rho}\frac{\partial H_z}{\partial \rho}+\varepsilon_0 n^2\omega\frac{\partial H_z}{\partial \phi}\right) \quad .
\end{aligned} \tag{A.15}$$

where $h^2=n_1^2k_0^2-\beta^2$ inside the cladding ($\rho\leq a$) or $h^2=n_2^2k_0^2-\beta^2$ outside the cladding ($\rho>a$). To solve for coefficients A,B,C,D for a given mode we apply the boundary conditions across the intersection of the core and cladding by requiring the continuity of E_z,H_z,E_ϕ, and H_ϕ at $\rho=a$.

$$\begin{aligned}
A\beta\left(\frac{1}{u^2}-\frac{1}{v^2}\right)m &= -C\omega\mu_0\left[\frac{J_m'(u)}{uJ_m(u)}+\frac{K_m'(v)}{vK_m(v)}\right] \\
A\omega\varepsilon_0\left[n_1^2\frac{J_m'(u)}{uJ_m(u)}+n_2^2\frac{K_m'(v)}{vK_m(v)}\right] &= -C\beta\left(\frac{1}{u^2}-\frac{1}{v^2}\right)m \\
u^2 &= a^2\left(n_1^2k^2-\beta^2\right) \\
v^2 &= a^2\left(\beta^2-n_2^2k^2\right)
\end{aligned} \tag{A.16}$$

Cross multiplying and canceling out terms gives the dispersion relation

$$\left[\frac{J_m'(u)}{uJ_m(u)}+\frac{K_m'(v)}{vK_m(v)}\right]\left[\frac{J_m'(u)}{uJ_m(u)}+\left(\frac{n_2}{n_1}\right)^2\frac{K_m'(v)}{vK_m(v)}\right] = m^2\left(\frac{1}{u^2}+\frac{1}{v^2}\right)\left[\frac{1}{u^2}+\left(\frac{n_2}{n_1}\right)^2\frac{1}{v^2}\right] \quad . \tag{A.17}$$

The propagation constant β can be solved for any m mode. In general, for a given mode m, there are many (n=1,2,...) possible solutions. For each value of β_{mn} there is a unique possible mode of propagation of the optical field whose spatial distribution is defined by (A.13) and (A.15). For

most step fibers $n_2/n_1 \approx 1$ thus this can be reduced to a simpler relation

$$\frac{J'_m(u)}{uJ_m(u)} + \frac{K'_m(v)}{vK_m(v)} = \pm m\left(\frac{1}{u^2} + \frac{1}{v^2}\right) \quad . \tag{A.18}$$

In general, fiber modes have nonzero E_z and H_z field components (unlike what we saw for plane waves). The exception occurs for $m=0$ modes, where either E_z or H_z can be zero. Fiber modes where E_z and H_z are nonzero are called hybrid modes and are often labeled HE_{mn} or EH_{mn} depending on whether H_z or E_z is larger.

A.2.1 Single Mode Fiber and Birefringence Effects

It is possible to prove for small diameters, a, only one spatial mode propagates through the optical fiber, the fundamental mode HE_{11} (m=1,n=1). To show the loss of all other modes we'll look at the dispersion relation for $m=0$

$$vJ'_0(u)K_0(v) + uJ_0(u)K'_0(v) = 0 \quad . \tag{A.19}$$

A mode reaches cutoff when $v/a=0$. Defining this quantity as $q=\frac{v}{a}$ the cutoff condition can be seen by noting that the optical field of guided modes decays exponentially inside the cladding layer since

$$K_m(q\rho) = \sqrt{\pi/2q\rho}\,\exp(-q\rho) \qquad \text{for } q\rho \gg 1 \quad .$$

But when $q=0$ or when $q<0$ exponential decay is no longer possible. This simplifies the cutoff dispersion relations to

$$J_0(u) = 0 \quad . \tag{A.20}$$

Numerically, the first zero (n=1) for the zeroth order Bessel function $J_0(x)$ occurs for x=2.4048 up to the fourth decimal place of precision. When q=0, $u_{\text{cutoff}}=k_0 a_{\text{cutoff}}\sqrt{n_1^2-n_2^2}$. For telecom wavelengths and materials: λ=1.55μm, n_1=1.455, and n_2=1.45. This means the radius, a, must be less than

$$a_{\text{cutoff}}=\frac{2.4048}{(\frac{2\pi}{1.55\cdot 10^{-6}m})\sqrt{1.455^2-1.45^2}}=4.9\mu\text{m} \quad . \tag{A.21}$$

Most telecom fiber cores are designed with radii of width 4μm or smaller. For the HE_{11} mode we have dispersion relation

$$\frac{J_1'(u)}{uJ_1(u)}+\frac{K_1'(v)}{vK_1(v)}=\pm\left(\frac{1}{u^2}+\frac{1}{v^2}\right) \quad . \tag{A.22}$$

which using the Bessel function recurrence relations gives

$$\frac{J_2(u)}{uJ_1(u)}=-\frac{K_2(v)}{vK_1(v)}$$

for the plus sign of equation (A.22) and

$$\frac{J_0(u)}{uJ_1(u)}=\frac{K_0(v)}{vK_1(v)} \tag{A.23}$$

for the minus sign. Looking at (A.23) in the limit $v\to 0$ (for a mode being cutoff) we get

$$K_0(v)\to -\ln(v)+0.1159...$$

$$K_1(v)\to\frac{1}{v}$$

$$\frac{K_0(v)}{vK_1(v)}\to\infty$$

For $\frac{J_0(u_{\text{cutoff}})}{u_{\text{cutoff}}J_1(u_{\text{cutoff}})}$ to equal ∞ would mean a_{cutoff}=0. Therefore, as long as a is nonzero, the fundamental mode propagates while all other modes are cutoff (assuming $a<a_{\text{cutoff}}$).

The electric field of a single-mode fiber can be expressed in complete detail in Cartesian coordinates by plugging in m=1,n=1 mode (A.13) into (A.15)

$$E_x = E_\rho \cos\phi - E_\phi \sin\phi$$

$$E_y = E_\rho \sin\phi + E_\phi \cos\phi$$

$$E_z = E_z \quad .$$

The exact solutions are rigorously derived in chapter 3 of the textbook "Fundamentals of Optical Waveguides," written by Okamoto Katsunari [124]. However, the axial components, E_z and H_z are on the order of $\Delta^{1/2} = \left(\frac{n_1 - n_2}{n_2}\right)^{1/2} \ll 1$ [125]. Therefore, we can make the approximately linear polarized assumption and get

$$\begin{aligned}
E_x(\rho,\phi,z) &= E_0 \begin{cases} \left(J_0(\frac{u}{a}\rho)/J_0(u)\right)\cos\phi e^{i\beta z} & ; \quad \rho \le a \\ \left(K_0(\frac{v}{a}\rho)/K_0(v)\right)\cos\phi e^{i\beta z} & ; \quad \rho \le a \end{cases} \\
E_y(\rho,\phi,z) &= E_0 \begin{cases} \left(J_0(\frac{u}{a}\rho)/J_0(u)\right)\sin\phi e^{i\beta z} & ; \quad \rho \le a \\ \left(K_0(\frac{v}{a}\rho)/K_0(v)\right)\sin\phi e^{i\beta z} & ; \quad \rho \le a \end{cases} \\
E_z(\rho,\phi,z) &= 0 \quad .
\end{aligned} \tag{A.24}$$

This is analogous to the plane wave solutions 1.1, only E_0 isn't a constant over all space, but rather a function of the radius. The two-fold degeneracy can be seen in the symmetry of ϕ of the equations above. There exists two equal propagation modes for electric fields, in the x direction and y direction (ϕ=0 and ϕ=$\pi/2$). For the E_x propagation mode, the dominate magnetic field is in the y direction and given by $H_y = n_2(\varepsilon_0/\mu_0)^{1/2} E_x$. These equal polarization modes (of the fundamental hybrid mode) are often labeled HE_{11}^x and HE_{11}^y for electric fields in the x and y direction respectively. For real-world fibers, asymmetric constructions and asymmetric stresses

can break this degeneracy, and when this happens, the fiber becomes birefringent.

A.3 Nonlinear Optics

This section was generated from the class and lecture notes of Thomas E. Murphy's course, ENEE791 *Quantum Electronics II: Nonlinear Optics*. To generate entangled states of matter our experiment relies on the production of nearly identical photons. The creation of two identical photons is done through a process called spontaneous parametric down conversion. It hinges on the fact that at high enough intensities the material's response to an electromagnetic field becomes nonlinear. When this happens, for appropriate materials, a single photon can be down converted into two photons.

A.3.1 Nonlinear Polarization of Materials

The response of any dielectric material to intense enough light will become nonlinear with electromagnetic field strength. The relationship between the polarization of a material and electric field in general can be written as a power series with the electric field

$$P=\varepsilon_0\left(\chi^{(1)}E+\chi^{(2)}E^2+\chi^{(3)}E^3+...\right) \quad . \tag{A.25}$$

The polarization of the material is related to the induced dipole moments from an external field and is not to be confused with the polarization of light (1.5). The first term is the linear response of the medium that is well studied in classical electromagnetic textbooks, causing, among many things, dispersion, birefringence, and refraction, while the other terms represent the nonlinear response of the medium [5]. The term proportional to E^2 is the second-order nonlinear response, and $\chi^{(2)}$ is the second-order nonlinear susceptibility. This can be continued to the n^{th} order nonlinear response term and the n^{th} order nonlinear susceptibility $\chi^{(n)}$. The polarization can be written in

terms of the order of response

$$P=P^{(1)}+P^{(2)}+P^{(3)}+\cdots+P^{(n)}$$

with

$$P^{(1)}=\varepsilon_0\chi^{(1)}E$$

$$P^{(2)}=\varepsilon_0\chi^{(2)}E^2$$

$$P^{(3)}=\varepsilon_0\chi^{(3)}E^3$$

$$\vdots$$

$$P^{(n)}=\varepsilon_0\chi^{(n)}E^n$$

It is normally the case that all nonlinear susceptibilities are small in magnitude so that $P\approx P^{(1)}=\varepsilon_0\chi^{(1)}E$, but when E gets large the nonlinear terms cannot be ignored and we enter the domain of nonlinear optics. A host of interesting processes, such as second-harmonic generation, third-harmonic generation, sum and difference frequency generation, optical parametric amplification, and spontaneous parametric downconversion, are all consequences of including higher-order nonlinear terms.

The linear and nonlinear susceptibilities can be described as tensors. For example, if we look at the linear term explicitly in its vector formalism

$$\boldsymbol{P}^{(1)}=\varepsilon_0\boldsymbol{\chi}^{(1)}\cdot\boldsymbol{E}$$

$$\begin{bmatrix}P_x^{(1)}\\P_y^{(1)}\\P_z^{(1)}\end{bmatrix}=\varepsilon_0\begin{bmatrix}\chi_{xx}&\chi_{xy}&\chi_{xz}\\\chi_{yx}&\chi_{yy}&\chi_{yz}\\\chi_{zx}&\chi_{zy}&\chi_{zz}\end{bmatrix}\begin{bmatrix}E_x\\E_y\\E_z\end{bmatrix} \tag{A.26}$$

which can be more conveniently written using Einstein notation as

$$P_j^{(1)}=\varepsilon_0\chi_{jk}^{(1)}E_k \qquad \left(\sum_k \text{ implied}\right) \tag{A.27}$$

where summation is implied over any indices that are repeated in the same term. For the second-order nonlinear term the polarization can be written as

$$P_j^{(2)}=\varepsilon_0\chi_{jkl}^{(2)}E_kE_l \tag{A.28}$$

Nonlinear dielectric materials often used to study nonlinear processes have well defined crystal structures. The well-defined axes of crystalline materials make it necessary to consider the directions in which the fields are applied. Now consider x,y,z are now the orientations along the crystal. When looking at equation [A.28], we can contract the nonlinear susceptibility terms in the Kleinman limit (far from resonant frequencies of the crystal lattice) because we can assume $\chi_{jkl}^{(2)}$ is real. This is because $\chi_{xyz}^{(2)}E_yE_z=\chi_{xzy}^{(2)}E_zE_y$, $\chi_{yxz}^{(2)}E_xE_z=\chi_{yzx}^{(2)}E_zE_x$, etc. Grouping terms by E_jE_k for j,$k\in\{x,y,z\}$ simplifies equation [A.28] to

$$\begin{bmatrix} P_x^{(2)} \\ P_y^{(2)} \\ P_z^{(2)} \end{bmatrix} = \begin{bmatrix} d_{11} & d_{12} & d_{13} & d_{14} & d_{15} & d_{16} \\ d_{21} & d_{22} & d_{23} & d_{24} & d_{25} & d_{26} \\ d_{31} & d_{32} & d_{33} & d_{34} & d_{35} & d_{36} \end{bmatrix} \begin{bmatrix} E_xE_x \\ E_yE_y \\ E_zE_z \\ 2E_yE_z \\ 2E_zE_x \\ 2E_xE_y \end{bmatrix} \tag{A.29}$$

where we can see the relations

$$d_{11}=\varepsilon_0\chi^{(2)}_{xxx} \quad d_{12}=\varepsilon_0\chi^{(2)}_{xyy} \quad d_{13}=\varepsilon_0\chi^{(2)}_{xzz} \quad d_{14}=\varepsilon_0\chi^{(2)}_{xyz} \quad d_{15}=\varepsilon_0\chi^{(2)}_{xzx} \quad d_{16}=\varepsilon_0\chi^{(2)}_{xxy}$$

$$d_{21}=\varepsilon_0\chi^{(2)}_{yxx} \quad d_{22}=\varepsilon_0\chi^{(2)}_{yyy} \quad d_{23}=\varepsilon_0\chi^{(2)}_{yzz} \quad d_{24}=\varepsilon_0\chi^{(2)}_{yyz} \quad d_{25}=\varepsilon_0\chi^{(2)}_{yzx} \quad d_{26}=\varepsilon_0\chi^{(2)}_{yxy}$$

$$d_{31}=\varepsilon_0\chi^{(2)}_{zxx} \quad d_{32}=\varepsilon_0\chi^{(2)}_{zyy} \quad d_{33}=\varepsilon_0\chi^{(2)}_{zzz} \quad d_{34}=\varepsilon_0\chi^{(2)}_{zyz} \quad d_{35}=\varepsilon_0\chi^{(2)}_{zzx} \quad d_{36}=\varepsilon_0\chi^{(2)}_{zxy}$$

Often experimental tables listing the optical properties of crystals quote the values of these d_{jk} rather than χ_{jkl}.

A.3.1.1 Second Order Processes

Let us now take a closer look at $\chi^{(2)}$ processes. Let us assume our crystal has a large, nonzero $\chi^{(2)}$ and you have two incident monochromatic fields with frequencies ω_1 and ω_2

$$E_j(t)=\frac{1}{2}E_j(\omega_1)e^{-i\omega_1 t}+\frac{1}{2}E_j(\omega_2)e^{-i\omega_2 t}+c.c. \tag{A.30}$$

with c.c. being the complex conjugate of that prior argument. Here $E_j(\omega_1)$ is a constant, and ω_1 acts as a label and not a function of ω_1. Under the assumption that the material responds instantaneously and uniformly across frequencies to the applied electric fields, A.28 adequately describes the second-order polarization in time. Thus we would observe

$$\begin{aligned}
P^{(2)}_j &= \varepsilon_0\chi^{(2)}_{jkl}E_kE_l \\
&= \frac{\varepsilon_0\chi^{(2)}_{jkl}}{4}(E_k(\omega_1)e^{-i\omega_1 t}+E_k(\omega_2)e^{-i\omega_2 t}+c.c)(E_l(\omega_1)e^{-i\omega_1 t}+E_l(\omega_2)e^{-i\omega_2 t}+c.c) \\
&= \frac{\varepsilon_0\chi^{(2)}_{jkl}}{4}[\\
&\qquad (E_k(\omega_1)E_l(\omega_1)e^{-i2\omega_1 t}+E_k(\omega_2)E_l(\omega_2)e^{-i2\omega_2 t}+c.c.) \qquad \text{(Second Harmonic)}
\end{aligned}$$

$(E_k(\omega_1)E_l^*(\omega_1)+E_k(\omega_2)E_l^*(\omega_2)+c.c)$ (Optical Rectification)

$(E_k(\omega_1)E_l(\omega_2)e^{-i(\omega_1+\omega_2)t}+E_k(\omega_2)E_l(\omega_1)e^{-i(\omega_1+\omega_2)t}+c.c.)$ (Sum Frequency)

$(E_k(\omega_1)E_l^*(\omega_2)e^{-i(\omega_1-\omega_2)t}+E_k(\omega_2)E_l^*(\omega_1)e^{-i(\omega_1-\omega_2)t}+c.c.)]$

(Difference Frequency)

Thus you get novel radiation terms at the frequencies $\{0,2\omega_1,2\omega_2,\omega_1+\omega_2,\omega_1-\omega_2\}$. This can be summarized visually in Fig. [42] below. When $\omega_1=\omega_2=\omega$ one would see a strong 2ω signal. The

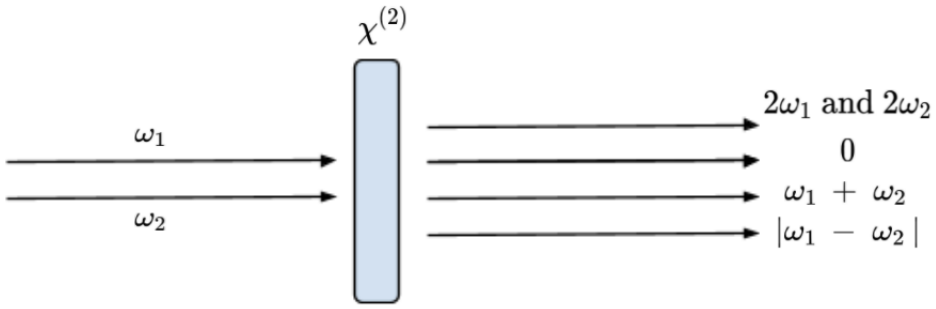

Figure 42: Second Harmonic Generation in a $\chi^{(2)}$ crystal

generation of correlated and entangled photons through spontaneous parametric downconversion is analogous to this process in reverse. It should be noted that for materials with a time-dependent response, instead of instantaneous like assumed here, the description is more complicated.

A.3.2 Propagation Through $\chi^{(2)}$ Materials

To fully understand the creation of light at new wavelengths within a nonlinear crystal, we must have coupled propagation equations of light, through space and time, at the newly created frequencies, and at the pump. Starting with Maxwell's Equations and examining a source free region, valid for our dielectric crystals, our electric and magnetic fields are

$$\nabla\times\boldsymbol{E}(\boldsymbol{r},t)=-\mu_0\frac{\partial}{\partial t}\boldsymbol{H}(\boldsymbol{r},t) \tag{A.31}$$

$$\nabla\times\boldsymbol{H}(\boldsymbol{r},t)=\frac{\partial}{\partial t}\boldsymbol{D}(\boldsymbol{r},t) \tag{A.32}$$

where the displacement vector $\boldsymbol{D}$ relates the electric and induced polarization. Separating the linear and nonlinear parts by equation [A.25] we have

$$\boldsymbol{D}(\boldsymbol{r},t)=\varepsilon_0\boldsymbol{E}(\boldsymbol{r},t)+P^{(1)}(\boldsymbol{r},t)+P^{(NL)}(\boldsymbol{r},t) \quad . \tag{A.33}$$

Taking the curl of equation [A.31] and it's Fourier transform we have

$$\begin{aligned}
\nabla\times\nabla\times\boldsymbol{E}(\boldsymbol{r},t)&=-\mu_0\frac{\partial}{\partial t}\nabla\times\boldsymbol{H}(\boldsymbol{r},t)\\
&=-\mu_0\frac{\partial^2}{\partial t^2}\boldsymbol{D}(\boldsymbol{r},t)\\
\nabla\times\nabla\times\boldsymbol{E}(\boldsymbol{r},t)+\mu_0\frac{\partial^2}{\partial t^2}\Big[\varepsilon_0\boldsymbol{E}(\boldsymbol{r},t)+\boldsymbol{P}^{(1)}(\boldsymbol{r},t)\Big]&=-\mu_0\frac{\partial^2}{\partial t^2}\boldsymbol{P}^{(NL)}(\boldsymbol{r},t)\\
\nabla\times\nabla\times\mathcal{F}(\boldsymbol{E}(\boldsymbol{r},t))+\mu_0\frac{\partial^2}{\partial t^2}\Big[\varepsilon_0\mathcal{F}(\boldsymbol{E}(\boldsymbol{r},t))+\mathcal{F}\Big(\boldsymbol{P}^{(1)}(\boldsymbol{r},t)\Big)\Big]&=-\mu_0\frac{\partial^2}{\partial t^2}\mathcal{F}\Big(\boldsymbol{P}^{(NL)}(\boldsymbol{r},t)\Big)\\
\nabla\times\nabla\times\hat{\boldsymbol{E}}(\boldsymbol{r},\omega)+\mu_0\frac{\partial^2}{\partial t^2}\Big[\varepsilon_0\hat{\boldsymbol{E}}(\boldsymbol{r},\omega)+\hat{\boldsymbol{P}}^{(1)}(\boldsymbol{r},\omega)\Big]&=-\mu_0\frac{\partial^2}{\partial t^2}\hat{\boldsymbol{P}}^{(NL)}(\boldsymbol{r},\omega)\\
\nabla\times\nabla\times\hat{\boldsymbol{E}}(\boldsymbol{r},\omega)-\mu_0\omega^2\Big[\varepsilon_0\hat{\boldsymbol{E}}(\boldsymbol{r},\omega)+\hat{\boldsymbol{P}}^{(1)}(\boldsymbol{r},\omega)\Big]&=\mu_0\omega^2\hat{\boldsymbol{P}}^{(NL)}(\boldsymbol{r},\omega)
\end{aligned}$$

leaving,

$$\nabla\times\nabla\times\hat{\boldsymbol{E}}(\boldsymbol{r},\omega)-\mu_0\omega^2\boldsymbol{\epsilon}(\omega)\hat{\boldsymbol{E}}(\boldsymbol{r},\omega)=\mu_0\omega^2\hat{\boldsymbol{P}}^{(NL)}(\boldsymbol{r},\omega) \tag{A.34}$$

where we used

$$\begin{aligned}
\hat{\boldsymbol{P}}^{(1)}(\boldsymbol{r},\omega)&=\varepsilon_0\boldsymbol{\chi}^{(1)}(-\omega;\omega)\hat{\boldsymbol{E}}(\boldsymbol{r},\omega)\\
\boldsymbol{\epsilon}(\omega)&=\varepsilon_0\Big(1+\boldsymbol{\chi}^{(1)}(-\omega;\omega)\Big) \quad .
\end{aligned}$$

Equation [A.34] is nothing more than a Helmholtz equation in the frequency domain where the nonlinear polarization is acting as a driving term.

We now assume the electric field can be described as a plane wave, or linear combination of plane waves, propagating in the +x direction with a gradually varying amplitude

$$\hat{\boldsymbol{E}}(\boldsymbol{r},\omega)=\boldsymbol{\mathcal{E}}(x,\omega)e^{ikx} \tag{A.35}$$

where k is to be taken as the wavevector at the frequency ω in the absence of any nonlinearity

$$k(\omega)=n(\omega)\frac{\omega}{c}=\omega\sqrt{\mu_0\epsilon(\omega)} \quad . \tag{A.36}$$

Plugging in (A.35) to (A.34) gives

$$\frac{\partial^2}{\partial x^2}\left[\boldsymbol{\mathcal{E}}e^{ikx}\right]-\mu_0\omega^2\boldsymbol{\epsilon}(\omega)\boldsymbol{\mathcal{E}}e^{ikx}=\mu_0\omega^2\hat{\boldsymbol{P}}^{(NL)}(x,\omega) \quad . \tag{A.37}$$

Since $\boldsymbol{\mathcal{E}}_\omega(x)$ is assumed to be a gradually-varying function of x the second derivative term can be approximated as

$$\begin{aligned}\frac{\partial^2}{\partial x^2}\left[\boldsymbol{\mathcal{E}}e^{ikx}\right]&=\frac{\partial}{\partial x}\left(\frac{\partial\boldsymbol{\mathcal{E}}}{\partial x}e^{ikx}+ik\boldsymbol{\mathcal{E}}e^{ikx}\right)\\&=\left(\frac{\partial^2\boldsymbol{\mathcal{E}}}{\partial x^2}+i2k\frac{\partial\boldsymbol{\mathcal{E}}}{\partial x}-k^2\boldsymbol{\mathcal{E}}\right)e^{ikx}\\\frac{\partial^2}{\partial x^2}\left[\boldsymbol{\mathcal{E}}e^{ikx}\right]&\approx\left(i2k\frac{\partial\boldsymbol{\mathcal{E}}}{\partial x}-k^2\boldsymbol{\mathcal{E}}\right)e^{ikx}\end{aligned} \tag{A.38}$$

in the limit

$$\left|\frac{\partial^2\boldsymbol{\mathcal{E}}}{\partial x^2}\right|\ll\left|k\frac{\partial\boldsymbol{\mathcal{E}}}{\partial x}\right|$$

With this approximation (A.37) becomes

$$\frac{\partial}{\partial x}\mathcal{E}_j(x,\omega)=i\frac{\omega}{2n(\omega)c\varepsilon_0}P_j^{(NL)}(x,\omega)e^{-ikx} \tag{A.39}$$

For $\chi^{(2)}$ processes we have seen that we can have mixing between two frequencies ω_1 and ω_2 such that a nonlinear polarization term will oscillate at the sum frequency $\omega_3=\omega_1+\omega_2$. With ω_3 present and $\omega_{1,2}$ we can get the $\omega_{2,1}$ through difference frequency generation $\omega_{1,2}=\omega_3-\omega_{2,1}$.

$$\hat{P}_j^{(2)}(x,\omega_3)=\varepsilon_0\chi_{jkl}^{(2)}(-\omega_3;\omega_1,\omega_2)\hat{\mathcal{E}}_k(x,\omega_1)\hat{\mathcal{E}}_l(x,\omega_2)e^{i(k_1+k_2)x} \tag{A.40}$$

$$\hat{P}_j^{(2)}(x,\omega_2)=\varepsilon_0\chi_{jkl}^{(2)}(-\omega_2;\omega_3,-\omega_1)\hat{\mathcal{E}}_k(x,\omega_3)\hat{\mathcal{E}}_l^*(x,\omega_1)e^{i(k_3-k_1)x} \tag{A.41}$$

$$\hat{P}_j^{(2)}(x,\omega_1)=\varepsilon_0\chi_{jkl}^{(2)}(-\omega_1;\omega_3,-\omega_2)\hat{\mathcal{E}}_k(x,\omega_3)\hat{\mathcal{E}}_l^*(x,\omega_2)e^{i(k_3-k_2)x} \tag{A.42}$$

Plugging these into equation (A.39) we get the 3 coupled differential equations for the electric fields at the three different frequencies

$$\begin{aligned}
\frac{\partial}{\partial x}\mathcal{E}_j(x,\omega_1)&=i\frac{\omega_1}{2n(\omega_1)c}\chi_{jkl}^{(2)}(-\omega_1;\omega_3,-\omega_2)\mathcal{E}_k(x,\omega_3)\mathcal{E}_l^*(x,\omega_2)e^{-i(\Delta k)x}\\
\frac{\partial}{\partial x}\mathcal{E}_j(x,\omega_2)&=i\frac{\omega_2}{2n(\omega_2)c}\chi_{jkl}^{(2)}(-\omega_2;\omega_3,-\omega_1)\mathcal{E}_k(x,\omega_3)\mathcal{E}_l^*(x,\omega_1)e^{-i(\Delta k)x}\\
\frac{\partial}{\partial x}\mathcal{E}_j(x,\omega_3)&=i\frac{\omega_3}{2n(\omega_3)c}\chi_{jkl}^{(2)}(-\omega_3;\omega_1,\omega_2)\mathcal{E}_k(x,\omega_1)\mathcal{E}_l(x,\omega_2)e^{i(\Delta k)x}
\end{aligned} \tag{A.43}$$

with the phase matching parameter,

$$\Delta k=k_1+k_2-k_3 \quad . \tag{A.44}$$

A.3.3 SPDC in PPKTP Type-II Waveguide

The Sellmeier equations for any material are empirical relations between the material's refractive index and wavelength of light transmitting through it. In its most general form

$$n_j^2(\lambda)=1=\sum_i \frac{B_{i,j}\lambda^2}{\lambda^2-C_{i,j}} \tag{A.45}$$

where n_j is the refractive index along the crystal's $j=\{x,y,z\}$ direction, λ the wavelength, $B_{i,j}$ and $C_{i,j}$ are experimentally determined Sellmeier coefficients. λ is often listed in micrometers. For materials like Potassium titanyl phosphate (KTP), a biaxial nonlinear crystal in the mm2 point symmetry group, the materials are approximated by the Sellmeier equations [126]

$$\begin{aligned} n_x^2(\lambda)&=3.0065+\frac{0.03901}{\lambda^2-0.04251}-0.01327\lambda^2 \\ n_y^2(\lambda)&=3.0333+\frac{0.04154}{\lambda^2-0.04547}-0.01408\lambda^2 \\ n_z^2(\lambda)&=3.3134+\frac{0.05694}{\lambda^2-0.05658}-0.01682\lambda^2 \quad . \end{aligned} \tag{A.46}$$

A plot of the Sellmeier equations for KTP is seen below in Fig. 43. In the Kleinman limit there are 7 non zero $\chi^{(2)}_{jkl}$ which are completely described by three different coefficients

$$\begin{aligned} d_{31}&=d_{15}\approx 2.5 \text{ pm/V} \\ d_{32}&=d_{24}\approx 4.4 \text{ pm/V} \\ d_{33}&\approx 16.9 \text{ pm/V} \end{aligned} \tag{A.47}$$

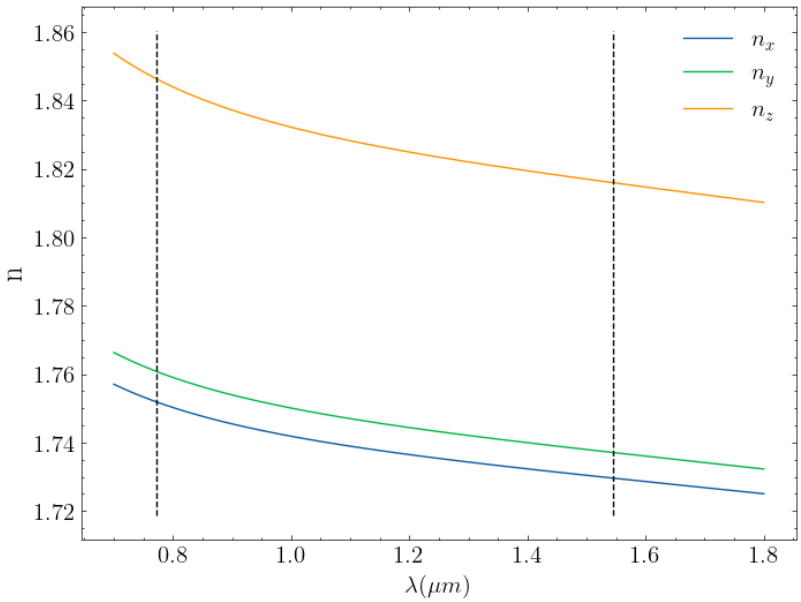

Figure 43: Index of refraction along x, y, z directions of KTP as a function of wavelength. Black dotted lines show the location of the experimental pump at 772.2nm and the down converted photons at 1544.4nm.

or alternatively in the matrix representation presented above,

$$\boldsymbol{d}=\begin{bmatrix} 0 & 0 & 0 & 0 & 2.5 & 0 \\ 0 & 0 & 0 & 4.4 & 0 & 0 \\ 2.5 & 4.4 & 16.9 & 0 & 0 & 0 \end{bmatrix} \text{[pm/V]}$$

Spontaneous parametric down conversion through a nonlinear crystal like KTP is a three-wave mixing process similar to sum frequency generation described above (A.43), only in reverse. Instead of two photons at ω_1 and ω_2 producing $\omega_3{=}\omega_1{+}\omega_2$. A pump photon at ω_p occasionally splits into two photons ω_i,ω_s such that $\omega_p{=}\omega_i{+}\omega_s$. As shown in the Fig. [44] light with frequency 2ω polarized in the y direction (to take advantage of PPKTP's high d_{32} as we'll see shortly) shines on the PPKTP waveguide and produces two photons polarized in the y and z direction. In the special case that the two downconverted photons are degenerate in frequency $\omega_s{=}\omega_i{=}\omega$ the three mixing electric fields (pump, signal, and idler) are

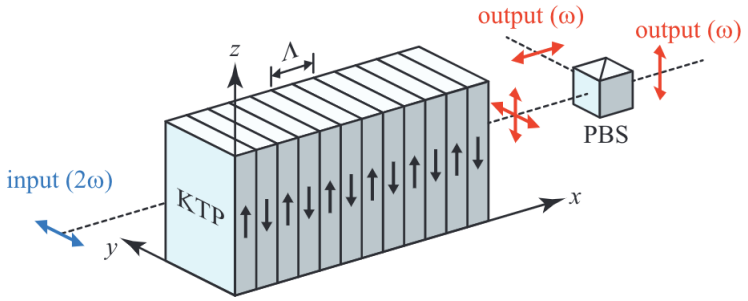

Figure 44: Spontaneous parametric down conversion in a type-II PPKTP waveguide. A pump (2ω) polarized in the y direction occasionally creates a signal and idler photons polarized in the y and z respectively. Fig. taken Prof Murphy's Nonlinear Optics Course.

$$\begin{aligned}
\boldsymbol{E}_p(x,t) &= \hat{y}\frac{1}{2}A_p e^{i(k_p x-2\omega t)}+c.c. \\
\boldsymbol{E}_s(x,t) &= \hat{y}\frac{1}{2}A_s e^{i(k_s x-\omega t)}+c.c. \\
\boldsymbol{E}_i(x,t) &= \hat{z}\frac{1}{2}A_i e^{i(k_i x-\omega t)}+c.c. \quad .
\end{aligned} \tag{A.48}$$

Using equations (A.43) in the slowly varying envelope approximation and taking careful consideration of the vectors used we have

$$\begin{aligned}
\frac{\partial}{\partial x}A_s(x,\omega) &= i\frac{\omega}{2n_y(\omega)c}\chi^{(2)}_{yyz}(-\omega;2\omega,-\omega)A_p(x,2\omega)A_i^*(x,\omega)e^{-i\Delta k x} \\
\frac{\partial}{\partial x}A_i(x,\omega) &= i\frac{\omega}{2n_z(\omega)c}\chi^{(2)}_{zyy}(-\omega;2\omega,-\omega)A_p(x,2\omega)A_s^*(x,\omega)e^{-i\Delta k x} \\
\frac{\partial}{\partial x}A_p(x,2\omega) &= i\frac{2\omega}{2n_y(2\omega)c}\chi^{(2)}_{yyz}(-2\omega;\omega,\omega)A_s(x,\omega)A_i(x,\omega)e^{i\Delta k x}
\end{aligned} \tag{A.49}$$

with a phase matching condition

$$\begin{aligned}
\Delta k &= k_y(\omega)+k_z(\omega)-k_y(2\omega)=\frac{n_y(\omega)\omega}{c}+\frac{n_z(\omega)\omega}{c}-\frac{n_y(2\omega)2\omega}{c} \\
&= \frac{n_y(\lambda)2\pi}{\lambda}+\frac{n_z(\lambda)2\pi}{\lambda}-\frac{n_y(\lambda/2)4\pi}{\lambda} \quad .
\end{aligned} \tag{A.50}$$

Looking at the relations between $\chi^{(2)}_{jkl}$ and d_{jk} listed above we see $\chi^{(2)}_{yyz}=d_{24}=\chi^{(2)}_{zyy}=d_{32}=4.4$

pm/V.

By inverting the crystal orientation from +z to -z flips that is seen within the periodic poling process for PPKTP, the second-order nonlinear susceptibility undergoes the following transformation matrix

$$\hat{R}=\begin{bmatrix} 1 & 0 & 0 \\ 0 & 1 & 0 \\ 0 & 0 & -1 \end{bmatrix} \tag{A.51}$$

which introduces a factor of -1 each time z shows up in $\chi^{(2)}_{jkl}$. Therefore $\hat{R}\chi^{(2)}_{yyz}=-\chi^{(2)}_{yyz}$ and the coupled equations become

$$\begin{aligned} \frac{\partial}{\partial x}A_s(x,\omega)&=-i\frac{\omega}{2n_y(\omega)c}d_{32}A_p(x,2\omega)A_i^*(x,\omega)e^{-i\Delta kx} \\ \frac{\partial}{\partial x}A_i(x,\omega)&=-i\frac{\omega}{2n_z(\omega)c}d_{32}(-\omega;2\omega,-\omega)A_p(x,2\omega)A_s^*(x,\omega)e^{-i\Delta kx} \\ \frac{\partial}{\partial x}A_p(x,2\omega)&=-i\frac{2\omega}{2n_y(2\omega)c}d_{32}(-2\omega;\omega,\omega)A_s(x,\omega)A_i(x,\omega)e^{i\Delta kx} \quad . \end{aligned} \tag{A.52}$$

This causes the inefficiencies from non phase matched Δk after propagation through the KTP crystal to be zeroed by compensating for another non phase matched Δk in the opposite direction. This process is called quasi-phase matching. With a periodic poling between Λ between successive up or downward z crystal orientations, the new nonlinear equations governing the PPKTP waveguide are

$$\begin{aligned} \frac{\partial}{\partial x}A_s(x,\omega)&=i\frac{\omega}{n_y(\omega)c}d_{eff}A_p(x,2\omega)A_i^*(x,\omega)e^{-i\Delta k'x} \\ \frac{\partial}{\partial x}A_i(x,\omega)&=i\frac{\omega}{n_z(\omega)c}d_{eff}(-\omega;2\omega,-\omega)A_p(x,2\omega)A_s^*(x,\omega)e^{-i\Delta kx} \\ \frac{\partial}{\partial x}A_p(x,2\omega)&=i\frac{2\omega}{n_y(2\omega)c}d_{eff}(-2\omega;\omega,\omega)A_s(x,\omega)A_i(x,\omega)e^{i\Delta kx} \quad . \end{aligned} \tag{A.53}$$

where

$$d_{eff}=\frac{2}{\pi}d_{32}, \qquad \Delta k'=k_y(\omega)+k_z(\omega)-k_y(2\omega)-n\frac{2\pi}{\Lambda} \quad . \tag{A.54}$$

and n is an integer. For $n=1$ we see the periodic spacing should be $\Lambda=49.0\mu$m for successful quasi phase matching.

From our SPDC spectrum shown in figure 14 we know perfect production at $\omega_i=\omega_s=\omega_p/2$ is not guaranteed. Assuming ω_p is constant, decreasing ω_i will correspond to an increase in ω_s. However, a waveguide length of $L=1$ cm with the maximum and minimum possible phase matching conditions

$$\Delta k' L=\pm\pi=\pm 2\pi L(n(\lambda_i)/\lambda_i+n(\lambda_s)/\lambda_s-n(\lambda_p)/\lambda_p-1/\Lambda)$$

we can get a wavelength range of possible generated frequencies for λ_i, assuming

$$\lambda_s=(\lambda_p^{-1}-\lambda_i^{-1})^{-1}$$

$$1.5426\ \mu\text{m}\leq\lambda_i\leq 1.5454\ \mu\text{m} \quad .$$

Bibliography

[1] E. Dowling, M. Morris, G. Baumgartner, R. Roy, and T. E. Murphy. Non-local polarization alignment and control in fibers using feedback from correlated measurements of entangled photons. *Opt. Express*, 31(2):2316–2329, Jan 2023.

[2] E. Dowling, M. Morris, G. Baumgartner, R. Roy, and T. E. Murphy. Automated Bell Inequality Violation using Uncalibrated Fiber Squeezing Polarization Controllers. In *CLEO 2023*, page FM1A.2. Optica Publishing Group, 2023.

[3] E. Dowling, R. Roy, and T. E. Murphy. Polarization Drift Compensation in Fiber using Feedback from Correlated Measurements of Entangled Photons. In *APS March Meeting Abstracts*, volume 2022 of *APS Meeting Abstracts*, page F35.011, Mar. 2022.

[4] E. Dowling, R. Roy, and T. Murphy. Self-guided method to search for EPR state correlations using uncalibrated polarization controllers in a plug-and-play optical system. In *APS March Meeting Abstracts*, volume 2021 of *APS Meeting Abstracts*, page H71.139, Jan. 2021.

[5] D. J. Griffiths. *Introduction to electrodynamics*. Pearson, 2013.

[6] J. N. Damask. *Polarization optics in telecommunications*, volume 101. Springer Science & Business Media, 2004.

[7] R. C. Jones. A New Calculus for the Treatment of Optical Systems I. Description and Discussion of the Calculus. *J. Opt. Soc. Am.*, 31(7):488–493, Jul 1941.

[8] H. Hurwitz and R. C. Jones. A New Calculus for the Treatment of Optical Systems II. Proof of Three General Equivalence Theorems. *Journal of the Optical Society of America*, 31:493–499, 1941.

[9] R. C. Jones. A New Calculus for the Treatment of Optical Systems IV. *J. Opt. Soc. Am.*, 32(8):486–493, Aug 1942.

[10] T. Imai and T. Matsumoto. Polarization fluctuations in a single-mode optical fiber. *Journal of Lightwave Technology*, 6(9):1366–1375, 1988.

[11] C. D. Poole, J. H. Winters, and J. A. Nagel. Dynamical equation for polarization dispersion. *Opt. Lett.*, 16(6):372–374, Mar 1991.

[12] M. Brodsky, N. J. Frigo, M. Boroditsky, and M. Tur. Polarization mode dispersion of installed fibers. *Journal of Lightwave Technology*, 24:4584–4599, 2006.

[13] J. Hayes. *The FOA Reference Guide to Fiber Optics and Study Guide to FOA Certification*. Fiber Optic Association, 2009.

[14] C. B. Czegledi, M. Karlsson, E. Agrell, and P. Johannisson. Polarization drift channel model for coherent fibre-optic systems. *Scientific Reports*, 6, 2 2016.

[15] Y.-Y. Ding, H. Chen, S. Wang, D.-Y. He, Z.-Q. Yin, W. Chen, Z. Zhou, G.-C. Guo, and Z.-F. Han. Polarization variations in installed fibers and their influence on quantum key distribution systems. *Opt. Express*, 25(22):27923–27936, Oct 2017.

[16] M. Karlsson, J. Brentel, and P. A. Andrekson. Long-term measurement of pmd and polarization drift in installed fibers. *Journal of Lightwave Technology*, 18(7):941, Jul 2000.

[17] Y.-Y. Ding, H. Chen, S. Wang, D.-Y. He, Z. Yin, W. Chen, Z. Zhou, G.-C. Guo, and Z.-F. Han. Polarization variations in installed fibers and their influence on quantum key distribution systems. *Optics Express*, 25:27923, 10 2017.

[18] D. S. Waddy, L. Chen, and X. Bao. Polarization effects in aerial fibers. *Optical Fiber Technology*, 11(1):1–19, 2005.

[19] C. D. Angelis, A. Galtarossa, G. Gianello, F. Matera, and M. Schiano. Time evolution of polarization mode dispersion in long terrestrial links. *J. Lightwave Tech.*, 10, 1992.

[20] Z. Zhang, X. Bao, Q. Yu, and L. Chen. Fast state of polarization and pmd drift in submarine fibers. *Photon Tech Lett*, 18, 2006.

[21] D.-D. Li, S. Gao, G.-C. Li, L. Xue, L.-W. Wang, C.-B. Lu, Y. Xiang, Z.-Y. Zhao, L.-C. Yan, Z.-Y. Chen, G. Yu, and J.-H. Liu. Field implementation of long-distance quantum key distribution over aerial fiber with fast polarization feedback. *Opt. Express*, 26(18):22793–22800, Sep 2018.

[22] R. Harmon. Polarisation stability in long lengths of monomode fibre. *Electronics Letters*, 18:1058–1060(2), November 1982.

[23] C. Poole and R. Wagner. Phenomenological approach to polarisation dispersion in long single-mode fibres. *Electronics Letters*, 22:1029–1030(1), September 1986.

[24] S. H. Rumbaugh. Endless state-of-polarization control for coherent optical communication systems using nematic liquid crystal. *Dissertations and Thesis*, 1989.

[25] J. D. N.G. Walker, G.R. Walker. Endless polarisation control using an integrated optic lithium niobate device. *Electronics Letters*, 24:266–268(2), March 1988.

[26] N. G. Walker and G. R. Walker. Polarization Control for Coherent Communications. *Journal of Lightwave Technology*, 8(3):438–458, 1990.

[27] R. Noé, H. Heidrich, and D. Hoffmann. Endless Polarization Control Systems for Coherent Optics. *Journal of Lightwave Technology*, 6(7):1199–1208, 1988.

[28] R. Noé, H. Heidrich, and D. Hoffmann. Automatic endless polarization control with

integrated-optical Ti:LiNbO3 polarization transformers. *Opt. Lett.*, 13(6):527–529, Jun 1988.

[29] N. Walker. Endless polarisation control using four fibre squeezers. *Electronics Letters*, 23:290–292(2), March 1987.

[30] N. J. Muga, M. F. S. Ferreira, and A. N. Pinto. QBER Estimation in QKD Systems With Polarization Encoding. *Journal of Lightwave Technology*, 29(3):355–361, 2011.

[31] C. Agnesi, M. Avesani, L. Calderaro, A. Stanco, G. Foletto, M. Zahidy, A. Scriminich, F. Vedovato, G. Vallone, and P. Villoresi. Simple quantum key distribution with qubit-based synchronization and a self-compensating polarization encoder. *Optica*, 7(4):284–290, Apr 2020.

[32] N. Menkart, J. D. Hart, T. E. Murphy, and R. Roy. Dark current and single photon detection by 1550 nm avalanche photodiodes: dead time corrected probability distributions and entropy rates. *Opt. Express*, 30(22):39431–39444, Oct 2022.

[33] Y. Kang, H. X. Lu, Y.-H. Lo, D. S. Bethune, and W. P. Risk. Dark count probability and quantum efficiency of avalanche photodiodes for single-photon detection. *App. Phys. Lett.*, 83(14):2955–2957, 10 2003.

[34] G. B. Xavier, G. Vilela de Faria, G. P. Temporão, J. P. von der Weid, z. Peng, J. Zhang, D. Yang, W.-b. Gao, H.-x. Ma, H. Yin, H.-p. Zeng, T. Yang X-B Wang, J. Waldebäck, M. Tengner, D. Ljunggren, and A. Karlsson. Full polarization control for fiber optical quantum communication systems using polarization encoding. *Optics Express*, 16(3):1867–1873, 2008.

[35] G. B. Xavier, N. Walenta, G. V. de Faria, G. P. Temporão, N. Gisin, H. Zbinden, and J. P.

von der Weid. Experimental polarization encoded quantum key distribution over optical fibres with real-time continuous birefringence compensation. *New J. Phys.*, 11(4):045015, apr 2009.

[36] M. Martinelli and R. A. Chipman. Endless Polarization Control Algorithm Using Adjustable Linear Retarders With Fixed Axes. *Journal of Lightwave Technology*, 21(9):2089–2096, 9 2003.

[37] M. Martinelli, P. Martelli, and S. M. Pietralunga. Polarization stabilization in optical communications systems. *Journal of Lightwave Technology*, 24(11):4172–4183, 2006.

[38] M. F. Ramos, N. A. Silva, N. J. Muga, and A. N. Pinto. Reversal operator to compensate polarization random drifts in quantum communications. *Opt. Express*, 28(4):5035–5049, Feb 2020.

[39] M. F. Ramos, N. A. Silva, N. J. Muga, and A. N. Pinto. Full polarization random drift compensation method for quantum communication. *Opt. Express*, 30(5):6907–6920, Feb 2022.

[40] A. Treiber, A. Poppe, M. Hentschel, D. Ferrini, T. Lorünser, E. Querasser, T. Matyus, H. Hübel, and A. Zeilinger. A fully automated entanglement-based quantum cryptography system for telecom fiber networks. *New J. Phys.*, 11(4):045013, apr 2009.

[41] Y.-Y. Ding, W. Chen, H. Chen, C. Wang, Y.-P. li, S. Wang, Z.-Q. Yin, G.-C. Guo, and Z.-F. Han. Polarization-basis tracking scheme for quantum key distribution using revealed sifted key bits. *Opt. Lett.*, 42(6):1023–1026, Mar 2017.

[42] P. M. *et al* . A study of polarization compensation for quantum networks. *EPJ Quantum Technology*, 10(1):1–11, 2023.

[43] Y. Shi, H. S. Poh, A. Ling, and C. Kurtsiefer. Fibre polarisation state compensation in entanglement-based quantum key distribution. *Opt. Express*, 29(23):37075–37080, Nov 2021.

[44] J. Chen, G. Wu, L. Xu, X. Gu, E. Wu, and H. Zeng. Stable quantum key distribution with active polarization control based on time-division multiplexing. *New J. Phys.*, 11(6):065004, 2009.

[45] S. Wengerowsky, S. K. Joshi, F. Steinlechner, J. R. Zichi, S. M. Dobrovolskiy, R. van der Molen, J. W. N. Los, V. Zwiller, M. A. M. Versteegh, A. Mura, D. Calonico, M. Inguscio, H. Hübel, L. Bo, T. Scheidl, A. Zeilinger, A. Xuereb, and R. Ursin. Entanglement distribution over a 96-km-long submarine optical fiber. *Proceedings of the National Academy of Sciences*, 116:6684–6688, 4 2019.

[46] R. Glauber. *The Quantum Theory of Optical Coherence*. John Wiley Sons, Ltd, 2006.

[47] R. Loudon. *The Quantum Theory of Light*. OUP Oxford, 2000.

[48] J. J. Sakurai and J. Napolitano. *Modern quantum mechanics; 2nd ed.* Addison-Wesley, San Francisco, CA, 2011.

[49] R. Horodecki, P. L. Horodecki, M. L. Horodecki, and K. Horodecki. Quantum entanglement, 2009.

[50] W. K. Wootters. Entanglement of formation of an arbitrary state of two qubits. *Phys. Rev. Lett.*, 80:2245–2248, Mar 1998.

[51] J. F. Clauser, M. A. Horne, A. Shimony, and R. A. Holt. Proposed Experiment to Test Local Hidden-Variable Theories. *Phys Rev. Lett.*, 23:880–884, Oct 1969.

[52] R. Horodecki, I. Horodecki, and M. Horodecki. Violating Bell inequality by mixed spin-1/2 states: necessary and sufficient condition. *Physics Letters A*, 200:340–344, 1995.

[53] J. P. Dowling. *Schrödinger's Web: Race to Build the Quantum Internet*. CRC Press, 2021.

[54] S.-H. Wei, B. Jing, X.-Y. Zhang, J.-Y. Liao, C.-Z. Yuan, B.-Y. Fan, C. Lyu, D.-L. Zhou, Y. Wang, G.-W. Deng, H.-Z. Song, D. Oblak, G.-C. Guo, and Q. Zhou. Towards real-world quantum networks: A review. *Laser & Photonics Reviews*, 16(3):2100219, 2022.

[55] P. P. Rohde. *The Quantum Internet: The Second Quantum Revolution*. Cambridge University Press, 2021.

[56] J. C. Bienfang, A. J. Gross, A. Mink, B. J. Hershman, A. Nakassis, X. Tang, R. Lu, D. H. Su, C. W. Clark, C. J. Williams, E. W. Hagley, and J. Wen. Quantum key distribution with 1.25 Gbps clock synchronization. *Opt. Express*, 12(9):2011–2016, May 2004.

[57] L. Calderaro, A. Stanco, C. Agnesi, M. Avesani, D. Dequal, P. Villoresi, and G. Vallone. Fast and simple qubit-based synchronization for quantum key distribution. *Phys. Rev. Appl.*, 13:054041, May 2020.

[58] M. Alshowkan, B. P. Williams, P. G. Evans, N. S. Rao, E. M. Simmerman, H.-H. Lu, N. B. Lingaraju, A. M. Weiner, C. E. Marvinney, Y.-Y. Pai, B. J. Lawrie, N. A. Peters, and J. M. Lukens. Reconfigurable quantum local area network over deployed fiber. *PRX Quantum*, 2:040304, Oct 2021.

[59] I. A. Burenkov, A. Semionov, Hala, T. Gerrits, A. Rahmouni, D. Anand, Y.-S. Li-Baboud, O. Slattery, A. Battou, and S. V. Polyakov. Synchronization and coexistence in quantum networks. *Opt. Express*, 31(7):11431–11446, Mar 2023.

[60] D. Poderini, E. Polino, G. Rodari, A. Suprano, R. Chaves, and F. Sciarrino. Ab initio experimental violation of Bell inequalities. *Phys. Rev. Res.*, 4:013159, Feb 2022.

[61] M. A. Nielsen and I. L. Chuang. *Quantum Computation and Quantum Information: 10th Anniversary Edition*. Cambridge University Press, 2012.

[62] S. M. Barnett. *Quantum Information*. Oxford University Press, 2009.

[63] C. Bennett and G. Brassard. Quantum cryptography: Public key distribution and coin tossing. *Proceeds of the IEEE International Conference on Computers, Systems, and Signals*, 1984.

[64] C. H. Bennett, G. Brassard, and N. D. Mermin. Quantum cryptography without Bell's theorem. *Phys. Rev. Lett.*, 68:557–559, Feb 1992.

[65] A. Ekert. Quantum cryptography based on Bell's theorem. *Phys Rev. Lett.*, 67:661–663, Aug 1991.

[66] N. Gisin, G. Ribordy, W. Tittel, and H. Zbinden. Quantum cryptography. *Rev. Mod. Phys.*, 74:145–195, Mar 2002.

[67] W. Woottres and W. Zurek. A single quantum cannot be cloned. *Nature*, 299:802–803, 1982.

[68] General Photonics Corporation Ltd., Frequently Asked Questions for PolaRITE II/III Polarization Controllers.

[69] M. Jofre, G. Anzolin, F. Steinlechner, N. Oliverio, J. P. Torres, V. Pruneri, and M. W. Mitchell. Fast beam steering with full polarization control using a galvanometric optical scanner and polarization controller. *Opt. Express*, 20(11):12247–12260, May 2012.

[70] S. Harris, M. Oshman, and R. Byer. Observation of tunable optical parametric fluorescence. *Phys. Rev. Lett.*, 18(18):732, 1967.

[71] R. Ghosh and L. Mandel. Observation of nonclassical effects in the interference of two photons. *Phys. Rev. Lett.*, 59:1903–1905, Oct 1987.

[72] P. G. Kwiat, K. Mattle, H. Weinfurter, A. Zeilinger, A. V. Sergienko, and Y. Shih. New high-intensity source of polarization-entangled photon pairs. *Phys. Rev. Lett.*, 75:4337–4341, Dec 1995.

[73] P. G. Kwiat, E. Waks, A. G. White, I. Appelbaum, and P. H. Eberhard. Ultrabright source of polarization-entangled photons. *Phys. Rev. A*, 60:R773–R776, Aug 1999.

[74] A. G. White, D. F. V. James, P. H. Eberhard, and P. G. Kwiat. Nonmaximally entangled states: Production, characterization, and utilization. *Phys. Rev. Lett.*, 83:3103–3107, Oct 1999.

[75] M. Fiorentino, S. M. Spillane, R. G. Beausoleil, T. D. Roberts, P. Battle, and M. W. Munro. Spontaneous parametric down-conversion in periodically poled KTP waveguides and bulk crystals. *Opt. Express*, 15(12):7479–7488, Jun 2007.

[76] C. Couteau. Spontaneous parametric down-conversion. *Contemp. Phys.*, 59(3):291–304, 2018.

[77] S. Lerch, B. Bessire, C. Bernhard, T. Feurer, and A. Stefanov. Tuning curve of type-0 spontaneous parametric down-conversion. *J. Opt. Soc. Am. B*, 30(4):953–958, Apr 2013.

[78] R. W. Boyd. *Nonlinear Optics, Third Edition*. Academic Press, Inc., USA, 3rd edition, 2008.

[79] C. E. Kuklewicz, M. Fiorentino, G. Messin, F. N. C. Wong, and J. H. Shapiro. High-flux source of polarization-entangled photons from a periodically poled $KTiOPO_4$ parametric down-converter. *Phys. Rev. A*, 69:013807, Jan 2004.

[80] F. Kaiser, A. Issautier, L. A. Ngah, O. Alibart, A. Martin, and S. Tanzilli. A versatile source of polarization entangled photons for quantum network applications. *Laser Phys. Lett.*, 10(4):045202, feb 2013.

[81] M. C. Tichy. Interference of identical particles from entanglement to boson-sampling. *J. Phys. B: Atom. Mol. Opt. Phys.*, 47(10):103001, may 2014.

[82] S. Bose and D. Home. Generic entanglement generation, quantum statistics, and complementarity. *Phys. Rev. Lett.*, 88:050401, Jan 2002.

[83] R. A. Brewster, G. Baumgartner, and Y. K. Chembo. Quantum analysis of polarization entanglement degradation induced by multiple-photon-pair generation. *Phys. Rev. A*, 104:022411, Aug 2021.

[84] T. Kim, M. Fiorentino, and F. N. C. Wong. Phase-stable source of polarization-entangled photons using a polarization sagnac interferometer. *Phys. Rev. A*, 73:012316, Jan 2006.

[85] C. Liang, K. F. Lee, M. Medic, P. Kumar, R. H. Hadfield, and S. W. Nam. Characterization of fiber-generated entangled photon pairs with superconducting single-photon detectors. *Opt. Express*, 15(3):1322–1327, Feb 2007.

[86] O. Kuzucu and F. N. C. Wong. Pulsed sagnac source of narrow-band polarization-entangled photons. *Phys. Rev. A*, 77:032314, Mar 2008.

[87] P. J. Thomas, C. J. Chunnilall, D. J. M. Stothard, D. A. Walsh, and M. H. Dunn. Production of degenerate polarization entangled photon pairs in the telecom-band from a

pump enhanced parametric downconversion process. *Opt. Express*, 18(25):26600–26612, Dec 2010.

[88] W. P. Grice and I. A. Walmsley. Spectral information and distinguishability in type-ii down-conversion with a broadband pump. *Phys. Rev. A*, 56:1627–1634, Aug 1997.

[89] J. B. Altepeter, E. R. Jeffrey, and P. G. Kwiat. Photonic state tomography. *Adv. At. Mol. Opt. Phys.*, 52:105–159, 2005.

[90] P. Kwiat and *et al* . Quantum-Tomography. `https://github.com/KwiatLab/Quantum-Tomography/`, 2023.

[91] Y. Namihira and H. Wakabayashi. Real-time measurements of polarization fluctuations in an optical fiber submarine cable in a deep-sea trial using electrooptic $LiNbO_3$ device. *Journal of Lightwave Technology*, 7(8):1201–1206, 1989.

[92] H. Shimizu, S. Yamazaki, T. Ono, and K. Emura. Highly practical fiber squeezer polarization controller. *J. Lightwave Technol.*, 9(10):1217–1224, 1991.

[93] F. Heismann. Analysis of a Reset-Free Polarization Controller for Fast Automatic Polarization Stabilization in Fiber-optic Transmission Systems. *Journal of Lightwave Technology*, 12(4):690–699, 1994.

[94] C. L. Cortes, P. Lefebvre, N. Lauk, M. J. Davis, N. Sinclair, S. K. Gray, and D. Oblak. Sample-efficient adaptive calibration of quantum networks using Bayesian optimization. *Phys. Rev. App.*, 17(3):034067, 2022.

[95] R. A. Brewster, J. Goldhar, M. Morris, G. Baumgartner, and Y. K. Chembo. Estimation of the chsh parameter using hom interference. *IEEE Transactions on Quantum Engineering*, 3:1–10, 2022.

[96] M. Takeoka, R.-B. Jin, and M. Sasaki. Full analysis of multi-photon pair effects in spontaneous parametric down conversion based photonic quantum information processing. *New J. Phys.*, 17(4):043030, apr 2015.

[97] J. P. Gordon and H. Kogelnik. PMD fundamentals: Polarization mode dispersion in optical fibers. *Proc. Natl. Acad. Sci. U.S.A.*, 97(9):4541–4550, 2000.

[98] J. A. Nelder and R. Mead. A Simplex Method for Function Minimization. *The Computer Journal*, 7(4):308–313, 01 1965.

[99] P. Virtanen and *et al* . SciPy 1.0: fundamental algorithms for scientific computing in Python. *Nature Methods*, 17(3):261–272, 2020.

[100] F. Grünenfelder, A. Boaron, D. Rusca, A. Martin, and H. Zbinden. Simple and high-speed polarization-based QKD. *App. Phys. Lett.*, 112(5):051108, 01 2018.

[101] O. Gühne and G. Tóth. Entanglement detection. *Phys. Rep.*, 474(1):1–75, 2009.

[102] M. Barbieri, F. De Martini, G. Di Nepi, P. Mataloni, G. M. D'Ariano, and C. Macchiavello. Detection of Entanglement with Polarized Photons: Experimental Realization of an Entanglement Witness. *Phys. Rev. Lett.*, 91:227901, Nov 2003.

[103] G. Chen, W.-H. Zhang, P. Yin, C.-F. Li, and G.-C. Guo. Device-independent characterization of entanglement based on Bell nonlocality. *Fundamental Research*, 1(1):27–42, 2021.

[104] W. J. Munro, K. Nemoto, and A. G. White. The Bell inequality: A measure of entanglementa? *J. Mod. Optics*, 48(7):1239–1246, 2001.

[105] L.-K. Yang, G. Chen, W.-H. Zhang, X.-X. Peng, S. Yu, X.-J. Ye, C.-F. Li, and G.-C. Guo.

Self-guided method to search maximal Bell violations for unknown quantum states. *Phys. Rev. A*, 96:052310, Nov 2017.

[106] J. Cortés, J. Barra, L. Pereira, and A. Delgado. Detecting entanglement of unknown states by violating the Clauser–Horne–Shimony–Holt inequality. *Quantum Information Processing*, 22, 05 2023.

[107] Y. Ma and M. H. Yung. Transforming Bell's inequalities into state classifiers with machine learning. *npj Quantum Inf.*, 4, 12 2018.

[108] D. L. Deng. Machine Learning Detection of Bell Nonlocality in Quantum Many-Body Systems. *Phys Rev. Lett.*, 120, 6 2018.

[109] A. Canabarro, S. Brito, and R. Chaves. Machine Learning Nonlocal Correlations. *Phys Rev. Lett.*, 122:200401, May 2019.

[110] K. Bharti, T. Haug, V. Vedral, and L. Kwek. How to Teach AI to Play Bell Non-Local Games: Reinforcement Learning. arXiv:1912.10783, 2019.

[111] K. Bharti, T. Haug, V. Vedral, and L. Kwek. Machine Learning meets Quantum Foundations: A Brief Survey. *AVS Quantum Sci.*, 2(3):034101, 2020.

[112] R. Garnett. *Bayesian Optimization*. Cambridge University Press, 2023.

[113] R. A. Brewster, G. Baumgartner, and Y. K. Chembo. General characterization of qubit-preserving impairments on two-qubit bell nonlocality. *Phys. Rev. A*, 107:022225, Feb 2023.

[114] F. Zheng, R. Xu, G. Zhu, B. Jin, L. Kang, W. Xu, J. Chen, and P. Wu. Design of a polarization-insensitive superconducting nanowire single photon detector with high detection efficiency. *Sci. Rep.*, 6(1):22710, 2016.

[115] X. C. *et al* . Fractal superconducting nanowire single-photon detectors with reduced polarization sensitivity. *Opt. Lett.*, 43(20):5017–5020, 2018.

[116] S. N. Dorenbos, E. M. Reiger, N. Akopian, U. Perinetti, V. Zwiller, T. Zijlstra, and T. M. Klapwijk. Superconducting single photon detectors with minimized polarization dependence. *App. Phys. Lett.*, 93(16):161102, 2008.

[117] V. B. Verma, F. Marsili, S. Harrington, A. E. Lita, R. P. Mirin, and S. W. Nam. A three-dimensional, polarization-insensitive superconducting nanowire avalanche photodetector. *App. Phys. Lett.*, 101(25):251114, 2012.

[118] C. K. Hong and L. Mandel. Theory of parametric frequency down conversion of light. *Phys. Rev. A*, 31:2409–2418, Apr 1985.

[119] M. L. Stein. *Interpolation of spatial data: some theory for kriging*. Springer Science & Business Media, 2012.

[120] F. Nogueira. Bayesian Optimization: Open source constrained global optimization tool for Python. `https://github.com/fmfn/BayesianOptimization/`, 2014.

[121] P. Shadbolt, T. Vértesi, Y. Liang, C. Branciard, N. Brunner, and J. L. O'Brien. Guaranteed violation of a Bell inequality without aligned reference frames or calibrated devices. *Sci. Rep.*, 2(1):1–7, 2012.

[122] M. C. Tran, B. Dakić, W. Laskowski, and T. Paterek. Correlations between outcomes of random measurements. *Phys. Rev. A*, 94:042302, Oct 2016.

[123] G. B. Arfken, H. J. Weber, and F. E. Harris. *Mathematical methods for physicists: a comprehensive guide*. Academic press, 2012.

[124] K. Okamoto. Fundamentals of Optical Waveguides (Second Edition). pages 1–158. Academic Press, Burlington, second edition edition, 2006.

[125] D. Gloge. Weakly Guiding Fibers. *Appl. Opt.*, 10(10):2252–2258, Oct 1971.

[126] K. Kato and E. Takaoka. Sellmeier and thermo-optic dispersion formulas for KTP. *Appl. Opt.*, 41(24):5040–5044, Aug 2002.